Università degli Studi di Torino
Dipartimento di Fisica
Corso di Laurea Magistrale in Fisica

Tesi di Laurea Magistrale

Signal Formation in Innovative Silicon Detectors

Candidato:
Francesca Cenna

Relatore:
Prof. Ada Solano

Corelatore:
Dott. Nicolò Cartiglia

Anno Accademico 2012-2013

Abstract

Silicon-based tracking sensors have excellent position resolution, however, presently, the time determination is usually quite poor (∼ns): this fact is imposing severe restrictions on many applications and it has driven several R&D groups to design a new type of silicon sensor, able to measure with high precision the space (∼10 µm) and time (∼10 ps) coordinates of a particle. These new devices are called Ultra-Fast Silicon Detectors (UFSD) and make use of a reduced thickness to decrease collection time, and a low charge multiplication to enlarge the signal amplitude. This latter property is obtained by changing the current design of pixelated silicon detectors introducing an innovative doping profile that allows charge multiplication.
Chapter 1 presents the effects of radiation interaction with matter and the properties of silicon.
Chapter 2 is about silicon detectors: it describes the mechanism at the base of signal formation, as well as the principles of noise and signal shaping. An overview of the most common sensor geometries is also given.
Chapter 3 introduces two innovative architectures for silicon detectors: "3D" and Ultra-Fast. In particular, the mechanism of charge multiplication in silicon and its relation to the electric field are inspected.
Chapter 4 provides a description of the electronic circuits used for time measurements and an estimate of the time resolution with a leading edge discrimination technique. In particular, some aspects of timing with Ultra-Fast detectors are predicted, as well as their effects on time resolution.
Chapter 5 describes the program *Weightfield 2.0*: it allows to simulate a silicon sensor with internal gain and to investigate the effects of charge multiplication in the presence of a non-uniform charge deposition inside the sensor.
Chapter 6, finally compares the output of a *Weightfield 2.0* simulation with the results of laser tests on one of the first Ultra-Fast diodes produced by CNM in Barcelona.

Sommario

I rivelatori al silicio hanno un'eccellente risoluzione spaziale, mentre, attualmente, la risoluzione temporale è invece piuttosto scarsa (dell'ordine dei nanosecondi). Questo fatto limita molte delle loro applicazioni e ha spinto molti gruppi a sviluppare un nuovo tipo di rivelatore al silicio che sia in grado di misurare con elevata precisione sia lo spazio che il tempo. La risoluzione spaziale che si prevede di raggiungere è dell'ordine dei 10 µm, mentre quella temporale è all'incirca 10 ps. Tali dispositivi sono chiamati Ultra-Fast Silicon Detectors (UFSD) e sono caratterizzati da uno spessore ridotto in modo da ridurre il tempo di raccolta della carica, e da una moderata moltiplicazione di carica interna denominata "guadagno", la quale permette di aumentare l'ampiezza del segnale.
Il capitolo 1 presenta gli effetti dell'interazione della radiazione con la materia e le proprietà del silicio.
Il capitolo 2 tratta dei rivelatori al silicio: vengono descritti il meccanismi alla base della formazione del segnale, del noise e dello shaping. Inoltre, vengono trattate le principali geometrie in uso per i rivelatori di particelle.
Il capitolo 3 introduce due tipi di rivelatori al silicio innovativi: "3D"e Ultra-Fast. In particolare, viene prestata attenzione al meccanismo di moltiplicazione della carica nel silicio e alla sua dipendenza dal campo elettrico.
Il capitolo 4 fornisce una descrizione dei circuiti elettronici che vengono tipicamente utilizzati per le misure di timing, nonché alcune previsioni riguardanti la risoluzione temporale, nel caso di utilizzo di rivelatori Ultra-Fast.
Il capitolo 5 descrive il programma *Weightifield 2.0*, che permette di simulare un sensore al silicio con guadagno interno e di studiare la moltiplicazione della carica in presenza di una deposizione di carica non uniforme all'interno del sensore.
Il capitolo 6, infine, confronta il risultato delle simulazioni di *Weightifield 2.0* con i test effettuati col laser su uno dei primi diodi Ultra-Fast, prodotto dalla CNM di Barcellona.

Contents

1 Semiconductors **9**
1.1 Particle interaction with matter 9
1.1.1 Energy loss for charged particles 9
1.1.2 Interaction of photons with matter 12
1.2 Conduction in solids 14
1.2.1 Silicon properties 16
1.2.2 Doping silicon 17
1.2.3 Drift 18
1.2.4 Diffusion 20
1.2.5 pn diode 21

2 Silicon Detectors **27**
2.1 Signal formation in silicon sensors 28
2.1.1 Induced current and Shockley-Ramo theorem 28
2.1.2 Charge carriers motion 31
2.1.3 Radiation damage 32
2.2 Front-end electronics 37
2.2.1 Charge sensitive amplifier 38
2.2.2 Noise 39
2.2.3 Shaping 40
2.3 Silicon sensor production 43
2.3.1 Monocrystalline growing 43
2.3.2 From wafer to sensor 44
2.4 Geometries for silicon detectors 45
2.4.1 Pad 46
2.4.2 Microstrip 46
2.4.3 Pixel detectors 47
2.4.4 APD 49

3 Innovative silicon detectors **53**
3.1 3D pixel detectors 53
3.1.1 3D layouts 53
3.1.2 Pixel configurations 55
3.1.3 Active and slim edges 56
3.2 Ultra Fast detectors 57
3.2.1 Operating principle 58
3.2.2 Impact ionization model 59
3.2.3 Sensor thickness 62

3.2.4 Electric field 62
3.2.5 Applications of Ultra-Fast detectors 64

4 Time Measurements 67
4.1 Timing circuits 67
4.2 Time resolution 69
4.2.1 Time walk 70
4.2.2 Jitter 72
4.2.3 Noise estimate 73
4.2.4 Timing with UFSD 73

5 UFSD Simulator 77
5.1 The Weightfield 2.0 program 77
5.1.1 Potentials calculation 77
5.1.2 Field calculation 79
5.1.3 Current calculation 80
5.1.4 Gain implementation 83
5.1.5 Graphical interface 85

6 Measurements and Results 99
6.1 Laser test 99
6.2 The LGAD under test 100
6.3 Laboratory measurements 106
6.3.1 Laboratory setup 106
6.3.2 Laser measurements and simulation 107

Chapter 1

Semiconductors

This chapter describes the properties of semiconductors and how radiation interacts with matter, explaining the operating principle of semiconductor detectors.

1.1 Particle interaction with matter

When a charged particle or an energetic photon interacts with an atom or a molecule in a material, *ionization* can take place: the atom or molecule can lose electrons, gaining in this way positive charge.
Radiation can ionize a material directly or indirectly. Direct ionizing radiation is typical of charged particles, while neutral particles like neutrons and photons produce secondary particles which can excite the material or cause secondary ionization.
While crossing a material, particles lose their energy. This energy loss can occur gradually (as for charged particles) or in a single collision (photons and neutrons). Another effect, the so called *multiple Coulomb scattering* from nuclei causes a series of small-angle trajectory deflections.

1.1.1 Energy loss for charged particles

As mentioned above, a charged particle passing through matter undergoes soft electromagnetic processes with the electrons of the medium. Different types of collision can lead to *atomic excitation*, displacing an electron to a higher atomic bound state, or *ionization*, creating an electron-ion pair if the transfered energy is higher than the ionization potential of the atom. The average energy for the creation of an electron-ion pair is some tens of eV in gases ($\sim$41 eV for helium, 26 eV for argon and 22 eV for xenon) while it is just a few eV in semiconductors (Si, Ge).
When a very high amount of energy is occasionally transfered in a ionization process, δ rays are produced: they are electrons kicked out from atoms with enough energy to create their own ionization trail.
Ionization represents the predominant way for charged particles to lose energy in matter. Detectors are mainly based on this effect.

Energy loss for heavy charged particles

Except for light particles as electrons and positrons, the mean rate of ionization energy loss for charged particles, also known as stopping power, is given with good approximation by the Bethe-Bloch formula [1]:

$$\langle\frac{dE}{dx}\rangle = 2\pi N_A {r_e}^2 m_e c^2 \frac{Z}{A}\frac{z^2}{\beta^2}\left[\ln\left(\frac{2m_e\gamma^2 v^2 W}{I^2}\right) - 2\beta^2 - \delta - 2\frac{C}{Z}\right] \tag{1.1}$$

where E is the kinetic energy of the incident particle of charge z, moving with velocity β and Lorentz factor γ. $I \approx 10Z^{0.9}$ eV is the mean excitation energy of the material, characterized by density ρ and by atomic and mass number Z and A, respectively. W is the largest kinetic energy that could be transferred to a free electron in a single collision. δ and C are correction factors accounting for the polarization of the medium. $N_A = 6.022\cdot 10^{23}$ mol^{-1} is Avogadro's number, r_e and m_e are classical electron radius and mass.

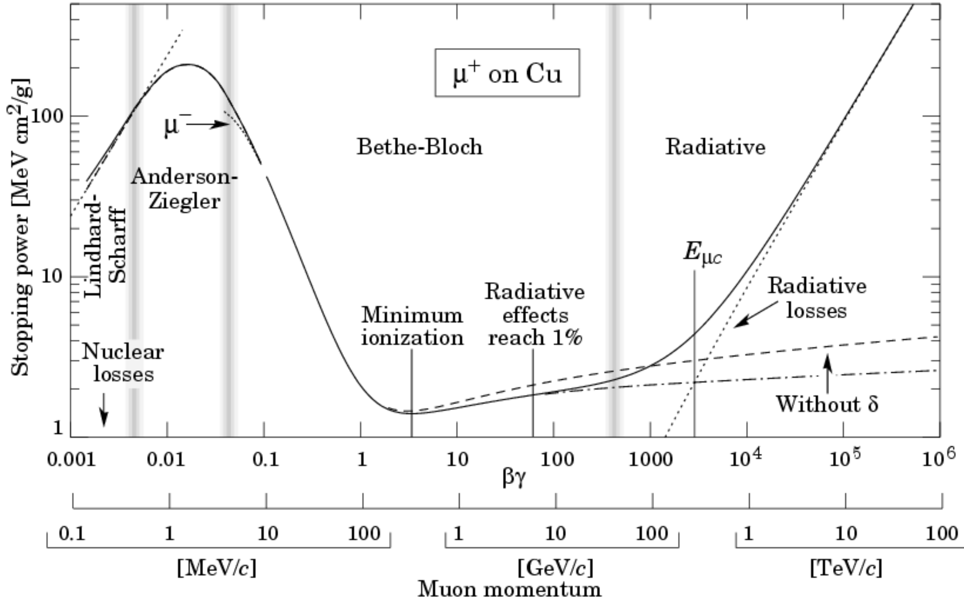

Figure 1.1: Energy loss for μ$^+$ on Cu as a function of $\beta\gamma = p/mc$.

According to the Bethe-Bloch formula, the ionization loss is proportional to the electron density in the medium $\frac{\rho Z N_A}{A}$ and to the square of the projectile charge, and it strongly depends on the projectile velocity. At low momenta the energy loss rate decreases proportionally to $1/\beta^2$.
All tracking detectors make use of the charges produced by the ionization of a charged particle crossing a medium, whether it can be a gas or a semiconductor. In Fig. 1.1 [2] it is shown the energy loss for a positive muon on copper.

Fig. 1.2 shows that in different materials the energy loss in MeV$\cdot$cm^2/g for heavy

charged particles has almost the same dependence on particle momentum. At $1 \div 2$ MeV $\cdot$ cm^2/g the energy loss reaches its minimum in all materials. A particle with energy at the minimum of this formula is called *minimum ionizing particle* (MIP): most relativistic particles have mean energy loss rates close to the minimum. In silicon, minimum ionization occurs at $\beta\gamma = 3$, corresponding to a value of $\langle dE/dx \rangle_{min} \sim 1.66$ MeV$\cdot$cm^2/g. For detectors of moderate thickness,

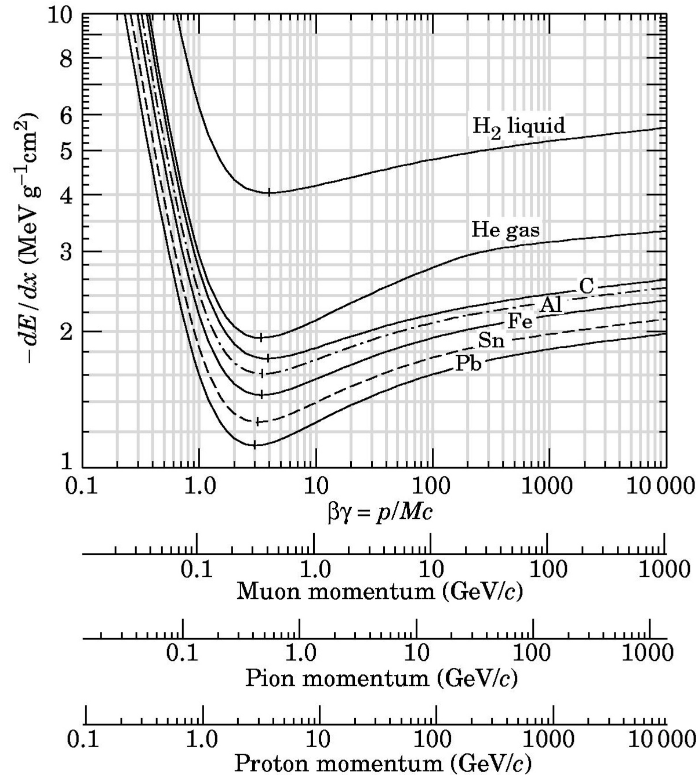

Figure 1.2: Bethe-Bloch formula for different materials.

the the energy loss probability distribution for the energy lost by a particle in a single hit is described by the Landau curve, whose tail at high energies is due to the so called *delta rays*, which are very energetic but rare events. As the detector thickness increases, the Landau curve gains a more Gaussian shape, since the material thickness allows many hits with atomic electrons [4].
For very thin absorbers the "standard" Landau distribution fails to describe properly the energy loss: the most probable value decreases as the thickness decreases, while the distribution width spreads. The variation with detector thickness of the Landau distribution is shown in Fig. 1.3[2]

Energy loss for electrons

Light charged particles behave in a different way with respect to heavy ones. When decelerating, charged particles lose kinetic energy which is converted into

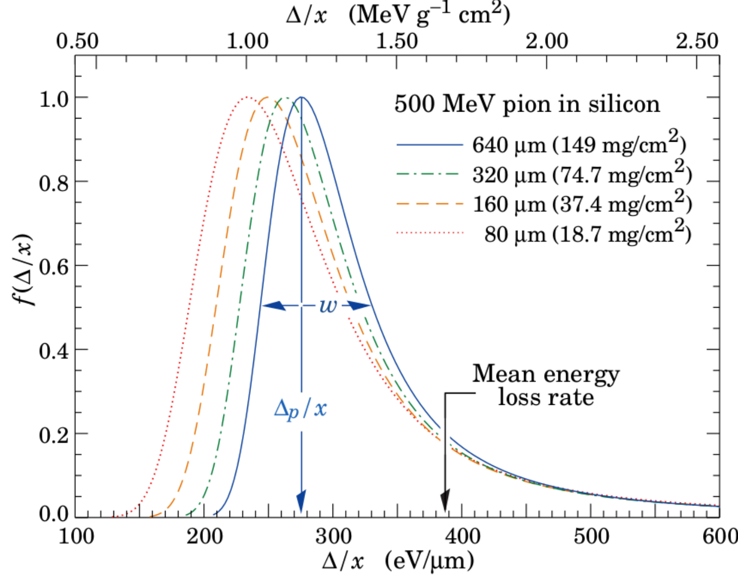

Figure 1.3: Straggling functions in silicon for 500 MeV pions, normalized to unity at the most probable value Δ_p/x, for different sensor thicknesses: as the thickness decreases, the most probable value lowers and the width w broadens.

photons: this electromagnetic radiation is called *Bremsstrahlung*. Its contribution is not relevant for heavy charged particles, but for electrons, due to their low mass, it becomes important and has to be accounted for when evaluating the total energy loss:

$$\langle\frac{dE}{dx}\rangle = \left(\frac{dE}{dx}\right)_{Brems} + \left(\frac{dE}{dx}\right)_{Ion}, \tag{1.2}$$

where the contribution of Bremsstrahlung can be written as:

$$-\frac{1}{\rho}\left(\frac{dE}{dx}\right)_{Brems} = \frac{E}{X_0},$$

with X_0 the radiation length, namely the distance needed to reduce the electron energy by a factor e:

$$\frac{1}{X_0} = \frac{4Z(Z+1)N_A}{137A} r_e^2 \ln\left(\frac{183}{Z^{\frac{1}{3}}}\right). \tag{1.3}$$

1.1.2 Interaction of photons with matter

Photons interact with matter in three main ways, depending on their energy: *photoelectric effect*, *Compton scattering* and *pair production*.
The absorption of a beam of incident photons with same direction and energy

can be modeled by the exponential law:

$$N(x) = N_0 e^{-\mu_L x}, \tag{1.4}$$

where N_0 is the initial number of photons, $N(x)$ is the number of photons not yet absorbed at a given distance x and μ_L is the linear absorption coefficient:

$$\mu_L = \frac{\sigma N_A \rho}{A} \equiv \frac{1}{\lambda},$$

with σ the total cross section, ρ the density of the material and λ the mean free path, namely the average distance covered by a photon before being absorbed. The total cross section σ can be defined as the sum of the cross sections of the three main concurrent effects:

$$\sigma_{TOT} = \sigma_{Photo} + \sigma_{Compton} + \sigma_{Pair}.$$

Photoelectric effect

An incident photon is absorbed and all its energy is transferred to an electron from the inner shells of the atom. This electron is then ejected from that atom with a kinetic energy

$$E = h\nu - I,$$

where I, the *ionization potential*, denotes the energy required to remove a bound electron from that atom, namely the binding energy for the K- and L-shell electrons.
The electron can then cause secondary ionization in the medium, loosing energy in the material. It is important to note that the photon “disappears” in this process.
The ionization potential $I = (13.6eV)Z^2/n^2$, where n is the principal quantum number, depends on the square of the nuclear charge Z of the atom (and so on the dimension of the atom). The cross section for this effect is also strongly dependent on Z:

$$\sigma_{Photo} \propto Z^n,$$

where n assumes values between 4 and 5, depending on the photon energy.
The photoelectric effect is dominant at low photon energies (in silicon below 100 keV); for this reason high-Z materials are preferred for X-ray detection.

Compton effect

The incident photon transfers only part of its energy $h\nu$ to an electron in the outer shells of the atom. The remaining energy is taken away by a new photon of lower energy $h\nu'$.
This new photon is scattered, because it takes off in a new direction, forming an angle θ with the direction of the incident photon according to the equation:

$$h\nu' = h\nu \left[1 + \frac{h\nu}{m_e c^2}(1 - cos\theta)\right]^{-1}. \tag{1.5}$$

The scattering angle θ can take any value between 0 and 180°, proportionally to the amount of energy transferred to the electron. The maximum energy transfer occurs at $\theta = 180°$, when the photon is scattered backwards and the electron travels in the direction of the incident photon. The electron ejected from the atom can then produce ionizations.

Pair production

In this process a photon is converted into an electron-positron pair.
To conserve energy, the pair production occurs only at photon energies of at least $2m_ec^2 \sim 1.022$ MeV. The positron will loose energy by interaction with electrons in the absorbing material exactly like an electron. When it has lost all its kinetic energy, since the positron at rest is not a stable particle, it can not exist in the presence of other electrons, and another reaction occurs, where a positron-electron pair annihilates producing two photons with energy of 0.511 MeV each. (The electron involved in this annihilation can be any electron: not necessarily the one created by pair production.)

1.2 Conduction in solids

Electrons of a single isolated atom fill a discrete set of energy levels with quantized energies.
When atoms are bound together forming a solid, the potential energy and the energy levels of each electron change: the strongly bound ones do not undergo substantial variations in energy, the weakly bound ones instead are no longer localized, and their possible energy values fill continuous bands separated by forbidden gaps. The band structure of a given material can exhibit a very large

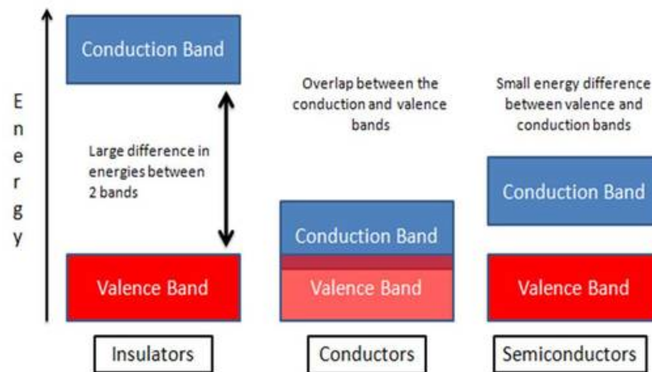

Figure 1.4: Schematic band structure for insulators, conductors and semiconductors.

number of bands. Among them, the *valence band*, defined as the highest energetic level completely filled by electrons at a temperature $T = 0$ K and the *conduction band*, which is the band standing immediately above the valence

band, are focal for the electronic and optical properties of a material.
As shown in Fig. 1.4, materials can be distinguished from the value of the distance between the conduction and the valence band, called *band gap*: insulators have a wide band gap of about 10 eV, while in conductors the conduction and the valence bands overlap. Semiconductors have intermediate features and a band gap of about 1 eV.
Insulators have the valence band completely filled, while the conduction band is empty: electrons need a large amount of energy to reach the conduction band from the valence band, much more than the energy gained from thermal agitation. Since electric conduction occurs in the conduction band only, in insulators there will be no current flow.
Semiconductors, whose band gap is much smaller, at higher temperatures can exhibit a current flow because some electrons become more energetic and jump to the conduction band, leaving holes behind them in the valence band. Since the number of occupied states in the conduction band and that of the unoccupied states in the valence band is small, the conductivity is low and only a small current can flow.
Semiconductor materials are for example silicon, germanium and carbon (diamond). They all have a face-centered cubic crystal structure: germanium is typically used in nuclear physics, has a small band gap of 0.66 eV and needs to operate at low temperatures; diamond has a larger band gap ($\sim$5.5 eV at 300 K [5]), good radiation hardness but provides a small signal and is too expensive to be used extensively. Silicon is then the best choice for reasons which are explained in the following.

1.2.1 Silicon properties

Silicon is a semiconductor, namely a solid which can be considered as an insulator at low temperatures and a conductor at higher temperatures. Its conductivity assumes values of about 10^3 Ω·m and it is intermediate between that of insulators and that of conductors.
Silicon has four valence electrons and forms covalent bonds with other atoms.
A silicon crystal is different from an insulator: only at a temperature of 0 K there are no free electrons, where at any temperature above zero the number of free electrons increases and then there is a finite probability that an electron in the lattice will be knocked loosing from its position and leaving behind an electron deficiency called a “hole”.
The energy distribution of these conduction electrons is called *Fermi-Dirac distribution* (Fig. 1.5 [3]) and is given by

$$f(E,T) = \frac{1}{1+e^{\frac{E-E_F}{kT}}}, \tag{1.6}$$

where E is the electron energy, E_F the *Fermi energy*, namely the energy of the electron in the highest occupied state at 0 K, T is the temperature of the system and k the Boltzmann constant. If an external voltage is applied, both the electron and the hole can contribute to a small current flow.
The conductivity of a semiconductor can be modeled in terms of the band theory of solids. Since for $T > 0$ K electrons can reach the conduction band and

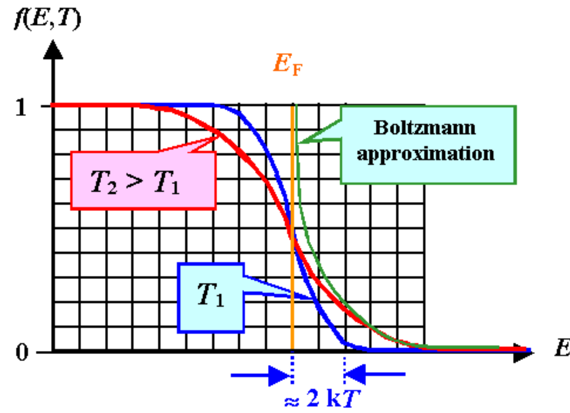

Figure 1.5: Fermi distribution.

contribute to electrical conduction, at room temperature electrons occupy the conduction band and can recombine with holes.
Electrons which have been freed from their lattice positions into the conduction band can move through the material. In addition, other electrons can hop between lattice positions to fill the vacancies left by the freed electrons. This additional mechanism is called *hole conduction* because it is as if the holes are migrating across the material in the direction opposite to the free electron movement.
The current flowing in an intrinsic semiconductor is thus due to electrons and holes. The current flow is influenced by the density of energy states which in turn influences the electron density in the conduction band. This current is highly temperature dependent.
The term "intrinsic" here distinguishes between the properties of pure silicon and the dramatically different properties of doped n-type or p-type semiconductors.
The carrier density for intrinsic silicon is the same for electrons and holes and its dependence on temperature is given by the function:

$$n_i = T^{3/2} \exp\left(-\frac{E_{gap}}{2kT}\right), \tag{1.7}$$

where $n_i = n = p = 1.45 \cdot 10^{10}$ cm^{-3} at $T = 300$ K is the carrier density [7] (n for electrons and p for holes) and E_{gap} is the energy of the forbidden gap separating valence and conduction bands.

1.2.2 Doping silicon

In silicon, the number of electron-hole pairs produced by a MIP in a volume of thickness $d = 300$ µm and a surface $A = 1$ cm^2 can be evaluated by

$$\frac{dE/dx \cdot d}{I_0} \approx 3.2 \cdot 10^4$$

where the mean ionization energy $I_0 = 3.6$ eV and mean energy loss $\langle dE/dx \rangle = 3.87$ MeV/cm.
This number, which represents the signal, should be compared with the number of free carriers thermally produced in the same silicon volume at room temperature ($T = 300$ K), which form the noise

$$n_i dA \approx 4.35 \cdot 10^8.$$

It is remarkable to note that the noise is about four orders of magnitude higher than the signal. Since to detect particles it is necessary to produce a signal higher than the noise, intrinsic silicon cannot be used.
By adding a small percentage of foreign atoms in the crystal lattice of silicon, it is possible to change its electrical properties, producing n-type and p-type semiconductors (Fig. 1.6). The addition of these impurities to the semiconductor lattice is called *doping*. To obtain a n-type material, silicon is doped with *pen-*

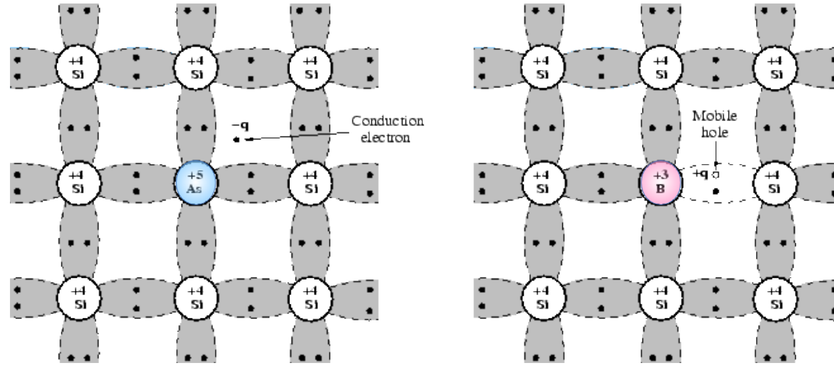

Figure 1.6: Schematic bond representation for n-type silicon doped with arsenic and p-type silicon doped with boron.

tavalent atoms (i.e. donors with one more valence electron) such as antimony, arsenic or phosphorous, which contribute extra electrons. These electrons form energy levels near the conduction band, greatly increasing the conductivity of the intrinsic semiconductor.
A p-type material, instead, is obtained with the addition of *trivalent* impurities (i.e. acceptors with one less valence electron) such as boron, aluminum or gallium, creates holes which form energy levels near the valence band, with an increase of the conductivity.
A doped semiconductor is called "extrinsic". In thermal equilibrium, the concentration of positive and negative charge carriers is constant in time and follows the *mass action law* [7]

$$np = n_i^2, \tag{1.8}$$

which says that the product of the concentration of electrons and holes is equal to the square of the intrinsic carrier density and it is not altered by doping. In n-type silicon electrons are majority and holes minority carriers, while in p-type silicon electrons are minority and holes are majority carriers (Fig. 1.7) [8].
Typical dopant concentrations used in silicon detectors are $\approx 10^{12}$ atoms/cm^3 (higher for CMOS electronics: between 10^{14} atoms/cm^3 and 10^{18} atoms/cm^3).

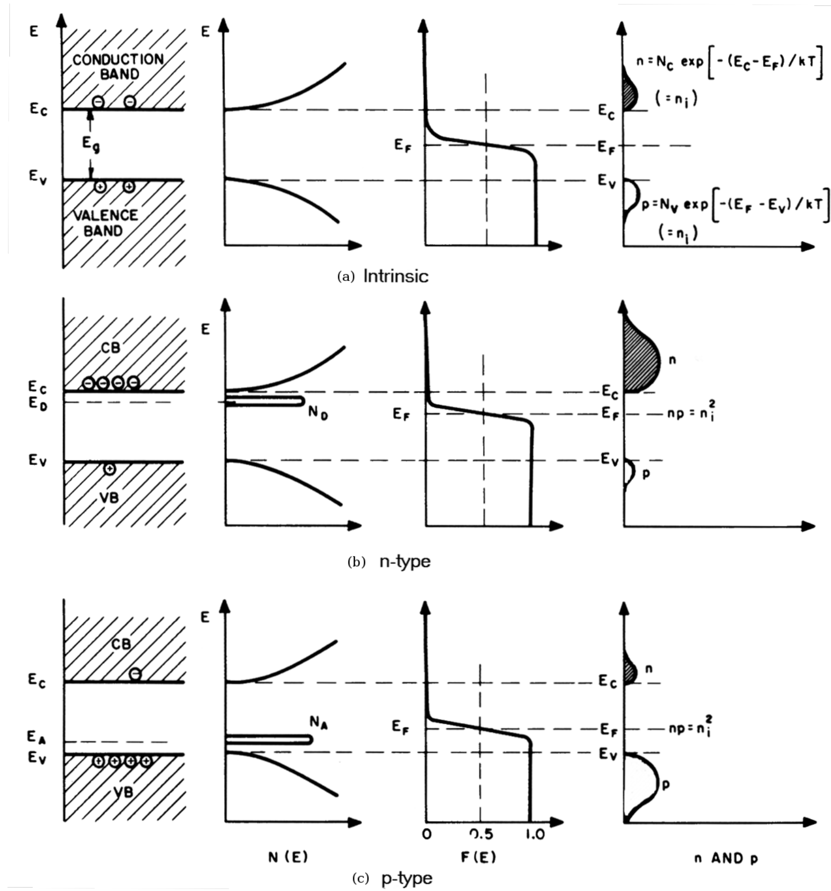

Figure 1.7: Density of states, probability distribution, and carrier concentration in an (a) intrinsic, (b) n-type and (c) p-type semiconductor. In n-type materials there are electron energy levels near the top of the band gap so that they can be easily excited into the conduction band. In p-type materials, extra holes in the band gap allow excitation of valence band electrons, leaving mobile holes in the valence band.

1.2.3 Drift

Charge transportation in semiconductors is mainly due to *drift* and *diffusion* mechanisms.
Drift is achieved by applying an external electric field across the material, so that the charge carriers start to drift with a certain velocity which is proportional to the applied electric field. By introducing electrons and holes *mobilities* as:

$$\mu_n = \frac{e \cdot \tau_n}{m_n} \qquad \mu_p = \frac{e \cdot \tau_p}{m_p}, \tag{1.9}$$

with e the electron charge, $\tau_{n,p}$ the free mean time between successive collisions and $m_{n,p}$ the effective mass, drift velocities are:

$$\overrightarrow{v_e} = -\mu_n \overrightarrow{E} \quad \text{for electrons,} \tag{1.10a}$$

$$\overrightarrow{v_h} = \mu_p \overrightarrow{E} \quad \text{for holes.} \tag{1.10b}$$

Mobility depends on dopant and charge carrier concentrations, temperature and electric field. In silicon, mobilities can be considered constant for electric field values $E < 1$ kV/cm: at 300 K $\mu_n = 1350$ cm^{2}V^{-1}s^{-1} and $\mu_p = 450$ cm^{2}V^{-1}s^{-1}. As the electric field becomes higher, mobility is more and more field-dependent, while the drift velocity tends to become constant, reaching the *saturation value*. Note that holes have a lower mobility value compared to electrons, leading to a drift velocity reduced by about a factor 3, when not in saturation.
The motion of electrons toward the positive terminal and holes to the negative one induces a current, the so called *drift current*, whose total value is

$$J_{TOT} = \mu_n E n q + \mu_p E p q. \tag{1.11}$$

The total induced drift current increases with the increasing of E until it reaches the saturation value. Drift velocity in silicon saturates at about $v_{sat} \sim 10^7$ cm/s for both electrons and holes (Fig. 1.8). To be more precise, holes velocity saturates later and the value is slightly lower ($\sim 9.5 \cdot 10^6$ cm/s).

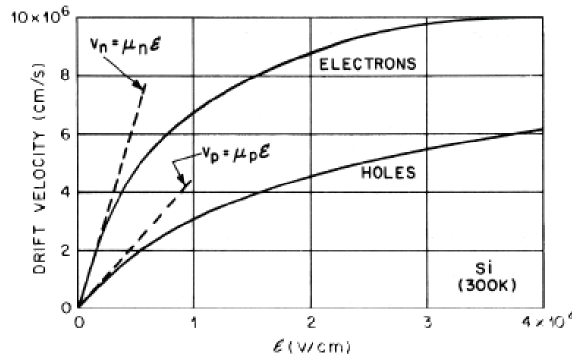

Figure 1.8: Behavior of electrons and holes drift velocity for electric field variations.

1.2.4 Diffusion

Even without an external electric field applied, charge carriers can move inside the semiconductor following a concentration gradient.
Diffusion consists in fact in the motion of charged particles from high to low concentration regions. The resulting diffusion currents are then [9]

$$J_n = qD_n \frac{dn}{dx} \quad \text{for electrons,} \tag{1.12a}$$

$$J_p = -qD_p \frac{dp}{dx} \quad \text{for holes.} \tag{1.12b}$$

where D_n and D_p are the diffusion constants, dn/dx and dp/dx are the concentration gradients for electrons and holes, respectively.
Einstein's relation for diffusion relates diffusion constant and mobility to the absolute temperature value for each type of carriers

$$\frac{D}{\mu} = \frac{kT}{q}. \tag{1.13}$$

Since electrons and holes are free charge carriers, the currents induced by their drift and diffusion motions are affected by an intrinsic noise, whose magnitude is higher than the expected signal for a particle detection. Consequently, intrinsic semiconductors are not effective as particle detectors. For this purpose, they have to be doped and then depleted from free carriers: this can be achieved by a *pn junction*.

1.2.5 pn diode

The simplest sort of semiconductor device is a diode. It consists in a p-type and a n-type silicon sections bonded together (a *pn junction*), with electrodes on each end.
It has three main operating modes: *equilibrium, forward bias* and *reverse bias.*

Equilibrium

When no voltage is applied to the diode, a diffusion motion establishes between the junction: the presence of a region with excess of electrons and lack of holes bonded to a region with excess of holes and lack of electrons causes a gradient of concentration. Hence electrons from the n-type material tend to diffuse into the p region filling the holes of the positive side of the junction and leaving fixed positive ions (donors) behind them. Likewise, holes from the p-type side diffuse toward the n side leaving a region with negative fixed ions (acceptors) in the p side: this creates in proximity of the p-n interface a region without free charge carriers called *depletion zone* or *space charge zone.* Since ions are fixed and do not move, in a depletion zone the semiconductor material is returned to its original insulating state and charge cannot flow.
The depletion zone gives then rise to an electric field which opposes the diffusion process for both electrons and holes (Fig. 1.9). In equilibrium, the potential which establishes in the depletion zone is called *built-in potential*

$$V_{bi} = \frac{k_B T}{q} \ln\left(\frac{N_A N_D}{n_i^2}\right), \tag{1.14}$$

and depends on the dopant concentrations, N_A for acceptors and N_D for donors.
There are two concurrent phenomena: the diffusion process that tends to generate more space charge, and the electric field generated by the space charge that tends to counteract the diffusion.
The built-in potential in silicon V_{bi} takes a value of about 0.7 V.

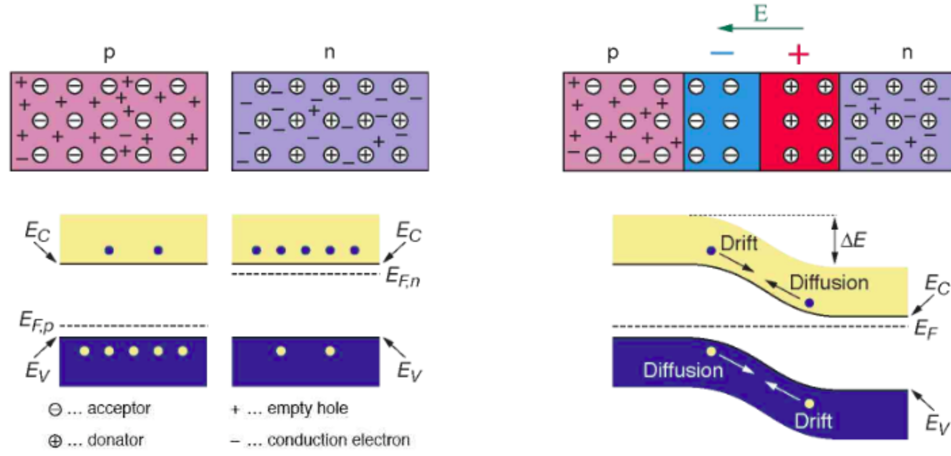

Figure 1.9: pn junction at equilibrium.

Forward bias

To bias a diode, a potential difference has to be applied to the junction.
The first way to bias a pn junction is directly (*forward bias*): the n side is connected to a potential lower than the one at the p side (Fig. 1.10). The n side, with respect to the p side, is then at a negative potential. When forward biased, the positive potential in the p-type region repels the holes and the negative potential in the n-type region repels the electrons: the width of the depletion zone decreases and the built-in potential value lowers. On the contrary, the number of minority carriers increases in both regions, leading to an increase of the diffusion currents.
With increasing forward-bias voltage, the depletion zone eventually becomes thin enough that the built-in potential cannot counteract charge carrier motion across the pn junction, consequently reducing electrical resistance. The electrons which cross the pn junction into the p-type material (or holes which cross into the n-type material) will diffuse in the near-neutral region. Therefore, the amount of minority diffusion in the near-neutral zones determines the amount of current that may flow through the diode.

Reverse bias

Reverse bias is achieved by applying a negative potential to the p-type material and a positive potential to the n-type (Fig. 1.11). This removes holes and electrons from the junction, therefore the width of the depletion zone increases.

By increasing the reverse-bias voltage V_R, the depletion zone W widens further:

$$W = x_n + x_p = \sqrt{\frac{2\epsilon_0\epsilon_{Si}}{e}\left(\frac{1}{N_A} + \frac{1}{N_D}\right)(V_{bi} + V_R)}, \qquad (1.15)$$

where x_n and x_p are respectively the width of the depletion zone in the n and p sides, ϵ_0 is the absolute dielectric constant and ϵ_{Si} is the one relative to silicon.

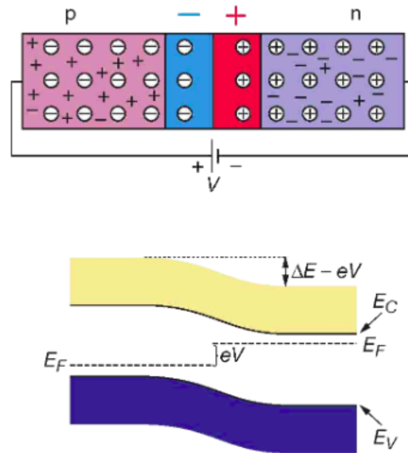

Figure 1.10: pn junction with forward bias.

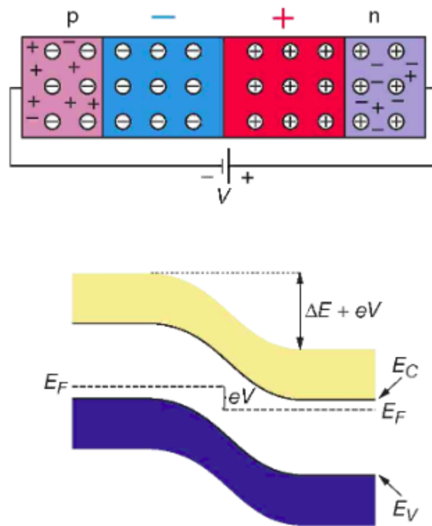

Figure 1.11: pn junction with reverse bias.

Since a silicon sensor is typically formed by a highly doped p^+ implant ($N_A \sim 10^{18}$ cm^{-3}) on a low doped n bulk ($N_D \sim 10^{12}$ cm^{-3}), one finds that the width of the depletion region is deeply shifted to the less doped side (n, in this case), also leading to a negligible built-in voltage value:

$$W \approx x_n \approx \sqrt{\frac{2\epsilon_0 \epsilon_{Si}}{eN_D} V_R}. \tag{1.16}$$

By defining the resistivity as

$$\rho = \frac{1}{eN_D\mu}, \tag{1.17}$$

the width of the depletion zone becomes:

$$W = \sqrt{2\epsilon_0\epsilon_{Si}\rho\mu V_R}, \tag{1.18}$$

where μ is the mobility (for electrons it is $\mu_e = 1350$ cm^2/(Vs), while for holes it is $\mu_h = 450$ cm^2/(Vs).
The whole diode is depleted at a voltage called full depletion voltage V_{FD}

$$V_{FD} = \frac{d^2}{2\epsilon_0\epsilon_{Si}\rho}, \tag{1.19}$$

being d the total thickness of the sensor.
When the electric field intensity increases beyond a critical level, the pn junction depletion zone breaks down and current begins to flow, usually by either the Zener or avalanche breakdown processes. Both of these breakdown processes are non-destructive and are reversible, as long as the amount of current flowing does not reach levels that cause the semiconductor material to overheat causing thermal damage.
The current which flows when a junction is reverse biased is called *leakage current*.
The I(V) characteristic for an ideal silicon pn-diode with a reverse saturation current (leakage current) I_0 is

$$I = I_0\left(e^{\frac{eV}{kT}} - 1\right), \tag{1.20}$$

while the real behavior is displayed in Fig. 1.12.

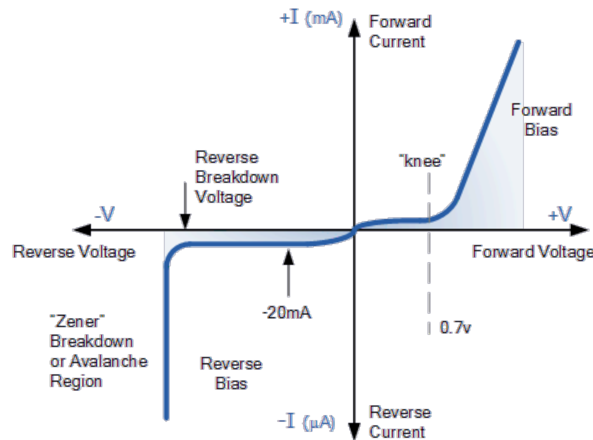

Figure 1.12: I(V) characteristic for a pn silicon junction.

Chapter 2

Silicon Detectors

Silicon is so widely used for electronic devices because it gives a great number of advantages when compared to many other materials.
First of all, its good intrinsic energy resolution: an electron-hole pair is produced every 3.6 eV released by a particle crossing the material. This is of crucial importance since silicon detectors can be considered as solid state ionization chambers: while in the latter ionization takes place into gases, in silicon detectors it takes place into a semiconductor. But considering the ∼30 eV needed to ionize a gas molecule in an ionization chamber, for the same amount of energy silicon yields about 10 times the number of charge carriers.
Other important and useful features are its abundance, its low energy band gap, the possibility to alter the gap properties by adding dopant atoms and the existence of a natural oxide SiO_2.
As introduced in Sec. 1.2.2-3, by the addition of trivalent and pentavalent atoms one gets p-type and n-type silicon, which can be joined together forming a *pn junction*. The junction is characterized by a depletion region W which increases with the applied reverse bias as $W \propto \sqrt{V}$, until it reaches full depletion of

$$V_{FD} = \frac{eNd^2}{2\epsilon_0 \epsilon_{Si}}, \tag{2.1}$$

where N is the concentration of the less doped region. Another important feature for silicon detectors is the reverse bias leakage current or *dark current*: it is dominated by thermally generated e-h pairs, which cannot recombine in the presence of the electric field and then drift separately to the respective electrodes. It converts into power consumption, noise, global warm-up and additional thermal diffusion and it has to be minimized for a proper use of the detector. Leakage current depends on the quality of the material and on the fabrication technique.
The depletion region can be viewed as a parallel plate capacitor with silicon dielectric, whose capacitance decreases with the square of the bias voltage until full depletion is reached, and then it is constant:

$$C(V) = \begin{cases} \sqrt{\frac{q\epsilon_{Si}N}{V_{bias}}} & , V_{bias} \leq V_{FD} \\ \\ \frac{\epsilon_{Si}}{W} = const & , V_{bias} > V_{FD} \end{cases}.$$

The full depletion voltage can be then determined by both C(V) and $1/C^2(V)$ characteristics. Typical values for a silicon detector capacitance are between 100 and 500 fF for a single pixel (Eq. 4.10).
In addition, when producing a detector, one has to take into account the electric field resulting from the application of the bias voltage. Its maximum value is at the main junction and must be kept always below the breakdown voltage.

2.1 Signal formation in silicon sensors

Charged particles crossing a silicon detector produce ionizing and non-ionizing energy loss. The non-ionizing energy loss produces radiation damage only, while the ionizing one creates electron-hole pairs producing the signal, but may lead to radiation damage too.
Silicon has a band gap of 1.12 eV, which is one third of the mean energy needed to produce an electron-hole pair. At a temperature of 300 K, a minimum ionizing particle (MIP) produce electron-hole pairs with a most probable rate of 75 pairs every µm.

2.1.1 Induced current and Shockley-Ramo theorem

The signal of a silicon sensor is defined as the induced current on the electrodes; so, even if we talk about charge collection, signal does not start when the charge is collected, but just when the charge begins to move inside the sensor. Consequently, it stops when the whole charge is collected (the so called *charge collecting time*).
When a charge is produced between two electrodes we have two possibilities:

a) if its initial position is about in the middle between the electrodes, the charge induced on the two electrodes is approximately the same. The two electrodes are crossed by the same number of field lines (Fig. 2.1a).

b) if it is closer to one electrode, field lines will be denser on this electrode; thus the induced charge on it will be larger (Fig. 2.1b).

When a charge moves through the sensor, the induced charge on the electrodes changes.
The magnitude of the instant induced current on a single electrode i for a charge q is modeled by the *Shockley-Ramo's theorem* [14][15]:

$$I_i = -q\vec{v}(x) \cdot \vec{E_w}(x), \tag{2.2}$$

where $v(x)$ is the charge velocity and depends on the applied electric field E and on the charge position x. E_w is called *weighting field* and is defined as the virtual electric field which is determined by applying to the collecting electrode

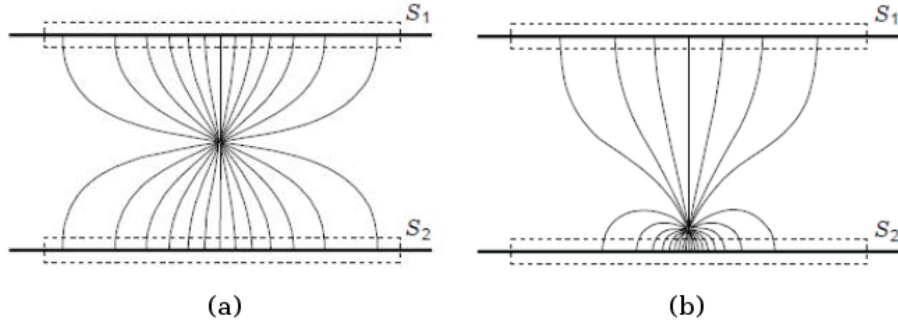

Figure 2.1: Field lines for a charge produced a) in the middle between two electrodes, b) nearer one of the two.

i the potential 1 and 0 to the others. The weighting field is only geometry dependent and it is independent of bias voltage.
With respect to a given electrode i, the currents induced by electrons and holes add up because they drift in opposite directions. For a parallel plate geometry, since drift velocity can be expressed in relation to the applied electric field E and the bias voltage V_b as

$$v = \mu E = \mu \frac{V_b}{d},$$

and the electric fields E and E_w are constant until the charge reaches the electrode, the induced current on the electrode i is:

$$I_i = -evE_w = -e\mu \frac{V_b}{d^2}, \tag{2.3}$$

where d is the detector thickness and e is the absolute value of electron charge. The current induced by all moving charges is then given by:

$$I = -eE_w \left(\sum_i v_{i,e} + \sum_i v_{i,h} \right). \tag{2.4}$$

If an electron-hole pair is produced at a given distance x from the anode (Fig. 2.2), charge collecting time for electrons and holes is:

$$t_{ce} = \frac{x}{v_e} = \frac{xd}{\mu_e V_b} \quad \text{for electrons,} \tag{2.5a}$$

$$t_{ch} = \frac{d-x}{v_h} = \frac{(d-x)\cdot d}{\mu_h V_b} \quad \text{for holes,} \tag{2.5b}$$

and the charge induced by their motion $Q = \int_0^T I(t)dt$ is then

$$Q_e = e\mu_e \frac{V_b}{d^2} \frac{xd}{\mu_e V_b} = e\frac{x}{d} \quad \text{for electrons,} \tag{2.6a}$$

$$Q_h = e\mu_h \frac{V_b}{d^2} \frac{(d-x)d}{\mu_h V_b} = e\left(1 - \frac{x}{d}\right) \quad \text{for holes.} \tag{2.6b}$$

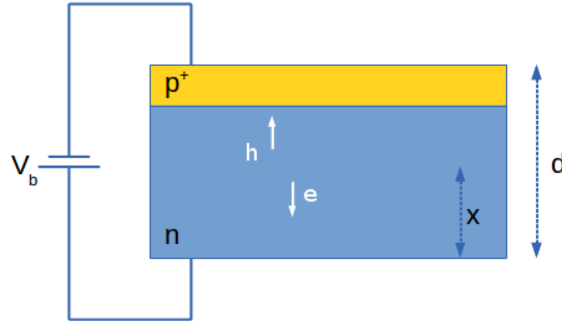

Figure 2.2: Electrons and holes drifting in a parallel-plates geometry.

The total charge $Q_e + Q_h$ contained in the current signal of the sensor is proportional to the energy deposited by the ionizing particle.

2.1.2 Charge carriers motion

Drift and weighting potentials

The Shockley-Ramo's theorem shows that the current induced on an electrode by charge carriers moving inside the sensor depends on the drift and weighting field. The electric field and the corresponding potential can be related to the charge density which gives rise to them. The electric field dependence on charge density ρ is expressed by the divergence

$$\vec{\nabla} \cdot \vec{E} = \frac{\rho}{\epsilon}, \tag{2.7}$$

where ϵ is the permittivity, and to the electric potential V by

$$\vec{E} = -\vec{\nabla} V. \tag{2.8}$$

For the drift potential, charge density is given by $\rho = eN$ where N is the dopant density and e is the electron charge. Then, the potential is related to the charge density by the so-called *Poisson's equation*

$$\nabla^2 V = -\frac{\rho}{\epsilon} \tag{2.9}$$

which, in absence of charge (as for the weighting field), becomes *Laplace's equation*

$$\nabla^2 V = 0. \tag{2.10}$$

Drift and weighting field are then evaluated by solving Poisson's and Laplace's equations.

Drift electric field

As said in Sec. 1.2.3, drift motion is one of the main contributions in charge carrier motion and drift velocity depends on the applied electric field. This electric field is in turn determined by depletion and bias voltage. By setting a bias voltage lower than the depletion voltage the sensor bulk is only partially depleted, causing an inefficient charge collection (Fig. 2.3).

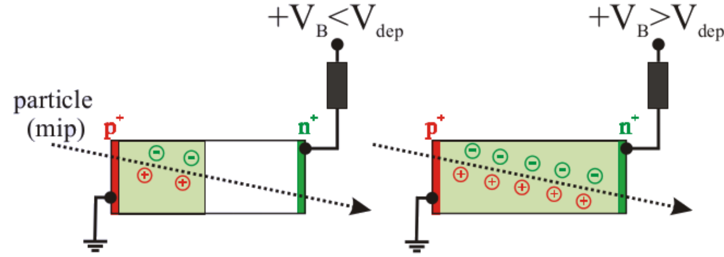

Figure 2.3: For bias voltage lower than depletion voltage the sensor is not fully depleted. The green zone is the depleted bulk (where electric field is present), while the white zone is the neutral non depleted bulk (without electric field): full charge collection is then possible only if $V_b > V_{depl}$.

For bias voltages higher than depletion voltage, the bulk is fully depleted and the overbias $V_b - V_{depl}$ adds a uniform offset given by $V_b - V_{depl}/d$ to the electric field, as shown in Fig. 2.4. The drift electric field is not uniform within the bulk:

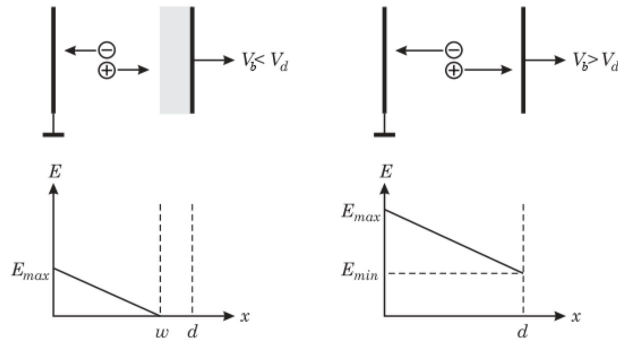

Figure 2.4: Distribution of the electric field for $V_b < V_{depl}$ and $V_b > V_{depl}$.

it starts from a minimum value at the backplane and reaches the maximum value at the readout electrode.
Being the drift velocity much influenced by the applied electric field, charges drifting to a lower electric field region will decelerate, while those drifting to a higher field region will accelerate until their velocity reaches the saturation value.
The uniformity of the drift electric field within the bulk, instead, is determined by depletion voltage: given a difference between bias and depletion voltage, a lower depletion voltage reduces the gradient of the electric field across the detector thickness, leading to a more uniform drift velocity. For example, if one

considers a sensor with V_{depl}= 50 V biased with V_b= 200 V and a second sensor with V_{depl}= 20 V biased with V_b= 170 V, even if the overbias $V_b - V_{depl}$= 150 V is the same in both cases, in the second sensor the drift field is more constant within the bulk, because the depletion voltage is lower.
In addition, one has to note that the signal of each detector depends on its geometry: different geometries lead to different electric field shapes and then to different $I(t)$ patterns.

Thermal diffusion

Charge carrier drift is affected by thermal diffusion, causing the spread of the charge distribution, with a resulting root mean square of

$$\sigma_D = \sqrt{2Dt} \tag{2.11}$$

after a drift time t, where D is the diffusion coefficient calculated in Eq. 1.13. The measured signal results then in a superposition of Gaussian distributions. Electrons created close to cathode and holes created close to anode are more affected by charge diffusion, due to a longer drift time.

2.1.3 Radiation damage

Tracking devices are placed in the inner part of high energy physics experiments, as close as possible to the interaction point, so they are designed and tested to operate at high radiation levels. The luminosity upgrade of LHC (HL-LHC) to 10^{35} cm^{-2}s^{-1} will translate into a further increase of the radiation dose afflicting detectors and electronics. For this reason, new radiation-hard detectors are being designed to stand at higher particle fluences.
Radiation may harm the silicon crystal and alter the position of atoms in the lattice. The entity of the damage varies with the particle energy: lower-energy charged particles create more point-like defects, while higher-energy charged particles and neutral particles (e.g. neutrons) lead to cluster-like damage.
Damage can concern either the bulk or the surface oxide:

a) bulk damage (also known as *displacement damage*) is due to Non-Ionizing Energy Loss (NIEL). It often translates into a change of the depletion voltage (higher values are needed to deplete the sensor) due to additional donors settling in the upper half of the band gap and acceptors in the lower, a reduction of charge collection efficiency due to electrons and holes trapping, and an increase of the leakage current.

b) surface damage is due to Ionizing Energy Loss (IEL) which causes the deposit of charges into the oxide structure or at the Si/SiO_2 interface; it leads typically to alterations in noise and breakdown voltage.

Charged particles, then, mainly damage the surface, while neutral ones (especially soft ones) damage the bulk [6]. For materials used in current detectors, the damage caused by different particles can be normalized to the *1 MeV neutron equivalent* NIEL damage n_{eq}: most fluence numbers are given using this normalization.
If the displacement caused by radiation damage is small, a modest amount of thermal energy ($E \sim kT$) may be enough to restore the atom to its original

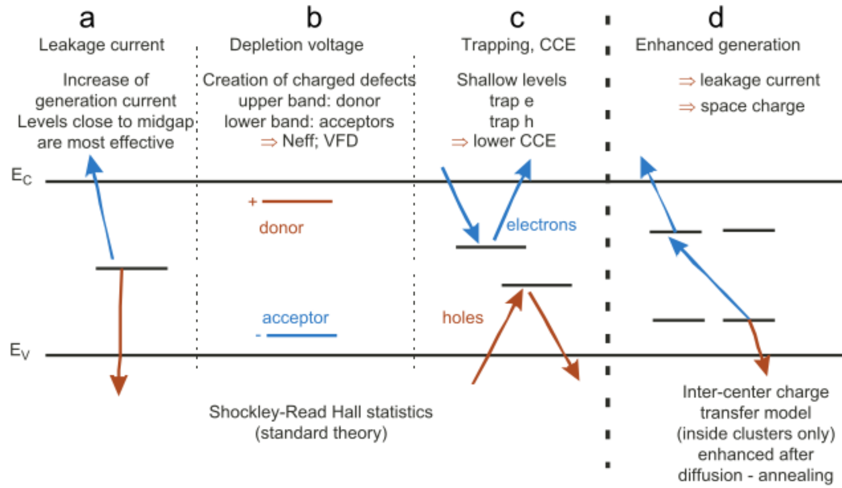

Figure 2.5: Different defect level locations and their effects.

configuration: it is possible then to recover from damage without heating the sensor, just keeping it at room temperature (T= 300 K). For displacements of higher entity, the sensors are kept at a certain temperature for a certain time with the process called *thermal annealing*: silicon conditions improve with increasing annealing time. It is to be noted that thermal energy is effective in repairing only the so-called *shallow level* damages, while in case of more severe damage the initial configuration cannot be completely restored. Hereunder will be shortly explained how operating parameters of a sensor change with irradiation.

Leakage current

Above $10^{14} n_{eq}/\mathrm{cm}^2$ the main problem which arises from radiation damage is the increase of the leakage current. Leakage current varies with particle fluence and time, as depicted in Fig. 2.6 [6], according to the relation:

$$\frac{\Delta I}{V} = \alpha \Phi_{eq}, \tag{2.12}$$

where V is the normalization volume, α is the *current-related damage rate* and Φ_{eq}, in n_{eq}/cm^2 is the 1 MeV neutron equivalent fluence. Mid-gap levels are responsible for the current increase, while annealing causes the current to decrease with time.

Depletion voltage

Depletion voltage depends on the effective charge N_{eff}, which evolves with fluence and time and becomes problematic at $10^{15} n_{eq}/\mathrm{cm}^2$ (Fig. 2.7 [6]). Irradiated sensors have a different number of acceptor and donor levels with respect to unirradiated. This variation may lead to an inversion of the material type, typically from n to p but also from p to p+. Hence, the depletion voltage exhibits an initial drop, after which it starts to rise (Fig. 2.7). This behavior can

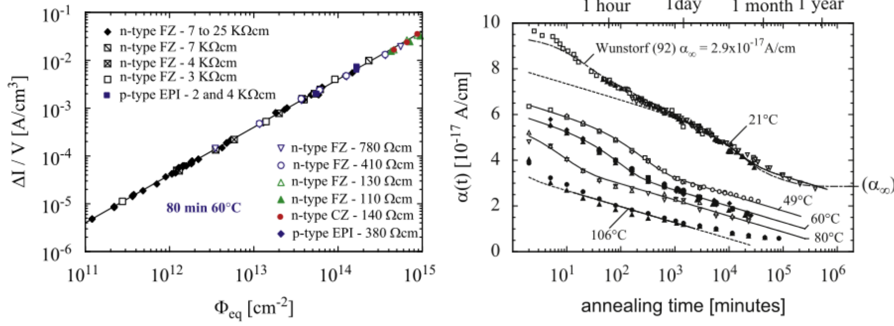

Figure 2.6: Leakage current variation with fluence and annealing time.

be parametrized by

$$N_{eff} = N_{D,0}e^{-c_D\Phi_{eq}} - N_{A,0}e^{-c_A\Phi_{eq}} - b\Phi_{eq}, \tag{2.13}$$

with $N_{D,0}$ and $N_{A,0}$ being the initial donor and acceptor concentrations, c_A and c_D the acceptor and donor removal rates, $b\Phi_{eq}$ the acceptor creation term.
In addition, N_{eff} is subject to a temperature dependent diffusion with time:

$$\Delta N_{eff}(\Phi_{eq}, t, T) = N_{C,0}(\Phi_{eq}) + N_A(\Phi_{eq}, t, T) + N_Y(\Phi_{eq}, t, T), \tag{2.14}$$

where $N_{C,0}$ is the stable term, N_A and N_Y are the annealing short-term and second-order long-term respectively.

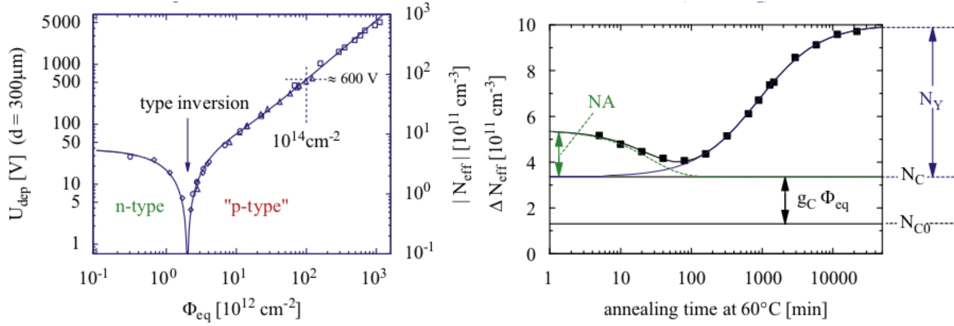

Figure 2.7: Depletion voltage variation with fluence and annealing time.

Charge trapping

Damage by irradiation creates trapping centers inside the silicon: the concentration of these new trapping centers N_i can be approximated by the linear relation

$$N_i = \Phi_{eq} g_i f_i(t) \propto \frac{1}{\tau_{eff}}, \tag{2.15}$$

where the product $g_i \cdot f_i(t)$ describes the evolution of annealing with time.
This worses the Charge Collection Efficiency (CCE), as described by:

$$Q_{e,h}(t) = Q_{0_{e,h}} e^{-\frac{t}{\tau_{eff}}}. \tag{2.16}$$

2.2 Front-end electronics

A crucial element for a detector signal shape is the effect of front-end electronics, which amplifies, shapes the sensor signal and converts it into a digital sequence. The signal produced by a sensor is typically a short current pulse: since the total charge, given by the integral of the signal current $I(t)$, contains the information about the energy deposited in the sensor, one needs to integrate the current. This is possible by integrating on a capacitance, by using a *charge sensitive* amplifier or an integrating ADC (Analog-to-Digital Converter) after amplification of the pulse.
When integrating on the input capacitance, the circuit in Fig. 2.8 has to be considered, (where C_{det} is the sensor capacitance, C_i and R_i are the amplifier input capacitance and resistance [43]. If the time constant of the circuit, given

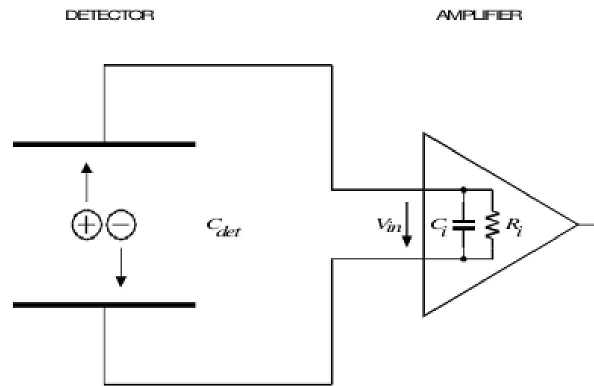

Figure 2.8: Integration on input capacitance.

by the product $R_i \cdot (C_{det} + C_i)$ is significantly longer than the collection time t_c, the peak voltage at the amplifier input is [17]

$$V_{in} = \frac{Q}{C_{det} + C_i}, \tag{2.17}$$

and depends on the input and sensor capacitances.
However, the sensor capacitance may be subject to variations since it depends on the sensor geometry and on the bias voltage (the sensor bulk may be not completely depleted). Therefore it is preferable to use systems whose response does not depend on the sensor capacitance, for example by using a charge sensitive amplifier, where the sensor capacitance is much lower than the amplifier input capacitance $C_{det} \ll C_i$.

2.2.1 Charge sensitive amplifier

The charge sensitive amplifier (CSA) is a transimpedance operational amplifier which converts the current pulse into a voltage signal, which can be measured, for example with an oscilloscope. It is often used as preamplifier stage in a front-end chain. The scheme of a charge sensitive amplifier is shown in Fig. 2.9: in the ideal case, it is characterized by a high input impedance $R_i \to \infty$ and by a feedback capacitance C_f, while the feedback resistance (parallel to C_f) is

supposed to be infinite and then omitted. The current pulse is integrated on

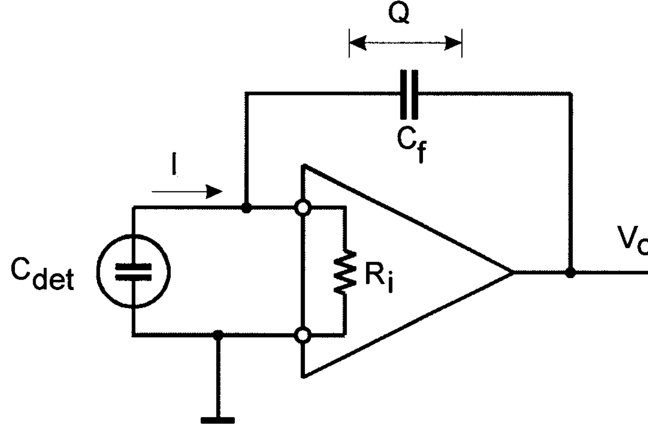

Figure 2.9: Ideal charge sensitive amplifier.

the feedback capacitance C_f and the resulting output voltage is a step

$$V_o \propto \frac{Q}{C_f} \tag{2.18}$$

and does not depend on C_{det}.
A more realistic amplifier, instead, responds to a current pulse with a finite speed and then its response affects the pulse shape: the output voltage cannot be a step but is moduled by a negative exponential and depends on the circuit time constant τ, since the internal capacitances of the amplifier have to charge up before allowing the output voltage to change.
Moreover, the signal also includes the noise on the signal itself and on the baseline (electronic noise). Therefore, measurements of peak amplitude include both signal amplitude and fluctuations due to noise.

2.2.2 Noise

The noise in a silicon detector system plays an essential role, since the signals are very low and it affects both the peak signal and the time distribution. The current signal I of a sensor of thickness d, produced by n carriers of charge e moving with a certain velocity v is

$$I = \frac{nev}{d}, \tag{2.19}$$

and the total noise can be estimated from the fluctuations of this current, given by the total differential

$$\langle dI^2 = \left(\frac{ne}{d}\langle dv\rangle\right)^2 + \left(\frac{ev}{d}\langle dn\rangle\right)^2. \tag{2.20}$$

It is composed by two statistically uncorrelated contributions:

- velocity fluctuations, i.e. *thermal noise*,
- number fluctuations, i.e. *shot noise*.

Both contributions provide a purely random noise, and are called *white* noise sources, since their noise power per unit bandwidth is constant.
A good detector should have a high *signal-to-noise ratio* (SNR), obtained from a reasonable compromise between a *large signal*, which implies low ionization energy, i.e. a reduced band gap, and a *low noise*, which implies a small number of intrinsic charge carriers and a larger band gap. This is optimized by a band gap of $E_g \approx 6$ eV. For this reason, the best material is certainly the diamond, but due to the high cost it is not feasible to use diamonds to build large area detectors.
It is to be noted that the noise at the preamplifier input appears amplified at the output but reduced by the presence of the negative feedback: the signal-to-noise ratio at the amplifier output depends then on the feedback network.
Many effects contribute to the overall noise in a silicon detector (Fig. 2.10). Since the signal processing integrates the signal current and the noise to give a quantity proportional to the charge, the output noise can be characterized by an equivalent charge referred to the input, the so called *Equivalent Noise Charge* (ENC), defined as the input charge for which the signal-to-noise ratio S/N is equal to 1 [16]. The Equivalent Noise Charge can be written keeping into account various contributions due to leakage current (ENC_I), sensor capacitance (ENC_C), sensor parallel resistor (ENC_{R_p}), sensor serial resistor (ENC_{R_s}):

$$ENC = \sqrt{ENC_I^2 + ENC_C^2 + ENC_{R_p}^2 + ENC_{R_s}^2}. \tag{2.21}$$

The main contribution is the one due to the sensor capacitance; which is linearly

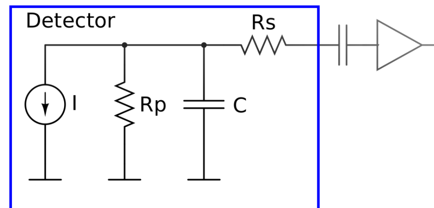

Figure 2.10: Contributions to noise in a sensor

correlated to the equivalent noise charge [3]

$$ENC_C = a + b \cdot C, \tag{2.22}$$

where a and b are amplifier design parameters and C is the equivalent capacitance of the detector at the amplifier input.
Since noise is part of the signal, amplifying the signal implies amplifying the noise too. To avoid this, it is needed to put a threshold in the readout electronics in order to separate the effective signal from thermal fluctuations: the choice of the threshold value has to reduce the effect of noise and avoid efficiency loss at the same time.

2.2.3 Shaping

Signal shaping (or *pulse processing*) has two conflicting objectives [16]:

1. reducing the bandwidth to match the measurement time, since a too large bandwidth increases the noise without increasing the signal;

2. avoiding signal *pile-up*, i.e. constraining the pulse width in order to measure successive signal pulses without overlapping. Reducing the pulse duration increases the signal rate but leads to heavier electronic noise contribution.

Shaping can be done internally to the preamplifier stage or by using of a RC-CR shaper (eventually in a sequence RC-(CR)^n). A front-end sequence with preamplifier (first stage) followed by a shaper is shown in Fig. 2.11 [18]: the charge sensitive amplified receives the signal from the sensor, the second stage is a CR (high-pass) filter or *differentiator* which brings the CSA output back to the baseline with a quick and sharp fall, while the third stage is a RC (low-pass) filter or *integrator* which softens the signal variation around the maximum. The

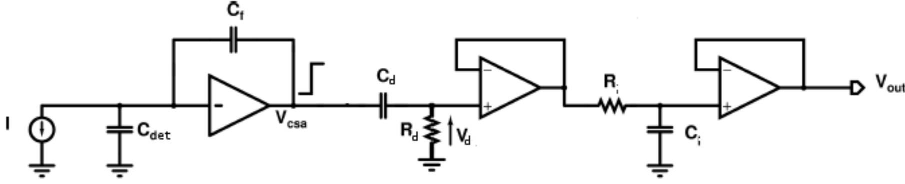

Figure 2.11: Front-end amplifier example.

output signal of the full chain is then

$$V_o(t) = \frac{Q}{C_f} \frac{\tau_d}{\tau_d - \tau_i} \left(e^{-\frac{t}{\tau_d}} - e^{-\frac{t}{\tau_i}} \right), \tag{2.23}$$

being $\tau_d = R_d C_d$ and $\tau_i = R_i C_i$ the differentiator and integrator time constants. The shaper converts then a narrow pulse to a broader pulse to reduce electronic noise, and the new shape of the signal reaches a gradually rounded maximum within a time called *peaking time* or *shaping time* in order to facilitate the peak amplitude measurement.
The noise at the output of a front-end chain with a CR-RC shaper, with a shaping time t_s, can be evaluated by considering the circuit of Fig. 2.12 The equivalent noise charge ENC at the output is:

$$ENC^2 = \left(\frac{e^2}{8} \right) \left[\left(2eI_d + \frac{4kT}{R_b} + i_{na}^2 \right) t_s + (4kTR_s + e_{na}^2) \frac{C_{det}^2}{t_s} + 4A_f C_D^2 \right], \tag{2.24}$$

composed by three contributions

- *current noise* (first term) independent of detector capacitance, increases with shaping time $\propto t_s$

- *voltage noise* (second term) $\propto C_{det}^2 / \sqrt{t_s}$

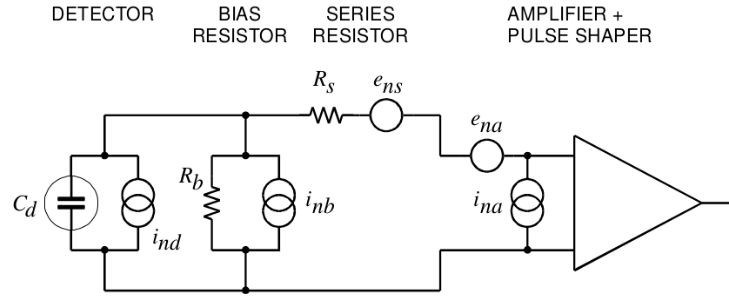

Figure 2.12: Equivalent circuit of a detector front-end for noise analysis.

- *1/f noise* (third term) independent of shaping time, $\propto C_{det}^2$

where e is the electron charge, I_d is the sensor bias current, R_b is the input shunt resistance, k the Boltzmann constant, T the temperature in K, i_{na} and e_{na} are the input current and voltage noise spectral densities and A_f is a noise coefficient specific of the device ($\sim 10^{-10} - 10^{-12}$ V^2). The first factor ($e^2/8$) normalizes the noise to the signal gain.

2.3 Silicon sensor production

The production of a silicon sensor starts from a silicon wafer [22]. The process to obtain a wafer consists of many steps: the starting point is pure sand melted with coke at about 1800 ℃ to form the "metallurgical grade silicon", which is then cooled and exposed to hydrochloric gas. The so obtained $SiHCL_3$ is then distilled and purified: with a process called *Chemical Vapor Deposition* (CVD), pure silicon is deposited and then can be cast into a polycrystalline silicon rod (polysilicon), which is made up of small crystals.

2.3.1 Monocrystalline growing

At this point, polysilicon needs to be converted into monocrystalline silicon: it consists of silicon whose crystal lattice has no discontinuities and it is at the base of the electronic industry. It can be prepared either intrinsic or doped (by adding small percentages of other elements such as boron and phosphorus). Different methods can be used to grow monocrystalline silicon, for example *Float Zone* (FZ) and *Czochralski* processes [28].

Czochralski silicon

The most common growing technique is the Czochralski method: it allows to produce wafers with very high resistance to thermal stress and high oxygen concentration with considerable advantages in terms of production speed and costs.
High purity polysilicon is melted with additional dopants into a rotating quartz (SiO_2) crucible Fig. 2.13 and a monocrystalline silicon seed is placed on the surface. The seed is gradually drawn upwards while rotating and this draws the molten silicon, which solidifies into a continuous crystal. The quartz crucible gradually dissolves during the process and releases a large quantity of oxygen into the melt, which strengthens the crystal.

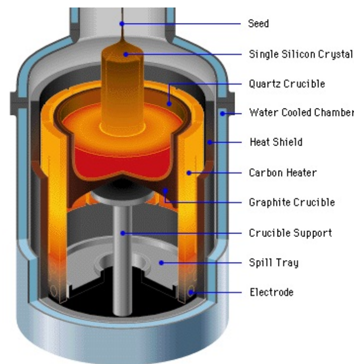

Figure 2.13: Czochralski crystal puller.

Float Zone silicon

Float Zone silicon has very low concentrations of light impurities, such as carbon, oxygen and nitrogen (this last increases the mechanical strength of the

wafer and is intentionally added in the growth procedure). This method takes place into vacuum or inert gaseous atmosphere and starts with a high-purity polycrystalline rod and a single-crystal seed, facing each other in vertical position (Fig. 2.14). Both seed and rod are partially melted with a radio-frequency field while rotating and the seed is drawn toward the lower part of the rod which is fused. A necking process is used to reach the designed diameter and the molten silicon solidifies into a single-crystal cylinder.
For the very low impurity concentrations, FZ silicon can achieve higher purity and resistivity with respect to Czochralski one.

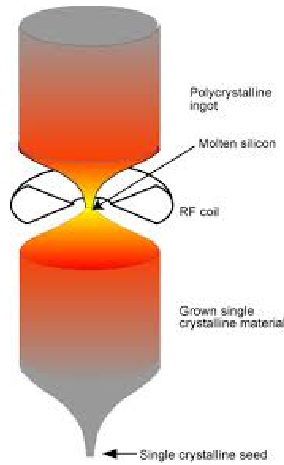

Figure 2.14: Schematic view of the Float Zone process.

2.3.2 From wafer to sensor

With a polished single-crystal wafer it is possible to start the fabrication of the sensor (Fig. 2.15a) [20]:

1. The first step is using a doped monocrystalline wafer for the bulk (for example n-type)

2. The wafer surface is passivated with a SiO_2 layer with an approximate thickness of ∼200 nm, obtained for example by growing with thermal oxidation at a temperature between 800 and 1200 ℃.

3. Then the oxide is partially removed by selective photolithography etching to create the base of electrodes (for example strips): the lithography process [19] is schematized in Fig. 2.15b. First, the oxide is covered by a *photoresist*, which is a photosensitive organic material [22], then a mask is used to select the surfaces where the oxide has not to be removed and the whole complex is exposed to UV light. The exposure to light causes a chemical change that allows some of the photoresist to be removed by a special solution, called "developer". The most common type of photoresist is called *positive photoresist* and becomes soluble in the developer when exposed.

At this point, the oxide layer which is not protected by photoresist is removed by a chemical agent (liquid or plasma) with a process called *etching* and then the photoresist is ready to be removed from the substrate by means of a chemical agent (either stripped by a liquid called "resist stripper" or oxidized by a plasma containing oxygen).

4. Electrodes and backplane have then to be doped by either thermal diffusion or ion implantation. For example, boron is used to create p^+ strips (with a concentration of about $N_A \approx 5 \cdot 10^{16}$ cm^{-2}) and Phosphorus for the ohmic n^+ backplane.

5. After the ion implantation, the *annealing* process is used to cure radiation damage and activate the dopants: this procedure consists in keeping silicon at a temperature of about 600 ℃ for a certain time and allows to incorporate the dopant impurities into the silicon lattice.

6. The front side is then metalized (aluminum) by sputtering or CVD

7. The excess of metal is removed by photolithography and the non-covered areas are etched

8. The backplane is fully metalized with annealing at ~ 450 ℃ in order to reach a better adherence between metal and silicon

The wafer is then ready to be cut.

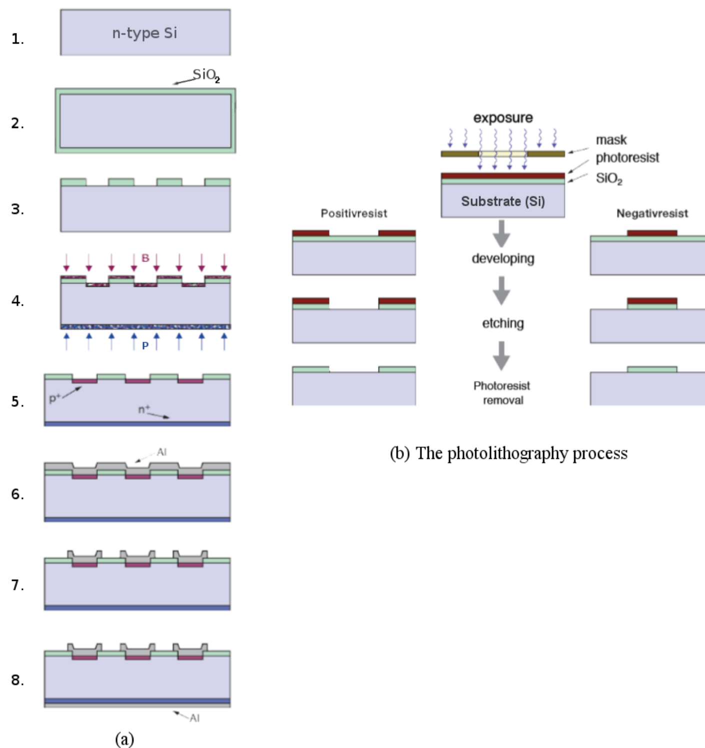

Figure 2.15: Steps for silicon sensor fabrication.

2.4 Geometries for silicon detectors

Several detector geometries are used in high energy physics. This section illustrates some of the most used architectures as well as new trends in silicon detectors.

2.4.1 Pad

Pads are the simplest devices: they contain only a single large diode (mm^2 to cm^2) with one ore more guard rings (see below).
This geometry is not able to provide a position resolution and is mainly used for basic tests like I(V) and C(V) curves.

2.4.2 Microstrip

Microstrip detectors are made on a large number of strip-shaped identical structures arranged in a plane, providing high resolution in the dimension [10] orthogonal to the strip direction (Fig. 2.17). Such a structure is characterized by the strip *pitch* p, defined as the orthogonal distance between the centers of two adjacent parallel detector elements (the repetition unit). The pitch determines the spatial resolution of the detector [12]: in the case of a simple binary readout the resolution σ_x is given by

$$\sigma_x = \frac{p}{\sqrt{12}}, \tag{2.25}$$

but in most cases, the analog readout of all channels allows to improve the spatial resolution, using the charge shared between neighboring strips due to capacitive coupling. For tracks generating signals on two strips, the position is often evaluated by calculating the centroid x as

$$x = \frac{x_1 h_1 + x_2 h_2}{h_1 + h_2}, \tag{2.26}$$

where x_1 and x_2 are the positions of the two strips, and h_1, h_2 are the signals on the two strips, respectively. Spatial resolution with analog readout also depends on the signal-to-noise ratio [6]:

$$\sigma_x \propto \frac{p}{SNR}. \tag{2.27}$$

Typical pitch values are in the range of ten to one hundred micrometers (here the name "microstrip").
A common strip detector is made of highly doped p^+ ($N_A \approx 10^{15}$ cm^{-3}) strips covered by aluminum, which work as readout electrodes on a n ($N_D \approx 1 \cdot 10^{12} - 5 \cdot 10^{12}$ cm^{-3}) bulk, forming several p^+n junctions. An additional n^+ backplane layer is applied to improve ohmic contact.

Operating principle

In a p^+-on-n strip detector electrons produced in the bulk by an ionizing particle drift to the n^+ backplane, while holes drift to the p^+ strips. The charge collected by the strips is then induced by capacitive coupling to the aluminum readout strips and then pre-amplified by a readout chip. The capacitor can be integrated

on the sensor (AC-coupled) or not [35], as in DC-coupled detectors (Fig. 2.16 [10]).
Microstrip detectors can be built as single- or double-sided devices. The readout can be done in channels connecting several strips: here the distance between two readout channels is called *readout pitch* p_r and is an integer multiple of the geometrical pitch p. Connection to bias voltage is for example achieved by

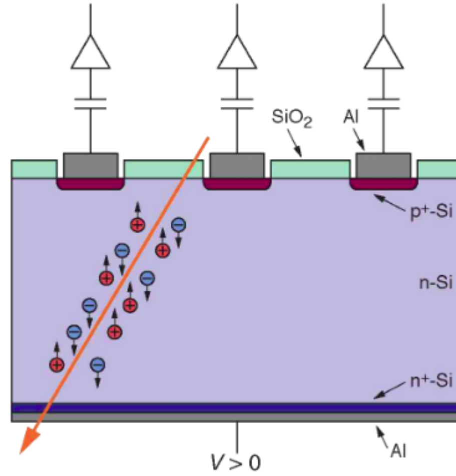

Figure 2.16: Schematic view of a strip detector with p^+ strips and ohmic n^+ backplane, DC-coupled.

polysilicon resistors called *bias resistors*.

Bias ring and guard ring

A microstrip detector is surrounded by a *bias ring*, connecting strips to each other by a polysilicon *bias resistor*, ensuring them the same bias voltage.
Outside the bias ring one or more *guard rings* are placed. They allow to shape the electric field at the detector edges and to prevent the diffusion of surface currents.

Double sided microstrip

With a microstrip detector, it is possible to get a 2D spatial information by segmenting both p^+ and n^+ electrode planes into orthogonal strips. For example, p^+ gives the x coordinate collecting electrons, while n^+ gives the y coordinate collecting holes: this allows to get an additional information with the same amount of material.
However, the double-sided layout has some disadvantages such as a more technical complexity, higher production costs and ambiguity issues due to the production of ghost hits when more than one track is read out [10].

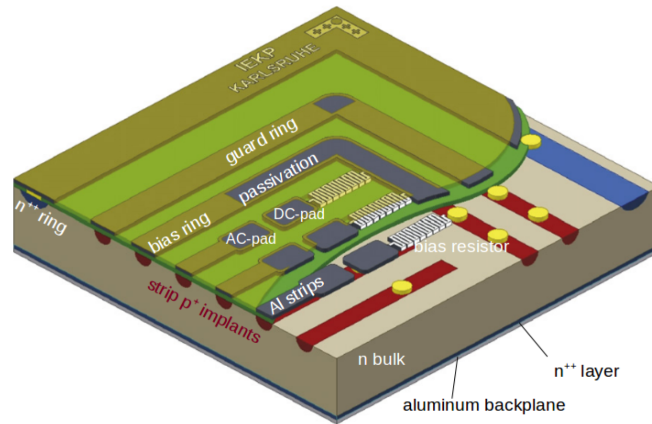

Figure 2.17: 3D view of a microstrip detector.

Figure 2.18: Two real tracks forming two ghost hits in a 2D-microstrip detector.

2.4.3 Pixel detectors

To avoid position ambiguity, *pixel detectors* have been designed. They provide non-ambiguous hits when more than one particle leaves a track.

Hybrid

In a hybrid pixel layout the readout chip is placed over the silicon sensor, and bump-bonds ensure electrical connection between each pixel and its electronics channel.
A typical pixel device has a small detector capacitance (≈ 300 fF for each pixel), and a low leakage current (≈ 1 nA/mm^3 for each pixel [24]).
Disadvantages are the high number of channels and electrical connections, and the high power dissipation. Moreover, bump-bonding is an expensive technology, limits the pixel size and may cause multiple scattering.

Monolithic

In monolithic pixel detectors, the sensor and the readout electronics are integrated on the same silicon wafer. However, sensors need a high-resistive silicon

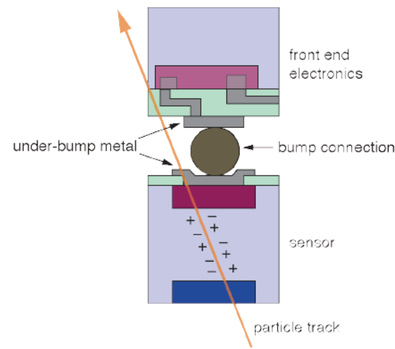

Figure 2.19: Pixel sensor bump-bonded to electronics.

(low-doped), while electronics need low-resistive silicon (heavily-doped).
In Monolithic Active Pixel Sensors, MAPS-CMOS, the electrons produced in an epitaxial silicon layer with thickness of 15-20 µm are collected by a n-well electrode. Since the epitaxial layer is low-resistive, the charge is collected from a non-depleted zone: electrons move by diffusion (not by drift) and the collecting time is higher (∼100 ns).
MAPS-SoI (Silicon on Insulator) are relatively faster, allowing to collect charge by drift. This is possible because electronics and sensor are kept separated with an oxide layer.

2.4.4 APD

An *Avalanche Photodiode* (APD) is a silicon device which makes use of the photoelectric effect to convert photons (typically visible or near-infrared) into an electric signal. Since visible photons create only one electron-hole pair, the signal produced by a simple photodiode is quite low. This signal can be enlarged by using an internal gain, based on the avalanche mechanism.
The zone producing the avalanche is a pn junction with high electric field, designed so as to provide internal gain by *impact ionization* (Sec. 3.2.2). APD operates as follows (Fig. 2.20a):

1. a photon enters the diode and produces an electron-hole pair
2. if reverse biased, the external electric field forces the electron to drift
3. while drifting, if the electron crosses a region with a field of enough strength, it is accelerated and then its energy increases. If the electron energy is high enough, it can ionize producing another electron-hole pair
4. the electron produced by ionization accelerates and can ionize further
5. this gives rise to an *avalanche ionization process* with gain of about $10^4 - 10^6$ for typical APD dimensions (between 5 mm × 5 mm and 1 cm × 1 cm)

The diode can tolerate the avalanche, as long as it has a limited duration and the induced current is not too high. However, the capability of these sensors to

resolve single photons is quite poor: for every incident photon the diode produces a current pulse with a uniform amplitude and thus it is not possible to know if more than one photon hit the sensor. In addition, the gain of APDs is limited by fluctuations of the avalanche multiplication.
APDs in particle physics are used, for example, in the electromagnetic calorimeter of the experiment CMS at CERN.

Silicon Photomultiplier

Silicon Photomultipliers (SiPM) are single-photon detectors, built from an APD array arranged into cells on a common silicon substrate (Fig. 2.20b). Each single photodiode operates in Geiger mode (G-APD) and is connected in parallel to the others with a quenching resistor. Gain is in the range of $10^5 - 10^7$, and further amplification is not required. With respect to simple APDs, SiPMs are not affected by avalanche fluctuations and are able to resolve single photons with a very low noise [25].
The response of a SiPM is very fast (less than 500 ps), due to a very thin depletion layer and the short duration of the Geiger discharge development, which makes SiPMs useful for fast timing [26]. The typical size of a silicon photomultiplier is 1.5 mm × 1.5 mm of surface and 300 µm of thickness.

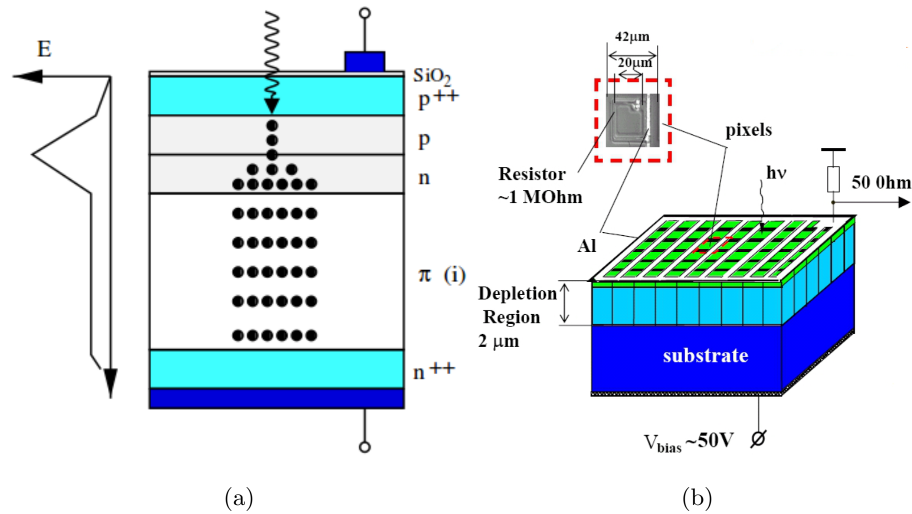

(a) (b)

Figure 2.20: a) Operating principle of an APD. b) Silicon Photomultiplier.

Chapter 3

Innovative silicon detectors

A luminosity upgrade of the LHC is planned for the year 2023. The new High-Luminosity LHC will reach luminosity of 10^{35} cm^{-2}s^{-1} and a neutron-equivalent fluence of $\Phi_{eq} \sim 10^{16}$ cm^{-2}. Therefore, more precise sensors,with more higher tolerance for radiation are needed.
In this section new tracking detector layouts for the next LHC upgrade will be described. We will focus our attention on two architectures: 3D and Ultra-Fast.

3.1 3D pixel detectors

3D pixel detectors were proposed for the first time in 1997 by S. Parker and fabricated at Stanford by C. Kenney [36].
The bulk of a 3D sensor is vertically crossed by electrodes (Fig. 3.1) of type p and n, which are organized in alternate columns: this allows to reduce the distance between opposite electrodes with respect to present planar sensors, reducing the depth of the depletion zone and subsequently the depletion voltage (between 10 and 30 V instead of 100 V).
Moreover, by decoupling the electrode distance from the substrate thickness, keeping the same amount of collected charge, it is possible to reach higher inter-electrode electric fields and then to increase the carriers velocity. Due to a shorter drift distance, passing-through electrodes also accomplish a faster detector signal response and a reduction of trapping centers (Sec. 2.1.3), resulting in a radiation harder sensor.

3.1.1 3D layouts

Since their introduction, many different layouts have been designed (Fig. 3.2 [3]). They can differ in

a) type of electrode: junction (pn) or ohmic contact (n^+-n, p^+-p),

b) single-sided or double-sided column etching,

c) column depth,

d) number of readout columns per pixel, determining the inter-electrode distance,

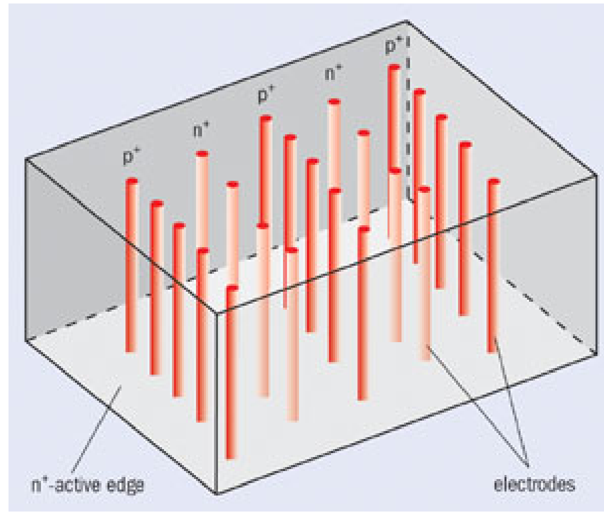

Figure 3.1: Scheme of a 3D sensor.

e) in the case of non-fully passing-through columns, presence of a structure implemented on the backside.

A typical bulk doping is p^{--}, being more radiation hard then n^{--} and not subject to type inversion when irradiated. The first 3D sensors were produced

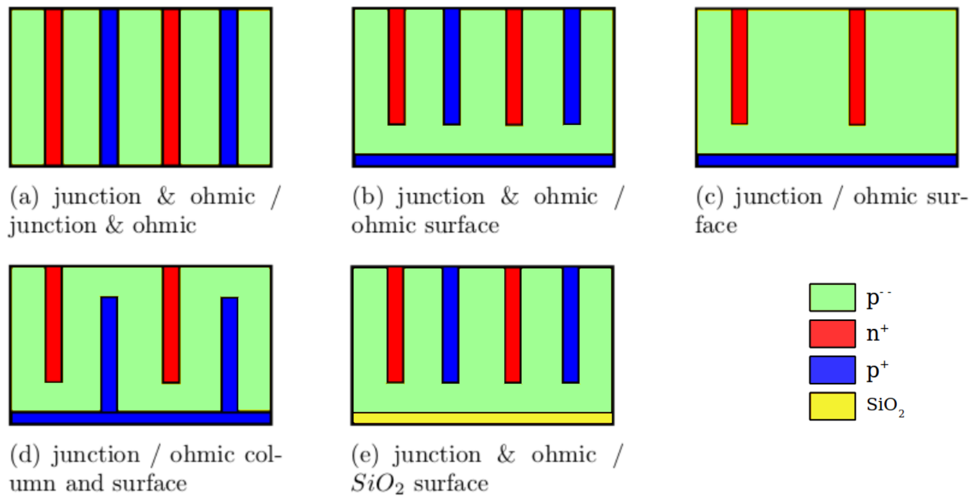

(a) junction & ohmic / junction & ohmic

(b) junction & ohmic / ohmic surface

(c) junction / ohmic surface

(d) junction / ohmic column and surface

(e) junction & ohmic / SiO_2 surface

Figure 3.2: 3D layout options.

with fully penetrating electrodes (*full-3D*) at Stanford and later by SINTEF in Norway (a), with both electrodes being etched from a single side, this technology requires a support wafer which later needs to be removed.
In addition, the so called *active edge* can be implemented, with the aim of re-

ducing dead areas at the edges and allowing full collection efficiency near the physical edge of the device.
FBK in Trento and CNM in Barcelona produced the so called 3D-DDTC (Double side Double Type Column) sensors, in order to simplify the fabrication process: junction electrodes are etched from the front while ohmic ones are etched from the back side of the wafer (d). The first 3D-DDTC by FBK showed electrodes not completely passing through, causing a low-field zone between the end of the column and the wafer surface. A later production used fully passing through electrodes.
Electrodes are generally hollow (Fig. 3.3) or partially filled with polysilicon.
Nevertheless, the development of 3D technology has to deal with issues like:

- increased pixel capacitance due to the electrode configuration, which may lead to an increased output noise;
- increased production costs with respect to planar technology due to the etching procedure to make deep hole-like electrodes with small diameter called *Deep Reactive Ion Etching*;
- low-field zones between same doping type electrodes causing charge collection inefficiency.

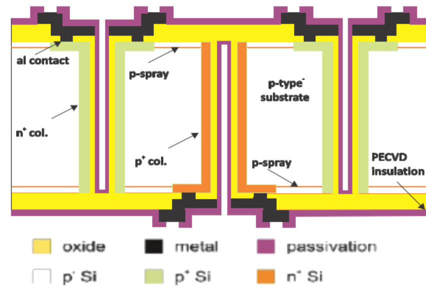

Figure 3.3: Cross-section of a 3D-DDTC sensor by FBK with electrodes penetrating into a p-type substrate [30].

3.1.2 Pixel configurations

Different pixel configurations for the 3D technology have been developed to be used with the present CMS readout chip PSI46v2, which has a pixel cell of $150 \times 100\ \mu m^2$. They differ in the number of electrodes per pixel cell, as seen in Fig. 3.4 [30]:

- 1E: single n-type electrode
- 2E: two n-type electrodes
- 4E: four n-type electrodes

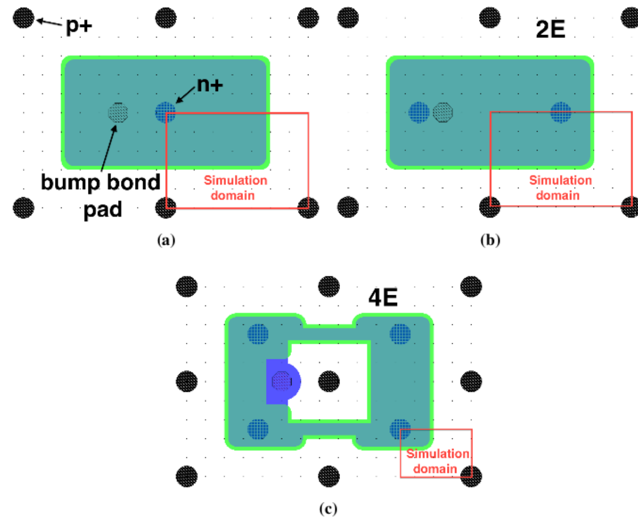

Figure 3.4: 3D pixel configurations: a) 1E, b) 2E, c) 4E.

3.1.3 Active and slim edges

One of the goals of 3D detectors is to reduce the edge inefficiency or even to remove it by using active edges.
In planar detectors the insensitive surface is very wide (about 14% of the surface area for the pixel sensor used in ATLAS at CERN), since edges show a last electrode field bulging, as well as occasional micro-cracks. Moreover, the area reserved to guard rings is significant, compared to sensor overall surface
To overcome this problem, planar sensors are usually staggered over many layers, to avoid inefficient coverage. This arrangement, however, forces particles to cross additional layers of material.
Active edges will allow to avoid this superposition of detector layers, being electrodes themselves (Fig. 3.5a [30]). First, trenches are etched around the margins of the sensor and then doped (either n or p). With active edges a support wafer is needed, forcing the production to be single-sided.
An alternative to active edges are *slim edges*, which can slim down the inactive region to ¡ 100 µm, reducing the bulging of the electric field by inserting a multiple alignment of ohmic columns (Fig. 3.5b).

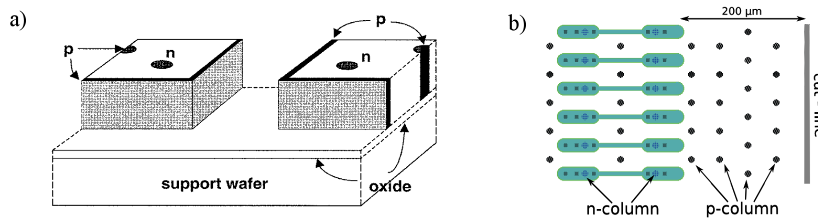

Figure 3.5: a) Schematic view of two 3D sensors with active edge bonded to the support wafer; b) scheme of the slim edge for a 3D sensor for ATLAS.

3.2 Ultra Fast detectors

Ultra-Fast silicon detectors (UFSD) have been proposed with the aim of enhancing concurrent space-time resolution [31]. At present, it is not possible to measure both space and time with good accuracy: precise tracking detectors have poor time resolution and vice versa.
UFSD have been intended to give a simultaneous space and time measurement with a granularity of about 10 µm and 10 ps, respectively. In order to increase the time resolution the detector should be able to provide a shorter signal, therefore the collection time should be reduced by employing a thinner sensor. However, in a thin sensor, an ionizing particle produces less e-h pairs, leading to a small signal: thus, an internal gain is needed, which allows to multiply the initial charge and then to operate with a smaller collected charge.
Applications for such a device range from high energy physics to mass spectrometry and PET tomography.
In this section the operating principle of UFSD, their properties and expected performance are presented, as well as the concept of charge multiplication in silicon sensors.

3.2.1 Operating principle

In silicon, as mentioned in Sec. 1.2.3, electrons drift velocity saturates to a value of $\sim 10^7$ cm/s. This means that, in a sensor of about 300 µm of thickness collecting electrons, charge collecting time is $\sim$3 ns. Thus, a faster sensor can be obtained by reducing the sensor thickness. Since a thinner sensor leads to a smaller collected charge, this will be not enough to reach an adequate signal-to-noise ratio and then a good time resolution. This means that, in order to build a detector which can be considered "fast", it has to be thinner than average sensors but also able to work with a smaller collected charge. For this reason, an internal charge multiplication mechanism is used to enlarge the signal and enhance timing measurements.
This mechanism is modeled by the *impact ionization model* for silicon, which is based on the *Townsend Avalanche* of gases (Fig. 3.6). Under the effect of an accelerating electric field, free electrons produce electrical conduction through a gas by ionizing its molecules and producing an avalanche multiplication. The avalanche mechanism was studied first in a gas environment because the first particle detectors where it was analyzed were wire chambers.
It is possible to model the multiplication of N_0 initial electrons drifting through a silicon path length d with high electric field with the law:

$$N_{TOT} = N_0 e^{\alpha d} = N_0 \cdot g \tag{3.1}$$

Since this charge multiplication is similar to that of gases, the α coefficient can be identified with the *first Townsend coefficient*, expressing the number of electron-hole pairs generated per unit length by an electron moving from cathode to anode. The theoretical dependence of the charge multiplication factor α with the electric field is supposed to be exponential (Fig. 3.7), while the real behavior needs to be confirmed by measurements. Using Eq. 3.2 it is possible to evaluate α for a given electric field: at $E_{max} = 270$ kV/cm, $\alpha = 0.746$ µm^{-1} [33]:

$$\alpha_{e,h}(E) = \alpha_{e,h}(\infty) \exp\left(-\frac{\beta_{e,h}}{|E|}\right) \tag{3.2}$$

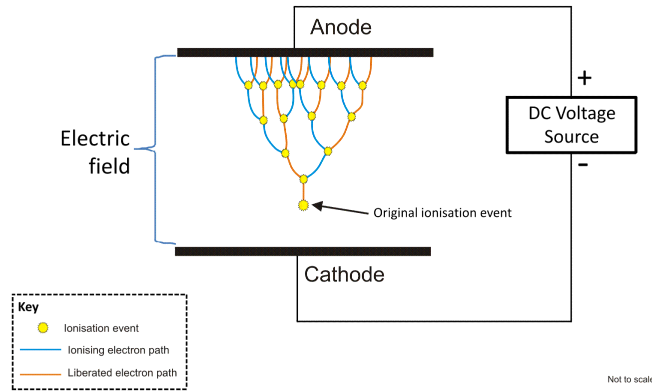

Figure 3.6: Townsend avalanche in gases.

For electric fields above ∼400 kV/cm, both electrons and holes ionize but

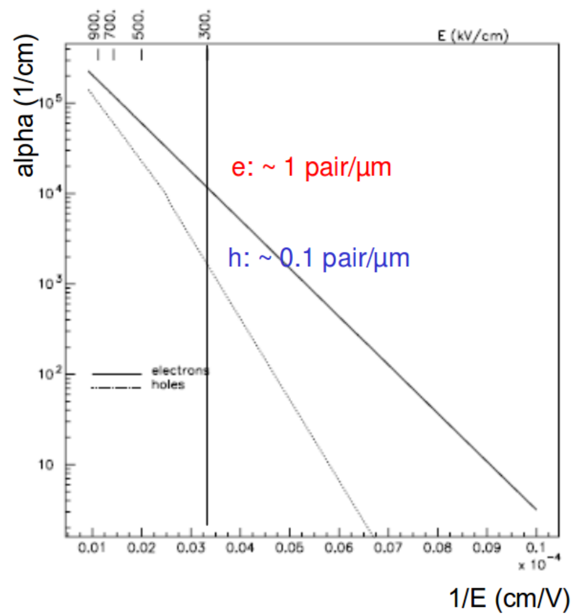

Figure 3.7: Charge multiplication factor in silicon.

the avalanche enters the geiger mode and infinite gain would lead to sensor breakdown.

3.2.2 Impact ionization model

With the advent of semiconductor detectors, the Townsend avalanche model has been extended to the solid state case. The mechanism of charge multiplication resulted to be the same, and the most general case is called *impact ionization model* [27].

Impact ionization is a process taking place in non-equilibrium environments with a large applied electric field: one energetic charge carrier can lose energy by the creation of other charge carriers. In semiconductors, an electron from conduction band or a hole from valence band gains under the effect of the applied electric field so much energy that it produces an electron-hole pair by colliding with an electron in the valence band and excites it to the conduction band. Avalanche photodiodes (APDs), for example, are based on this effect.

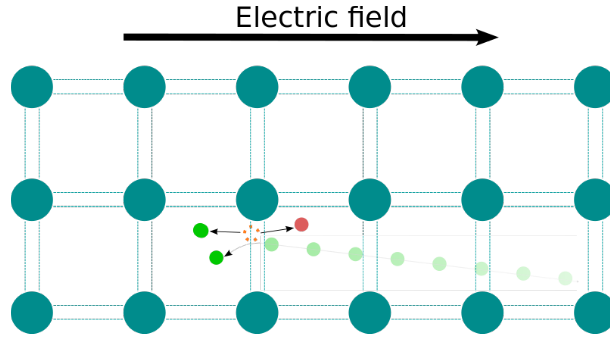

Figure 3.8: An example of an incoming electron impact ionizing to produce a new electron-hole pair.

The total rate of electron-hole pairs production due to impact ionization (*gain*) is evaluated by [23]

$$g = \alpha_n \frac{|\vec{J_n}|}{q} + \alpha_p \frac{|\vec{J_p}|}{q}, \tag{3.3}$$

where $\vec{J_n}$ and $\vec{J_p}$ are the electron and hole current densities, respectively. α_n and α_p are the electron and hole impact ionization rates, defined as the number of pairs produced by carriers motion along the electric field direction. The behavior of impact ionization rates with electric field is described by the empirical relation:

$$\alpha_n = A_n e^{-\left(\frac{B_n}{E}\right)^{\beta_n}}, \tag{3.4a}$$

$$\alpha_p = A_p e^{-\left(\frac{B_p}{E}\right)^{\beta_p}}. \tag{3.4b}$$

$A_n, A_p, B_n, B_p, \beta_n, \beta_p$ are parameters whose values are still subject of debate. According to this model, impact ionization coefficients increase rapidly with increasing electric field, as shown in Fig. 3.9: this means that the device breakdown voltage can be strongly reduced by the presence of a high localized electric field. In addition, since in silicon the impact ionization coefficient for electrons α_n is about one order of magnitude greater than that for holes, it is reasonable to neglect α_p when solving Poisson's equation for the drift potential.
Moreover, the expression for impact ionization coefficient can be further approximated by

$$\alpha_{eff} = a_\alpha E^7. \tag{3.5}$$

This expression is particularly useful when analytically deriving the solutions for breakdown voltage. α_{eff} is called *effective impact ionization coefficient*, and a_α is a constant whose value for silicon is about $1.8 \cdot 10^{-35}$ cm^6 V^{-7}.

In addition, the electric field strength dependence on bias voltage limits the achievable multiplication factor α. At the breakdown electric field value E_{max} = 350 kV/cm, it is possible to reach a maximum multiplication of ~1 µm^{-1} for electrons and ~0.1 µm^{-1} for holes.
The dependence of the α parameter on the electric field strength and then on the sensor bias introduces another design limitation. The best possible timing performance has to be achieved through the optimization of geometry, biasing and gain to get the shortest charge collection time. Up to now, a moderate

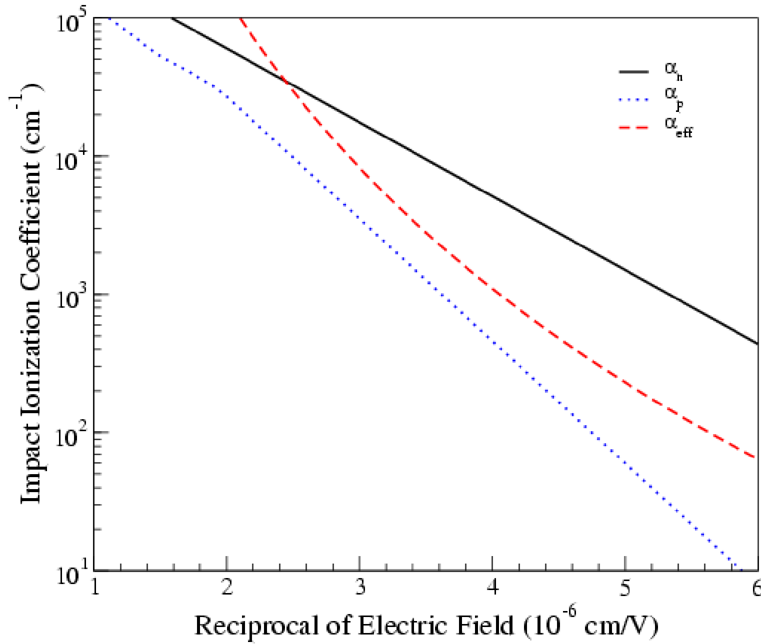

Figure 3.9: Impact ionization coefficients behavior with reciprocal of electric field.

charge multiplication have been observed in irradiated silicon detectors as an effect of type inversion (Sec. 2.1.3), converting n-doped silicon to p and p-doped regions to p$^+$. It has been seen that this new high-doped p$^+$ regions induced a small gain, tending to compensate for the efficiency loss due to charge trapping, typical of irradiated sensors. The intent of the R&D research for developing UFSD is instead to use it "constructively" to increase the signal magnitude of a very thin sensor.

3.2.3 Sensor thickness

Studies have been made to choose the better range for the sensor thickness [40]

Thickness	Backplane Capacitance		Signal	Coll.	Gain required	
[µm]	Pixels[fF]	Strips [pF/mm]	[e$^-$]	Time [ps]	2k e$^-$	12k e$^-$
1	250	5.0	35	13	57	343
2	125	2.5	80	25	25	149
5	50	1.0	235	63	8.5	51
10	25	0.50	523	125	3.8	23
20	13	0.25	1149	250	1.7	10.4
100	3	0.05	6954	1250	0.29	1.7
300	1	0.02	2334	3750	0.09	0.5

The highlighted field indicates detector thickness values which, presently, match realistic gain, backplane capacitance and good time resolution: sensor thickness has to be about 50 µm, corresponding to a collecting time of about 1 ns.
In order to get a faster detector the pixel geometry has to be preferred to the strip one because it gives the chance to reach moderate gain, small capacitance and fast charge collection at the same time.
Furthermore, the overall layout needs to be adapted to the different purposes of the sensor and to the respective field geometries.
Thin epitaxial sensors (Fig. 3.10a) [31] are made of a low-resistivity highly doped n^{++} electrode on a high-resistivity p epitaxial layer of silicon, deposited on a thick low-resistivity p^{++} bulk. Readout chip is bump bonded to the sensor. This architecture is very effective in charged particles detection but is not able to detect visible photons because the sensible epitaxial layer is placed between two thick low-resistivity layers.

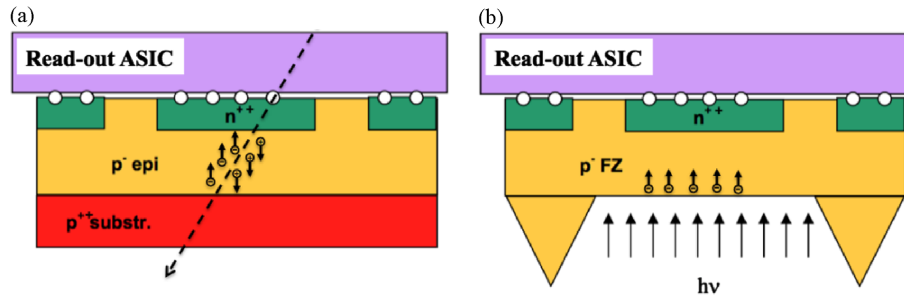

Figure 3.10: UFSD bump bonded to readout: a) epitaxial sensor for charge particles detection; b) FZ sensor for photon detection.

To detect visible photons, a backlit back-etched thin sensor have been studied: it is manufactured by removing via etching mechanism the excess of material from the backside of a high-resistivity *Float Zone* (FZ) wafer. With this technique it is possible to reach a thickness of 15 µm and to refine the removal via selective etching.

3.2.4 Electric field

The choice of an appropriate electric field is a crucial point in the development of UFSD: the field should be high enough to determine charge multiplication

and sufficiently low to prevent breakdown.
At present, this avalanche mechanism has been observed in sensors irradiated with high hadron fluences (above $10^{15} n_{eq}/\text{cm}^2$) because the operating electric field is high enough to achieve charge multiplication without reaching electric breakdown. Unirradiated sensors instead reach breakdown at lower electric field values: one of the requirements is then to get charge multiplication at voltages lower than the breakdown value.
For this reason, an update to the typical implant profile has been proposed: making the n^{++} implant of a planar segmented sensor deeper and wider and inserting below this implant an additional p^+ diffusion layer (Fig. 3.11, 3.12) it is possible to get a reduced field at the edges and a large n^{++}-p^+-p^- junction at the center of the electrodes. When reverse-biasing this region, a high and localized electric field is established. This can be adjusted by altering depth and doping concentration of the new p^+ layer, in order to obtain a uniform multiplication mechanism across the electrode.
According to this scheme, CNM started to develop sensors with low charge multiplication called *Low Gain Avalanche Detectors* (LGAD), further described in Sec. 6.2.

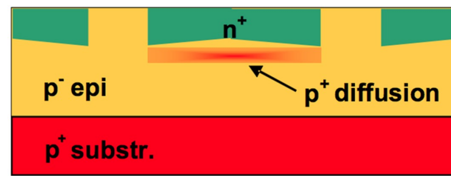

Figure 3.11: Scheme of p-epi with p^+ diffusion layer produced by CNM.

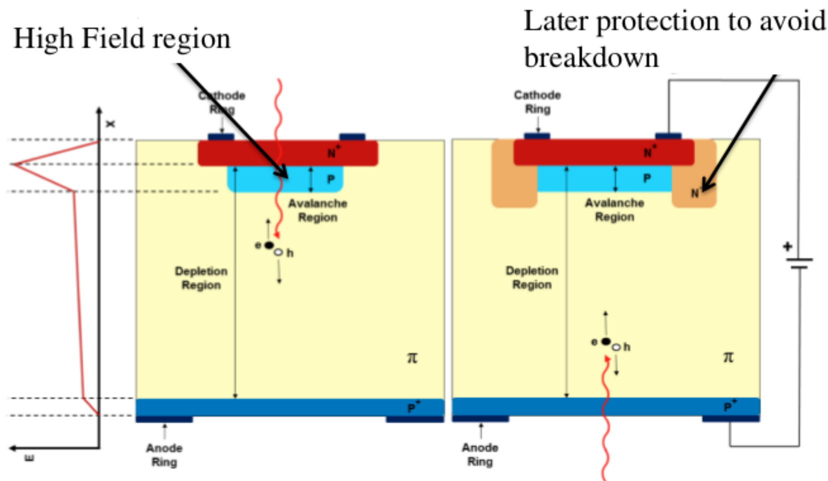

Figure 3.12: Proposed changes to sensor shape to avoid breakdown.

3.2.5 Applications of Ultra-Fast detectors

As said before, current semiconductor detectors only provide optimal spatial accuracy, while they lack in resolving time. A time resolution of 10 ps would be a decisive improvement in the field of silicon sensors. Space-time precise detectors as UFSD could fulfill many areas of interest, ranging from particle physics to medical applications [31]:

1. *Particle Tracking.* A precise event timing could reduce the number of random coincidences and increase the overall efficiency. By adding a fourth dimension to each point it is possible to cut down combinatorial background contribution.
2. *Vertexing.*
3. *Time of Flight (ToF).* Used to identify particles, as well as in many commercial applications such as medical PET , mass spectroscopy, 3D images reconstruction, and robotic vision.
4. *Counting Particles.* Medical physics and material science would take advantage of high rate and precise particle counting: it would be possible to have a direct and accurate measurement of the dose absorbed by patients in hadron therapy and to improve x-ray experiments.

Chapter 4

Time Measurements

The aim of UFSD is to measure time with an accuracy of 10-20 ps [41][42]. To illustrate how a time-tagging detector works, Fig. 4.1 shows a simplified scheme for such a detector: the current signal of a sensor, for example a pixel, is sent to a preamplifier (charge sensitive amplifier) which shapes the signal and converts it to a voltage one. This output voltage is then compared to a fixed threshold V_{TH} by a discriminator to determine the time of arrival.
The output of the discriminator changes value when the amplitude of the input signal crosses a certain threshold. It is used to decide whether the input signal is actually from a particle and to start the time measurements.
The simplest pulse discrimination is called *leading edge triggering* and provides a logic signal if the pulse amplitude is higher than the threshold. The discriminator output is then converted to a binary string by a TDC (Time To Digital Converter).

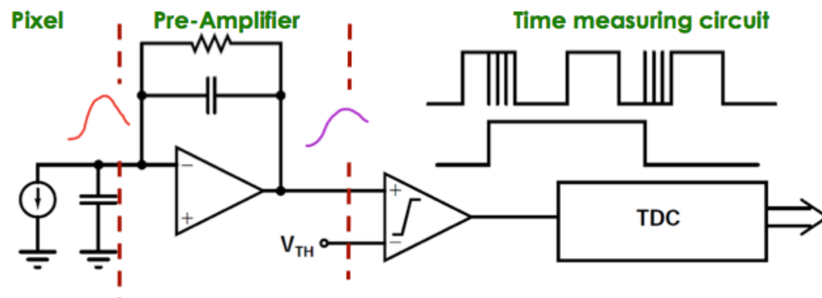

Figure 4.1: Main components of a time-tagging detector.

4.1 Timing circuits

In this section different types of discrimination circuits are described:

- **Leading edge (or single threshold)**: the discriminator sets the logical 1 when the signal is over the threshold and 0 when it goes under the threshold. This kind of discrimination most suffers the undesirable effect due to signals of different amplitude: *time walk* (Sec. 4.2.1).

- **Multiple threshold**: in order to reduce time walk, a second threshold is added. The logical 1 is set when signals cross both thresholds.

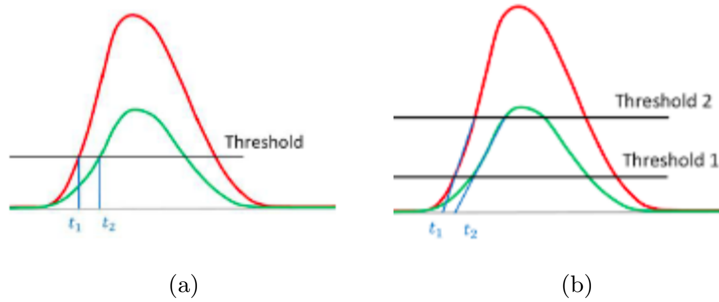

(a) (b)

Figure 4.2: Threshold discrimination: a) single, b) double.

- **Constant Fraction Discriminator (CFD)**: this kind of discriminator performs the mathematical operation of finding the maximum of a pulse by finding the zero of its slope, typically in the case of signals with short rise time t_r. It looks at the whole signal and emits the logic pulse when the input signal reaches a certain fraction of the peak value. A constant fraction discriminator operates as follows: the incoming signal is split into three components. One is delayed by a time $t_d \ll 0 \leq t_r$, connected to the inverting input of a comparator and eventually multiplied by a small factor, the second is connected to the non-inverting input of the comparator and the third to the non-inverting input of another comparator (Fig. 4.3). The outputs of both comparators are then sent to an AND gate (Fig. 4.4).
  CFD is immune to time walk under the assumption that the signals of different amplitudes have the same shape.

- **Waveform sampling**: converts a continuous waveform (signal) to a discrete signal through an ADC (Analog to Digital Converter). This technique is very precise and it is mostly used when the rate of incoming signals is low, as it takes several microseconds per event.

Constant fraction discrimination is probably the best compromise between accuracy and fast timing.

4.2 Time resolution

The aim of our analysis is to estimate the time resolution for various sensor types and geometries.
Time resolution σ_t can be written as the sum of three terms:

1. Time walk,

2. Jitter,

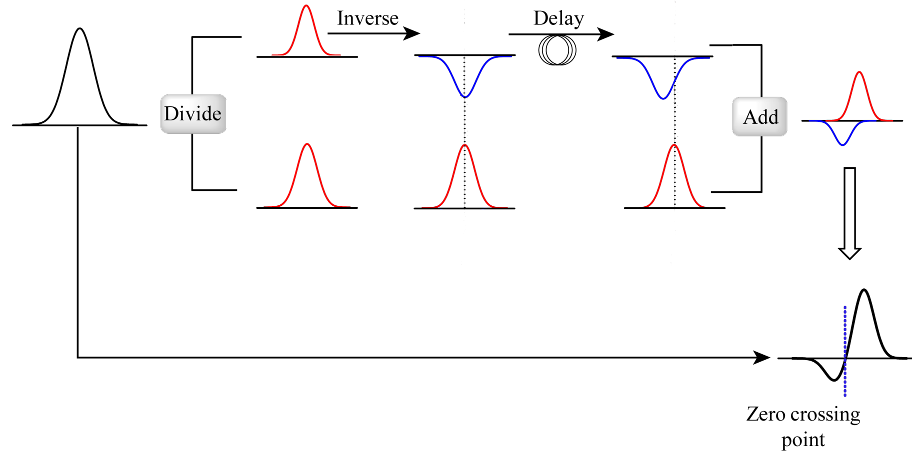

Figure 4.3: Operating principle of the Constant Fraction Discriminator.

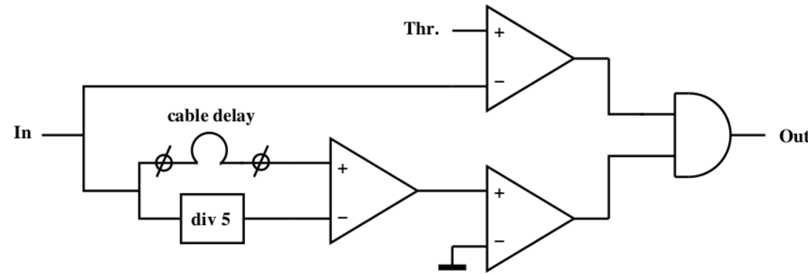

Figure 4.4: Basic functional diagram of a constant fraction discriminator.

3. TDC binning:

$$\sigma_t^2 = \sigma_{TW}^2 + \sigma_j^2 + \sigma_{TDC}^2. \tag{4.1}$$

Out of these three terms, the last one (TDC binning term TDC_{bin}), given by the width of the TDC least significant bit (LSB), can be neglected since it introduces a fixed value of uncertainty given by $\sigma_{TDC} = TDC_{bin}/\sqrt{12}$ and presently $TDC_{bin} \simeq 20$ ps.

4.2.1 Time walk

Time walk is the main drawback of single threshold discrimination. The term indicates that, given a threshold, the time needed to cross it is shorter for larger signals than for smaller ones. Time walk affects the output of discriminators, generating a delay on the firing of the discriminator, which depends on the signal amplitude, as can be seen in Fig. 4.5a. If we consider for simplicity a linear signal (Fig. 4.5b), with amplitude S and rise time t_r, it crosses the threshold V_{TH} with

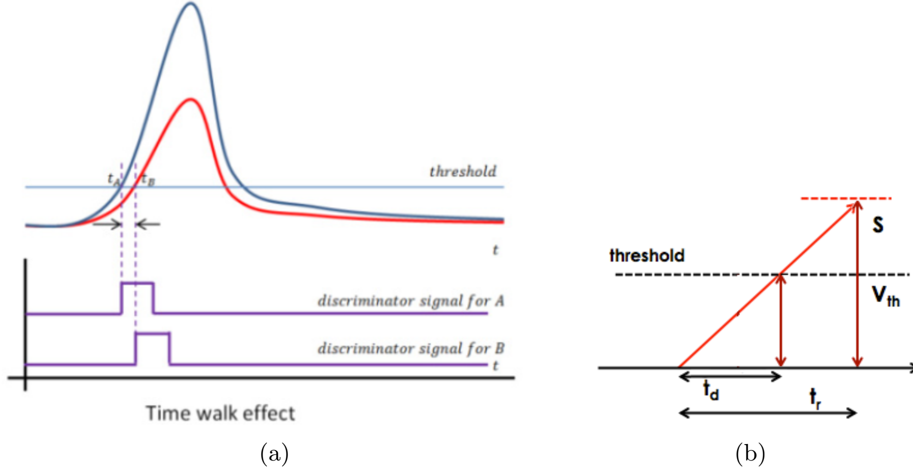

(a) (b)

Figure 4.5: a) Time walk and its effect on discriminator output. b) Delay time t_d achieved when a linear signal is crossing the threshold.

a delay t_d which can be expressed by

$$t_d = \frac{t_r V_{TH}}{S} \tag{4.2}$$

It is possible to evaluate the uncertainty due to time walk by considering the delay time distribution: being S_0 the most probable value for the signal amplitude, if one sets the value of the threshold to $V_{TH} = S_0/3$ and assumes a signal variability range $S_0/3 < S < 5S$, the delay can then vary from t_r to $t_r/15$. Time walk is defined as the root mean square of the delay distribution:

$$\sigma_{TW} = [t_d]_{RMS} = \left[\frac{t_r V_{TH}}{S}\right]_{RMS}. \tag{4.3}$$

Time walk effect is certainly minimized by choosing the lowest possible value for the threshold. It is a common usage to express the threshold value referred to the noise at the output of the preamplifier. In this analysis we set the threshold value to $V_{TH} = 10 \cdot N$, where N is the noise at the preamplifier output.
Moreover, the signal amplitude S in silicon detectors follows a Landau distribution: according to [38], in thinner detectors the average energy loss per micron in the silicon bulk decreases, while the width of the distribution spreads (as shown in Fig. 4.6). The most probable value of the Landau distribution (MPV) is given by

$$MPV = 0.027 \ln d + 0.126, \tag{4.4}$$

and its width ΔS with respect to the signal amplitude S

$$\Delta S/S = 0.7079 \cdot d^{-0.266}. \tag{4.5}$$

Therefore, since thin sensors have smaller energy loss per micron and larger distribution variations, they suffer time walk effects more than thick ones. Given a detector thickness, it is possible to generate the proper Landau distribution by

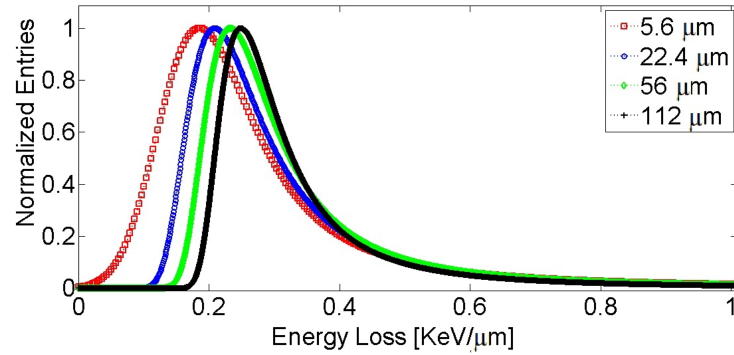

Figure 4.6: Average energy loss per micron of a ionizing particle in silicon layers of different thicknesses.

using Eq. 4.4 and 4.5: for example, the appropriate distribution for a thickness of 200 µm is shown in Fig. 4.7a. As a consequence, one can obtain the value of the time walk for a given shaping time (Fig. 4.7b): for $t_r = 5500$ ps, the time walk varies from 200 to 500 ps, according to the value of the threshold. Time walk

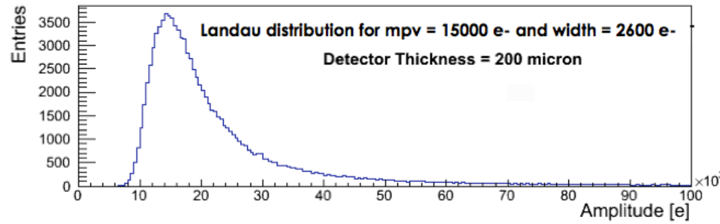

(a)

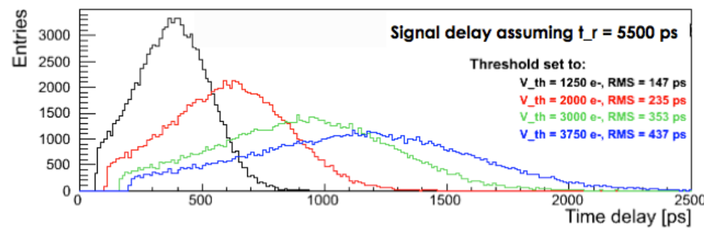

(b)

Figure 4.7: a) Landau distribution for a sensor thickness of 200 µm. b) Delay distributions for different values of V_{TH}, assuming a shaping time t_r of 5500 ps.

effect can be reduced if the signal amplitude is known: in this case, it is possible to easily implement a correction function. The more common techniques are Time Over Threshold (TOT) and Constant Fraction Discrimination (described in Sec. 4.1).

4.2.2 Jitter

A noisy signal (Fig. 4.8 [44]) changes the comparator firing time. *Jitter* is directly proportional to the noise of the system N and inversely proportional to the slope of the signal around the value of the comparator threshold. If one assumes a constant slope

$$\frac{dV}{dt} = \frac{S}{t_r}, \tag{4.6}$$

the time uncertainty introduced by jitter is:

$$\sigma_J = \frac{N}{dV/dt} = \frac{t_r}{S/N}. \tag{4.7}$$

Time resolution then can be parametrized by:

$$\sigma_t^2 = \left(\frac{t_r}{S/N}\right)^2 + \left(\left[\frac{t_r V_{TH}}{S}\right]_{RMS}\right)^2 + \left(\frac{TDC_{bin}}{\sqrt{12}}\right)^2, \tag{4.8}$$

where S is the signal, N is the noise at the preamplifier, V_{TH} is comparator threshold, t_r is preamplifier shaping time (assuming that integration and differentiation time constants are equal).

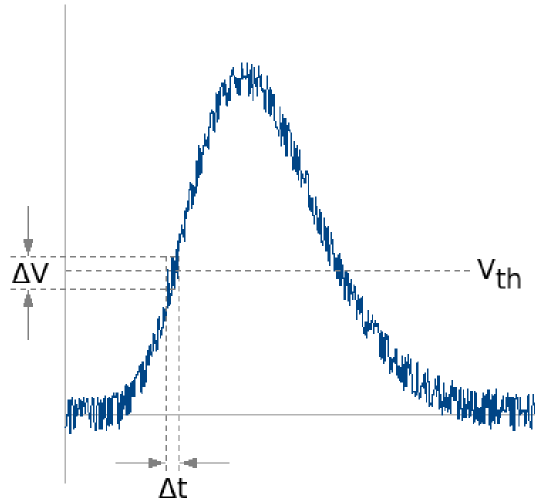

Figure 4.8: Jitter induced by noise.

4.2.3 Noise estimate

To make a reasonable estimate of the noise N at the preamplifier (charge sensitive amplifier) output, one can consider the equivalent noise charge equation at a shaper output (Eq. 2.24) [39]. It can be assumed that, for low values of t_r, the main contribution to the noise is given by the voltage term (Fig. 4.9)

$$N \propto \frac{C_{det}}{\sqrt{t_r}}, \tag{4.9}$$

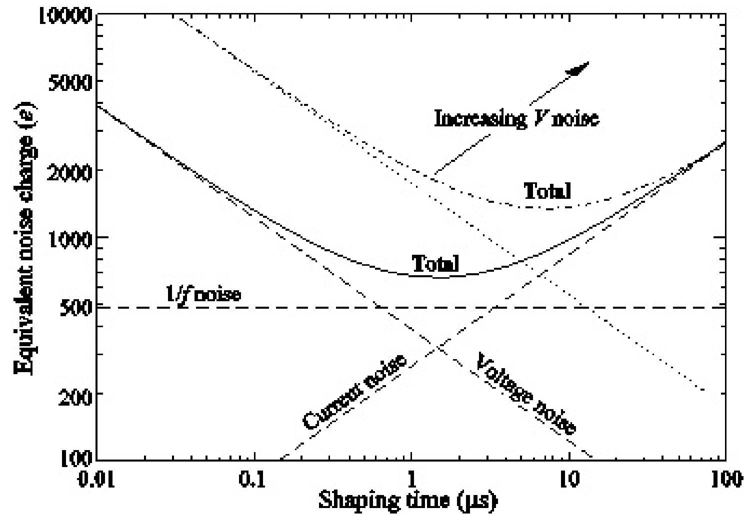

Figure 4.9: Equivalent noise charge as function of shaping time. For low shaping time values it is dominated by the voltage contribution.

where the detector capacitance is formed by three terms accounting for the back-plane capacitance, the neighbors contribution, and constant stray contribution

$$C_{det} = \epsilon_{Si}\epsilon_0 \frac{l^2}{d} + 0.2 \text{ fF/µm} \cdot 4l + 50 \text{ fF}. \tag{4.10}$$

The value of the preamplifier rise time t_r has to be chosen by taking into account several effects: it depends on the noise N of the system, on the amount of charge collected and on the possibility to produce ghost hits on neighboring sensors. Shaping time should be of the same order of magnitude of the collection time: the signal S increases until $t_r \sim t_c$ and reaches a constant value for $t_r > t_c$

$$\begin{cases} \sigma_t \propto \frac{C_{det}}{\sqrt{t_r}} & , t_r < t_c \\ \sigma_t \propto C_{det} \cdot \sqrt{t_r} & , t_r > t_c \end{cases}.$$

Fig. 4.10 shows how the time resolution varies with the shaping time for a pixel detector of thickness 100 µm, pixel size 100 µm and a collection time of 1250 ps: for shaping time equal to collection time, time resolution is minimized.

4.2.4 Timing with UFSD

Eq. 4.8 shows that σ_t decreases with increasing signal S, since it is proportional to S^{-1}. Another possibility to improve the time resolution is to increase the signal-to-noise ratio, which is achievable with detectors providing larger signals if the noise remains almost the same.
With respect to standard pixel detectors without gain, Ultra-Fast devices exhibit a longer charge collecting time, being the superposition of the original charge carriers drift time plus the time needed for the holes produced in the gain layer to drift toward the p^{++} electrode.

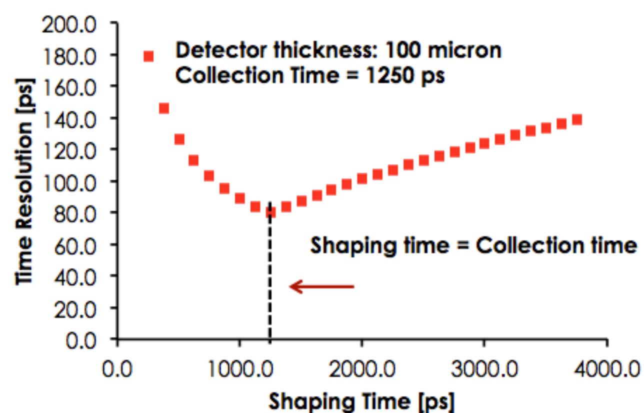

Figure 4.10: Time resolution vs preamplifier shaping time for a pixel detector with thickness 100 µm and a pixel size of 100 µm.

Moreover, considerations about time resolution which have been presented in this chapter, are only valid for a uniform charge distribution, for which constant fraction discrimination is effective in correcting amplitude variations, while this is not true if the signal shape varies, for example due to non uniformity in charge distribution (Sec. 5.1.3) [42].

Chapter 5

UFSD Simulator

To effectly design the electronic circuits needed to reduce time uncertainties, it is necessary to know very well the current signals produced by the particles in the sensors. To this end, we developed a software simulator, *Weightfield 2.0*.

5.1 The Weightfield 2.0 program

Our purpose is to develop a tool to study signals in Ultra-Fast Silicon Detectors. In particular, we want to investigate the behavior of gain in UFSD prototypes and to compare laboratory measurements with simulation.
Weightfield 2.0 is based on an existing program called *Weightfield* by HEPHY Vienna [37], which simulates the current signal in a silicon detector with microstrip or pad geometry. The original program has been complemented with the addition of new simulation options and adapted to be able to simulate Ultra-Fast detectors by introducing charge multiplication.
The program is implemented in C++ language within the ROOT framework and makes use of the ROOT Graphical Interface (TGUI). The graphical interface allows the user to select simulation parameters such as type of incident particles, sensor geometry and doping, depletion and bias voltages and to display drift and weighting potentials, as well as current signals and oscilloscope output.

5.1.1 Potentials calculation

Drift and weighting potentials are calculated by solving Poisson's and Laplace's equations, as said in Sec. 2.1.2. The program performs the calculation by discretizing the equation on a grid with mesh size of $\Delta h = 1$ µm. For this purpose, the spatial derivatives of the potentials in equation $\nabla^2 v = -f$ are approximated with a Taylor approximation for both vertical and horizontal coordinates to $v(x_i \pm 1) = v(x_i \pm \Delta h)$, which lead to [37]

$$\begin{aligned}\nabla^2 v(y_j, x_i) = \frac{1}{\Delta h}[v(y_j, x_{i+1}) + v(y_j, x_{i-1}) + v(y_{j+1}, x_i) + v(y_{j-1}, x_i) + \\ - 4v(y_j, x_i)] + \mathcal{O}(\Delta h^2),\end{aligned} \tag{5.1}$$

and to a discretized Poisson's equation

$$v(y_j, x_{i+1}) + v(y_j, x_{i-1}) + v(y_{j+1}, x_i) + v(y_{j-1}, x_i) - 4v(y_j, x_i) = -(\Delta h)^2 f_{j,i}. \tag{5.2}$$

The equation 5.2 is then solved for $v(y_j, x_i)$ and then further approximated in the following step. As a result, a single iteration step leads to:

$$v^{k+1}(y_j, x_i) = \frac{1}{4}\left(v^k(y_j, x_{i+1}) + v^k(y_j, x_{i-1}) + v^k(y_{j+1}, x_i) + v^k(y_{j-1}, x_i)\right) + \\ + \frac{(\Delta h)^2}{4} f_{j,i}. \tag{5.3}$$

However, to reach a reasonable approximation when simulating a usual detector size, this method requires several iteration steps which translate into an excessive CPU consumption and calculation time. To get a faster calculation, the number of simulation steps is reduced by implementing a multigrid structure, which allows to start the potential calculation on a coarser grid with a certain Δh_c and then to refine it to a grid with $\Delta h_f = \Delta h_c/2$ at each iteration step.
On the finest grid, with user defined detector size "`YMAX`" (for the thickness), "`XMAX`" (for the width), "`pitch` " and "`width` " (for strip pitch and width) the `Potentials` class creates a two-dimensional array and adjusts the `XMAX` value to place a strip exactly in the middle of the sensor.
Afterwards, the program resets the electrodes to the user selected value and sets the potentials. Drift potential is calculated by setting n-type readout electrodes to bias voltage and backplane to 0 for a n-on-p sensor or p-type strips to 0 and backplane to bias voltage for a p-on-n sensor. In order not to change the electrodes and backplane positions when iterating, the program sets another array called "fix ", while the boundary conditions for potentials and "`fix` " arrays are set by the method `SetBoundaryConditions()`.

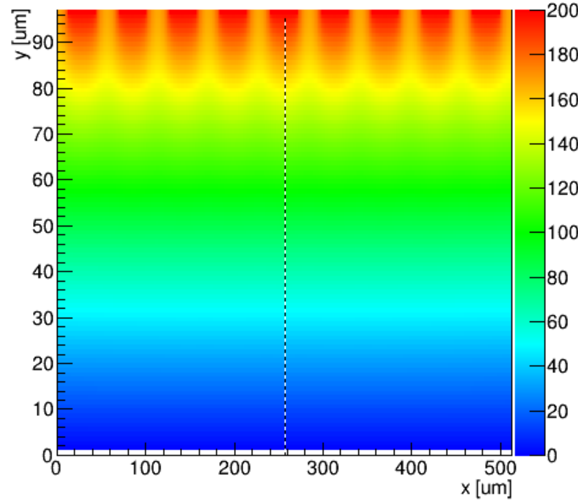

Figure 5.1: Drift potential for microstrip n-on-p geometry.

The total number of grids depends on detector dimensions: the function

`Restriktor()` maps the potential array to the coarsest grid, which contains (`XMAX`/2 + 1)×(`YMAX`/2 + 1) entries, and the calculation starts from this grid. The method `Gaussseidl(void*)` calculates the potentials in an infinite loop which breaks when $\sum_{i,j} |\, \mathrm{pot}_{i,j}^{old}$ - $\mathrm{pot}_{i,j}^{new}| < 0.001$ for 0<i<`XMAX` and 0<j<`YMAX`. As the calculation on the coarsest grid finishes, it is transferred to a finer one with the function `Prolongation()`: mutual points are copied from the old grid to the new grid which sizes (2`XMAX`$_{old}$ -1)×(2`YMAX`$_{old}$-1). Then, the function `Gaussseidl(void*)` is called again and calculates the potentials on this grid. This procedure is repeated until the finest grid is reached.

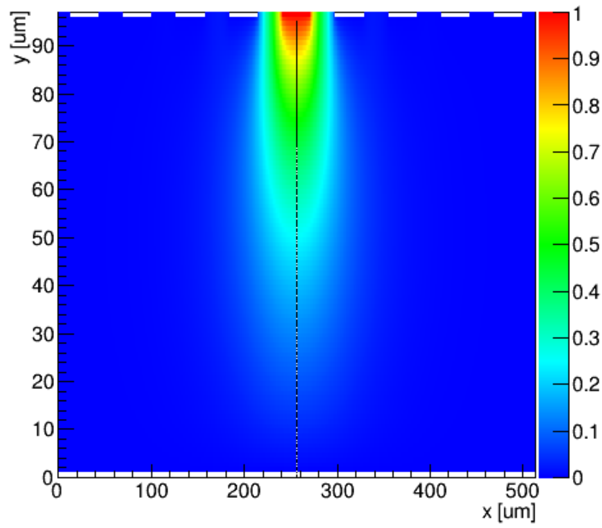

Figure 5.2: Weighting potential for microstrip n-on-p geometry.

5.1.2 Field calculation

For every point of the grid, the method `CalculateFields(Potentials &p, Field** df, Field** wf)` calculates numerically the drift and the weighting fields defined as $\vec{E_d} = -\nabla V_d$ and $\vec{E_w} = -\nabla V_w$ along x and y coordinates:

$$E_x = -\frac{V_{j,i} - V_{j,i-1}}{d},$$

$$E_y = -\frac{V_{j,i} - V_{j-1,i}}{d},$$

where d is the sensor thickness. If the option to have an additional magnetic field is on (Fig. 5.3 [35]), the drift field is rotated by a Lorentz angle θ with the rotation matrix

$$R_\theta = \begin{pmatrix} \cos\theta & -\sin\theta \\ \sin\theta & \cos\theta \end{pmatrix}$$

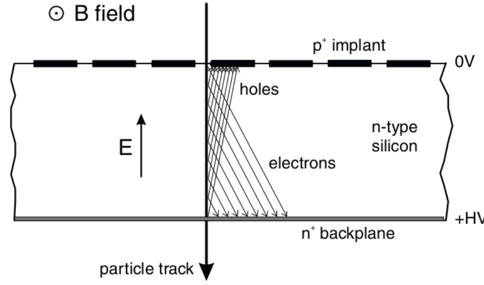

Figure 5.3: Since the magnetic field deflects electrons and holes trajectories, the Lorentz shift produces an offset between the particle track and the measured position [35].

5.1.3 Current calculation

As described in Sec. 2.1.1, electrons and holes produced by an ionizing particle drift under the effect of the electric field E_d with a certain drift velocity (Eq. 1.10) $\vec{v} = \mu\vec{E_d}$, which only depends on the applied electric field and on the carrier mobility (which is estimated as 1350 cm^2/V·s for electrons and 450 cm^2/V·s for holes).
Moreover, thermal diffusion adds up to drift motion (Sec. 1.2.4): carrier motion is then given by the superposition of drift and random diffusion motion:

$$\vec{v} = \vec{v}_{drift} + \vec{v}_{diffusion}. \tag{5.4}$$

However, the validity of Eq. 1.10 is restricted to small electric fields, while for higher electric fields the values of the drift velocities are better described by the empirical relations

$$\begin{aligned} v_e &= \frac{\mu_e E_d}{\sqrt{1+\left(\frac{\mu_e E_d}{v_{e,sat}}\right)}}, \\ v_h &= \frac{\mu_h E_d}{1+\frac{\mu_h E_d}{v_{h,sat}}}, \end{aligned} \tag{5.5}$$

where $v_{e,sat}$ and $v_{h,sat}$ are the electron and hole drift velocity saturation values.
The induced current on a single electrode is then given by Ramo's theorem (Eq. 2.2) and the total induced current is obtained by summing up all electrode contributions (Eq. 2.4). Current calculation is performed by the function `CalculateCurrents(Potentials &,Field**,Field**,Carriers*, void*)`.
As the drift and weighting potential calculation finishes, it is possible to start current calculation from the graphical interface. The program simulates the electron-hole production by an ionizing particle by distributing charge carriers along an imaginary trajectory. The point where the particle hits the detector and the angle formed with the vertical are selectable from the graphical interface.
It is possible to choose from a MIP or a alpha particle with uniform or non uniform charge distribution. The simulation of a MIP is done by the class `CreateCharges(Potentials &,Carriers*,int,void*)`, while alphas are simulated via `CreateChargesAlphaTop(Potentials &,Carriers *,int, void*)`

and `CreateChargesAlphaBottom(Potentials &,Carriers*,int,void*)`. Two flags allow to switch between uniform and non-uniform charge deposition (`UniformQFlag`) and to fix the total charge value (`ConstQFlag`).

Simulation of Minimum Ionizing Particles

The program offers several different implementations of MIP signals (Fig. 5.6).

1. **MIP with uniform charge deposition:** this option represents the idealized case of uniform constant energy deposition, set to 75 e-h pairs per micron. In this case, `UniformQFlag` and `ConstQFlag` are both set to true.

2. **MIP with non-uniform charge deposition:** simulates a MIP with the same total charge of the ideal MIP but accounts for non uniformity in charge distribution. `UniformQFlag` is set to false while `ConstQFlag` is set to true. The non-uniform charge deposition case introduces variability in the charge distribution along the detector thickness. A GEANT 4 simulation of energy loss in 5 µm silicon is used to build a library of energy deposition (Fig. 5.4), from which a random dE/dy value is extracted. With this library, it is possible to predict energy deposition in any thickness.
The energy deposited in 5 µm is then divided by 5 and by the energy needed to produce a pair to get the number of created e-h pairs per µm.

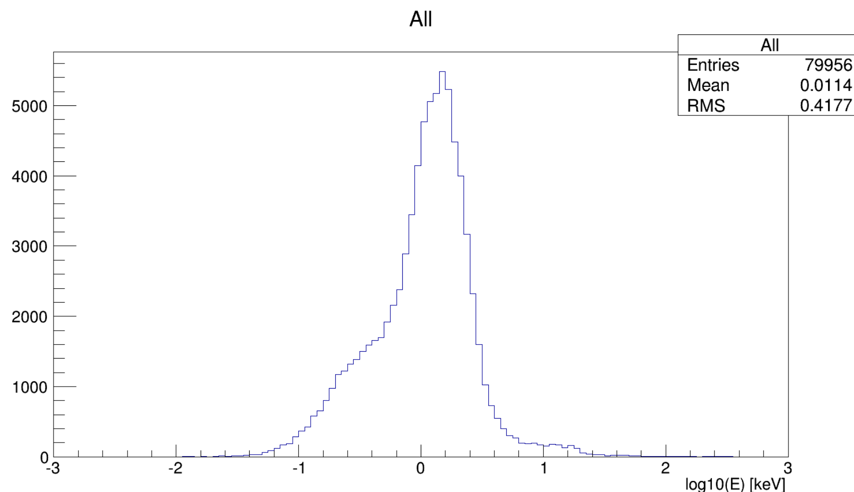

Figure 5.4: Histogram containing charge deposition values per 5 microns.

3. **MIP with Landau distributed charge:** both non uniformity in charge distribution and amplitude variability are considered. Both `UniformQFlag` and `ConstQFlag` are set to false.

4. **MIP with uniform charge distribution and user defined charge:** allows the user to simulate a uniform charge distribution with user defined charge deposition per micron. This case is the more realistic case because introduces also variability in the total MIP charge, achieved by extracting a random value from a Landau distribution.

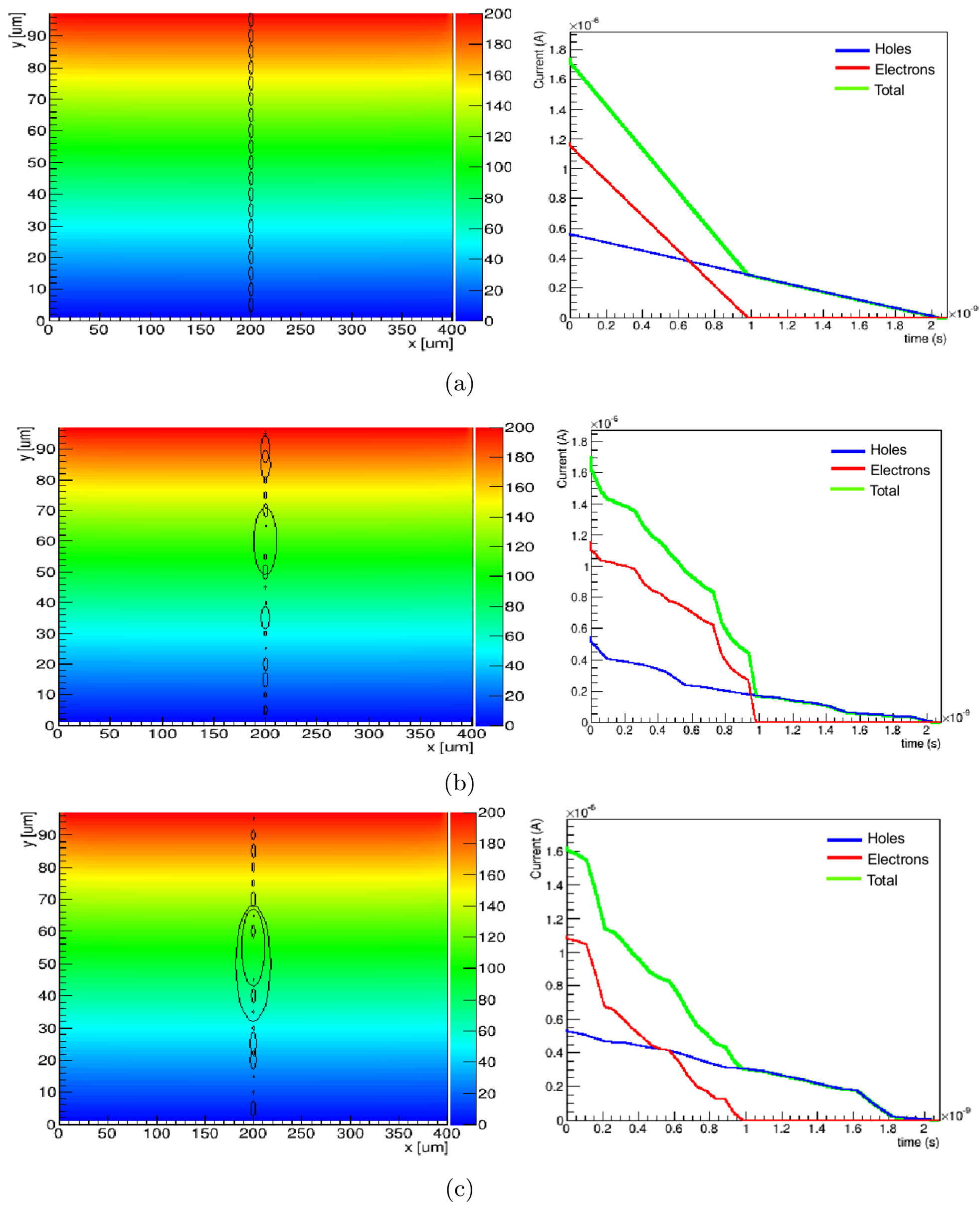

(a)

(b)

(c)

Figure 5.5: Charge distribution (left) and current vs time (right) in a n-on-p pad sensor of 100 µm thickness and 400 µm width for V_b= 200 V, V_{depl}= 50 V for the case a) MIP with uniform charge distribution, b) MIP with non uniform charge distribution, c) MIP with Landau-distributed charge. In the current graph, the less smooth lines and the bumps of the cases b) and c) indicate non uniformity in charge distribution.

Simulation of alpha particles

1. **alpha particle from top:** simulates an alpha particle entering the sensor from the top

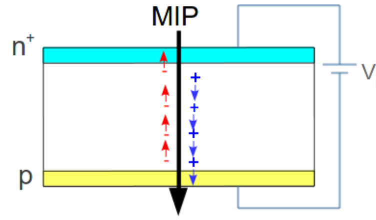

Figure 5.6: Schematic view for the drift of e-h pairs produced by a MIP.

2. **alpha particle from bottom:** simulates alpha particles entering the sensor from the bottom.

It is useful to simulate alpha particles because they are a good diagnostic instrument: alphas deliver a very localized charge deposition in silicon and produce pairs only in a superficial layer [45]. The signal generated by the drift of this localized charge depends strongly upon the electric field inside the sensor. This technique is called *Transient Charge Technique* (TCT).
The range of alpha particles in silicon increases with the particle energy: for a 5 MeV particle the nominal range is about 32 µm, but the effective range is reduced to about a third, due to additional energy losses in air along the way from the source to the sensor. The program allows the user to set the alpha particle range. As can be seen from Fig. 5.7 and Fig. 5.8, alpha particles from the top produce pairs only in the upper part of the sensor: electrons are immediately collected while holes drift to the bottom of the detector, where the electric field is lower so they slow down (hole current is decreasing, Fig. 5.7.a). Alpha particles from the bottom ionize in the lower part of the sensor: holes are collected first, electrons drift to the n^+ electrode where the electric field is higher, causing increase of the drift velocity and of the current (Fig. 5.8.b).
The shape of the current graph varies on whether the detector is collecting

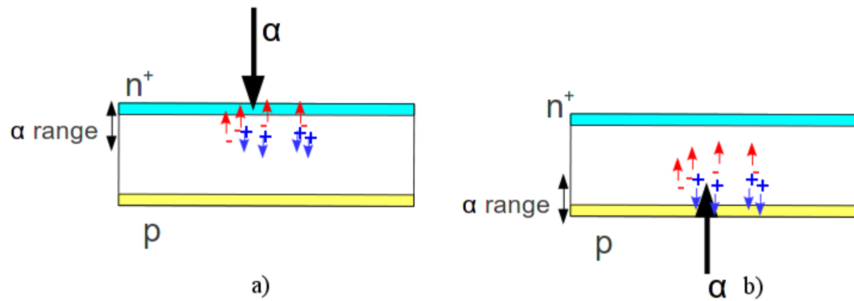

Figure 5.7: Schematic view of charge deposition by a) alpha particle from top and b) from bottom and carriers drift.

electrons or holes. Basically, a p-on-n sensor collecting holes produce a current distribution which is symmetric with respect to a n-on-p sensor collecting electrons. Since the most common doping configuration is p bulk set to negative bias voltage and n readout electrode set to ground, the simulations presented in this chapter are intended for a n-on-p sensor.

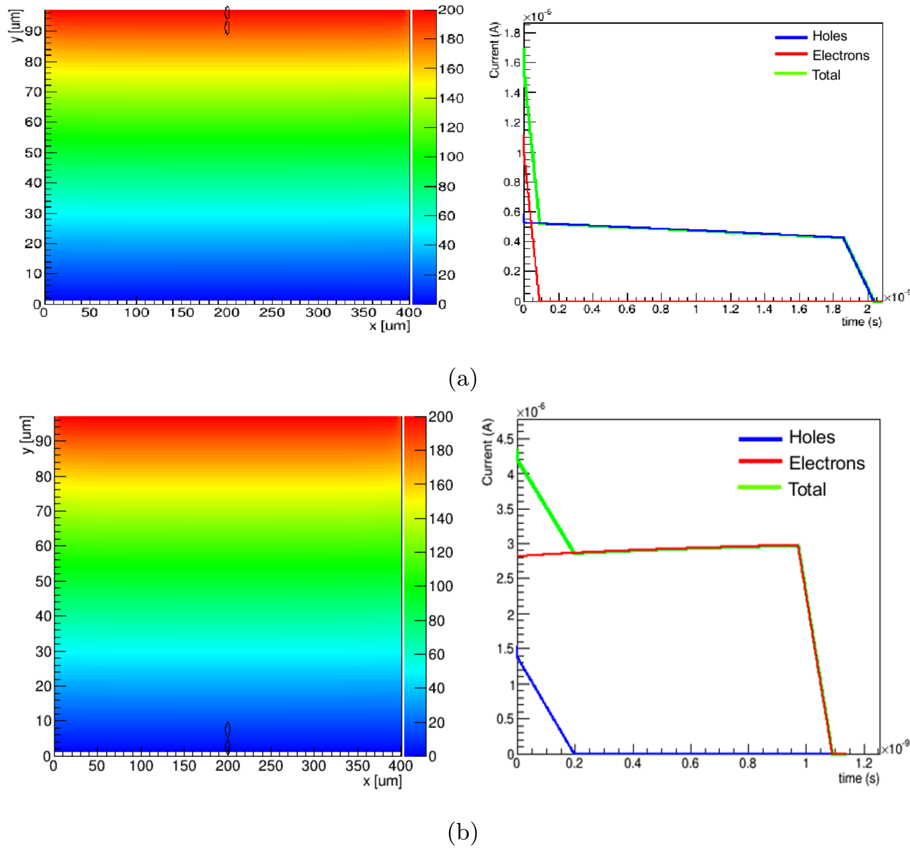

(a)

(b)

Figure 5.8: Charge distribution (left) and current vs time (right) in a pad sensor of 100 µm thickness and 400 µm width with V_b= 200 V, V_{depl}= 50 V for the case a) alpha from top, b) alpha from bottom.

5.1.4 Gain implementation

This section describes how the gain layer present in UFSD is implemented in the *Weightfield 2.0* program.
Theory of impact ionization model (Sec. 3.2.2) predicts a given dependency of the charge multiplication on the electric field. Since the actual behavior of gain in recently produced Ultra-Fast diodes is not well known, we developed a model able to simulate such sensors and to make affordable predictions. Gain layer thickness is fixed to the constant value of 4 µm, starting at 3 µm under the sensor surface.
Since charge multiplication has comes into play at electric field values of about 250-300 kV/cm and higher fields would lead to sensor breakdown, the electric field is tuned to reach these values in correspondence of the gain layer.

Drift potential with gain

The gain layer is turned on if the entry *Gain scale factor* contains a number larger than 1. Without knowing the actual dopant concentration of the p^+ gain

implant, the gain layer is added "by hand" with the method `CallCalculatePotentials()` of the class `WFGUI`.
As said in Sec. 2.1.2, the drift potential V_d is given by the so called *overbias*, i.e. the difference between bias and depletion voltage $V_{bias} - V_{depl}$, and the drift field $(V_{bias} - V_{depl})/d$ is responsible of charge carrier motion inside the sensor. Typically, drift field is not sufficient to produce charge multiplication, since the strength required to reach the saturation of drift velocity is about one order of magnitude lower than that required to start the avalanche process.
Drift potential is adjusted in order to reach an adequate field strength for charge multiplication within just 3 microns along y, forming the *gain layer*: it is set to have a rapid increase along the y coordinate which can be parametrized by

$$V_{d,gain} = V_d + G_{dist}^{2.1}, \tag{5.6}$$

where G_{dist} is an increment factor which gains 2 units at each step.
The voltage $V_{d,gain}$ used for multiplication is then subtracted to the drift potential (Fig. 5.9)

$$V_{d,bulk} = V_{bias} - V_{depl} - V_{d,gain}, \tag{5.7}$$

and $V_{d,bulk}$ is the fraction of the bias voltage which effectively determines the drift of the charge carriers.

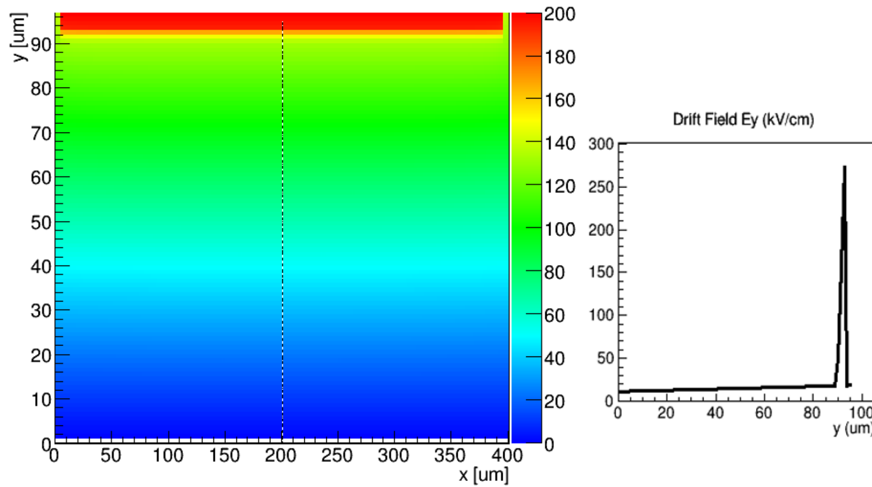

Figure 5.9: Drift potential (left) and field (right) with gain for V_b= 200 V, V_{depl}= 50 V, g_s= 2. The drift field reaches the required strength (250-300 V/cm) within the last microns.

Carrier drift with gain

From the theory of impact ionization model, the gain g (defined as N/N_0) has an exponential dependency on the α multiplication coefficient and the distance traveled along the electric field d

$$g \propto e^{\alpha d} \tag{5.8}$$

where the α coefficient depends on the local electric field giving rise to the multiplication, E_{local}, and on a constant $\alpha_c = 1.8 \cdot 10^{-35}$

$$\alpha = \alpha_c (E_{local})^7. \tag{5.9}$$

The electric field in the gain layer is of the order of $E_{local} \sim 10^5$ kV/cm, the dependence of α on the electric field is very weak and therefore α is about a constant.
Laboratory measurements confirm (Sec. 6.3) that LGAD have small gain. For low gain, the exponential dependence of α on the electric field can be approximated by a linear dependence

$$\alpha \sim \alpha_c E_{local} d, \tag{5.10}$$

and the dependence of the gain g on α can be written as the number of pairs generated N_{gain} at each step plus an offset $g_o = \sqrt{g_s} \cdot \alpha$

$$g = \sqrt{g_s} \cdot \alpha + N_{gain}, \tag{5.11}$$

being g_s the "gain scale factor" selectable by the user from the GUI. The observed behavior indicates that the gain has more a square-root rather than a linear dependence with the gain scale factor.
The gain of UFSD introduces two more components in the current: *gain electrons* and *gain holes*, which are the charge carriers produced by impact ionization (Sec. 3.2) inside the gain layer. These new contributions to the total current obviously lead to an increase in the total collected charge, resulting in a larger signal (Fig. 5.10, 5.11).

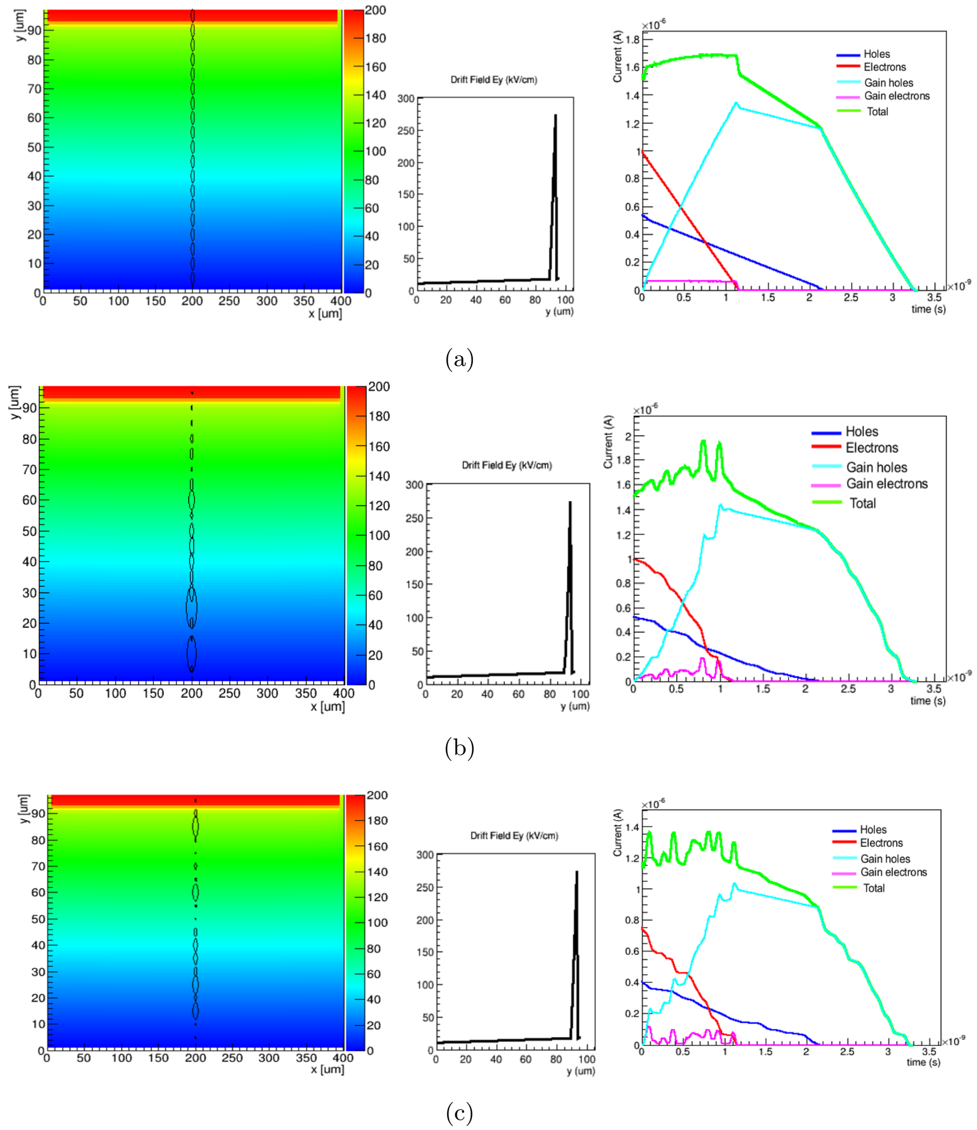

Figure 5.10: Charge distribution and drift potential (left), electric field (middle) and current vs time (right) for a sensor of 100 µm thickness and 400 µm width with V_b= 200 V, V_{depl}= 50 V, and gain scale factor g_s= 2 for the case a) MIP with uniform charge distribution, b) MIP with non uniform charge distribution, c) MIP with Landau distributed charge.

5.1.5 Graphical interface

Weightfield 2.0 graphical interface (Fig. 5.12) has been developed starting from the existing one in *Weightfield*. The left side contains four panels with the canvases showing potential, current and shaper output graphs. The right side of the GUI is divided in various panels where the user can select the input conditions for the simulation.

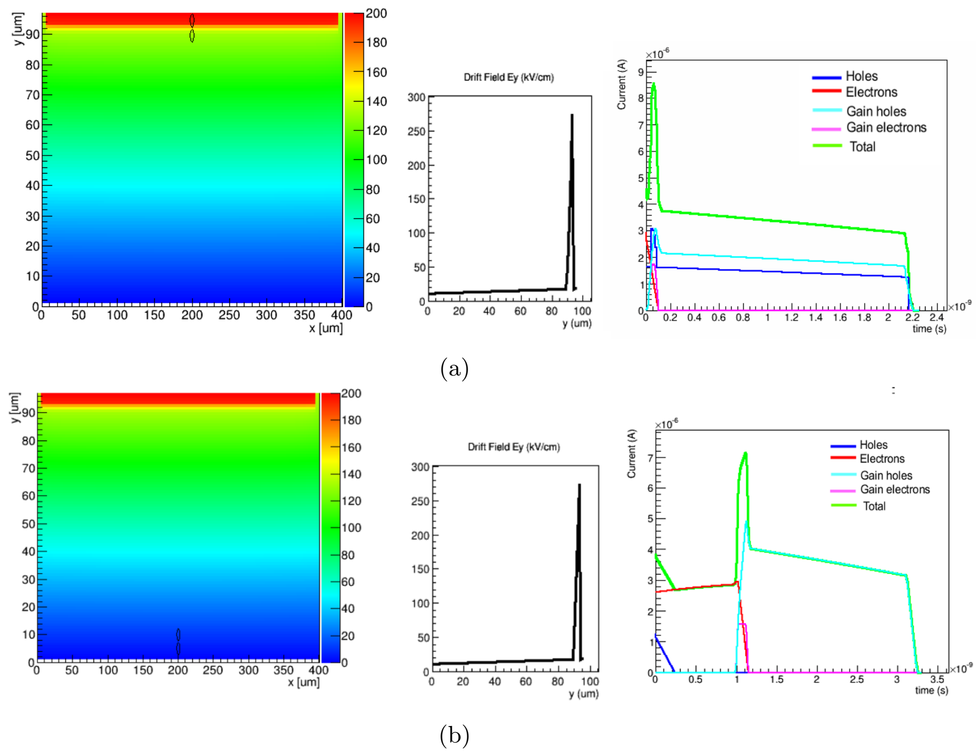

Figure 5.11: Same as Fig. 5.10 for a) alpha from top and b) alpha from bottom.

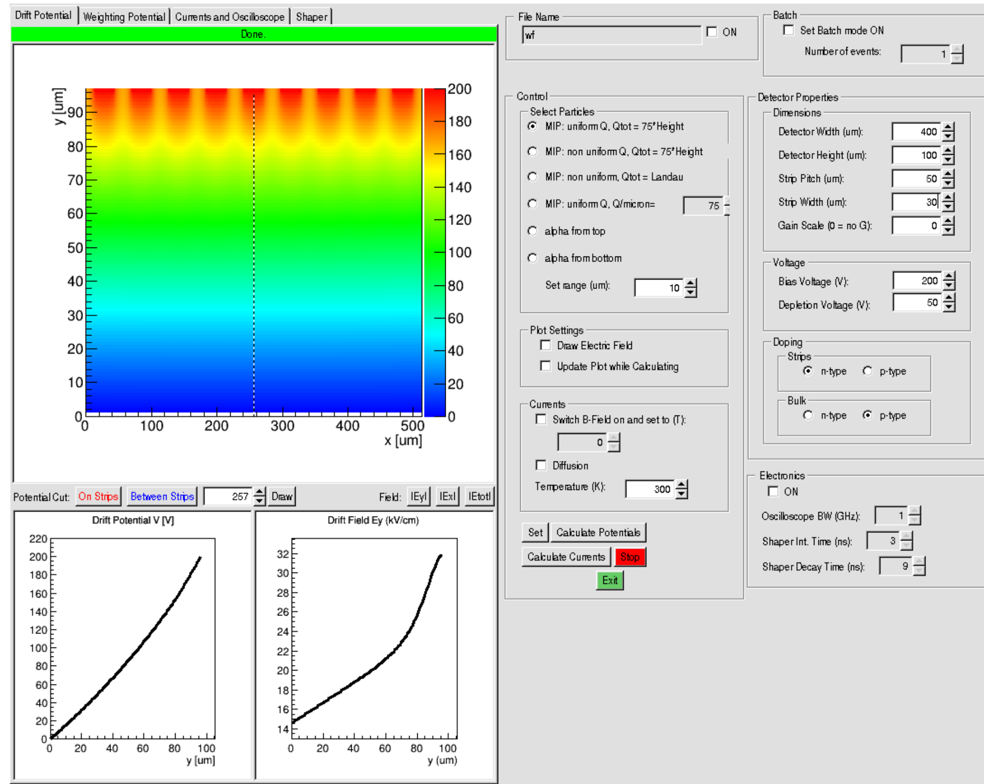

Figure 5.12: Weightfield 2.0 graphical interface.

Control panel

The *Control Panel* is divided in three boxes: *Select Particles*, *Plot Settings* and *Currents*. In the *Select Particles* box it is possible to select the type of incident particle choosing between MIP and alpha particle.
The *Currents* box allows to set a temperature value in K and to add the effect of magnetic field, with user selectable value in T, and of a thermal diffusion.
The *Calculate Potentials* button starts potential calculation and draws the drift and weighting potentials into the canvases on the left side of the GUI. In addition, the *Plot Settings* box allows to draw on the potential canvas the field lines.
The *Calculate Currents* button starts currents calculation and plots the current vs time graph in the current tab. In addition, it gives an overview of the initial charge distribution inside the sensor by drawing on the drift potential canvas ellipses with charge proportional radius.
The *Stop* button interrupts current calculation by exiting the loop over time, while *Exit* button closes the program.

Detector properties panel

The *Detector Properties* panel consists of three boxes:

- *Dimensions*: this box allows the user to choose the detector geometry by selecting the detector width, thickness, strip pitch and width in microns

and the gain scale factor described in Sec. 5.1.4;

- *Voltage*: to select depletion and bias voltages;
- *Doping*: to select the doping of bulk and electrodes.

Batch mode panel

The *Batch Mode* panel creates a loop of a selectable number of events when the corresponding button is on.

Electronics panel

The *Electronics* panel allows to simulate the voltage outputs of an oscilloscope and a shaper. The program plots the oscilloscope output on the current vs time plot in the *Currents and Oscilloscope* tab (Fig. 5.13) and the shaper output into its dedicated *Shaper* tab. The oscilloscope bandwidth is selectable, while two remaining entries allow to set integration and fall time of the shaper. The oscilloscope and the shaper are implemented within the function `CalculateCurrents(Potentials &, Field**, Field**, Carriers*, void*)`. The oscilloscope output voltage is evaluated as

$$V_{out,osc} = I_{tot} R_{in} \left(1 - e^{-\frac{t}{\tau}}\right), \tag{5.12}$$

where $R_{in} = 50\ \Omega$ is the oscilloscope internal resistance and $1/\tau$ is the oscilloscope sampling frequency.
The output of a shaper with rise time t_r and fall time t_f is obtained with by the function

$$V_{out,shaper} = V_{in} \left(1 - e^{-\frac{t}{t_r}}\right) e^{-\frac{t}{t_f}}. \tag{5.13}$$

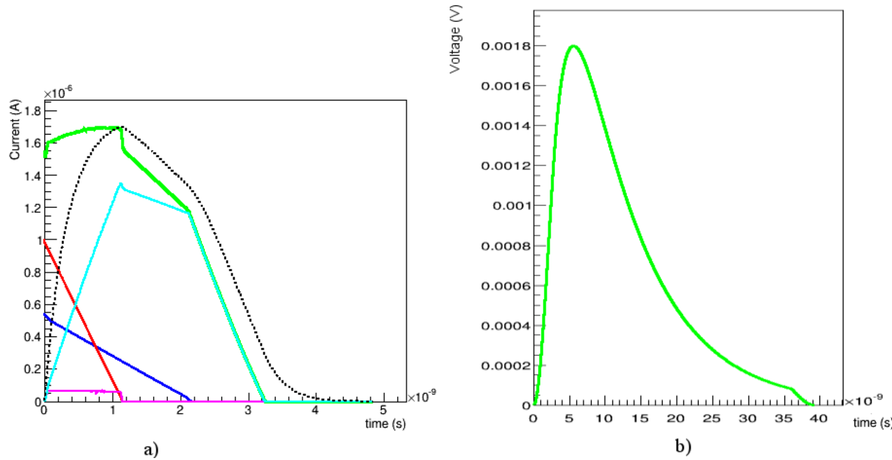

Figure 5.13: a) Current vs time plot for a MIP with non uniform charge distribution in a detector with gain: the black dashed line is the oscilloscope output of the same signal.

Drift and weighting potential tabs

The drift potential tab contains a canvas showing a 2-dimensional view of the drift potential inside the sensor. The x coordinate corresponds to the sensor width and the y coordinate to the thickness. It is possible to plot a 1-dimensional graph of the drift potential and drift field (along y) by fixing a value for x from the entry *Potential Cut*. The dashed line indicates the coordinate at which the potential cut is set. The *On Strips* button plots the drift field on the electrodes, by setting the horizontal cut value to the middle of the central electrode, while the *Between Strips* button sets the cut coordinate in middle between two neighboring electrodes.
The weighting potential tab is similar to the previous, one showing the weighting potential and field instead of the drift ones.

Currents tab

Currents tab features:

- the current canvas described in Sec. 5.1.3
- the time bar indicating the charge collecting time
- an entry to select the x coordinate at which the particle hits the detector
- an entry to select the angle (in degrees) formed by the particle trajectory with the vertical
- the *Charge Collection* table showing the individual contribution of each component to the total current
- the *Lorentz Drift* table showing the angle (in degrees) formed by electrons and holes when the magnetic field is on.

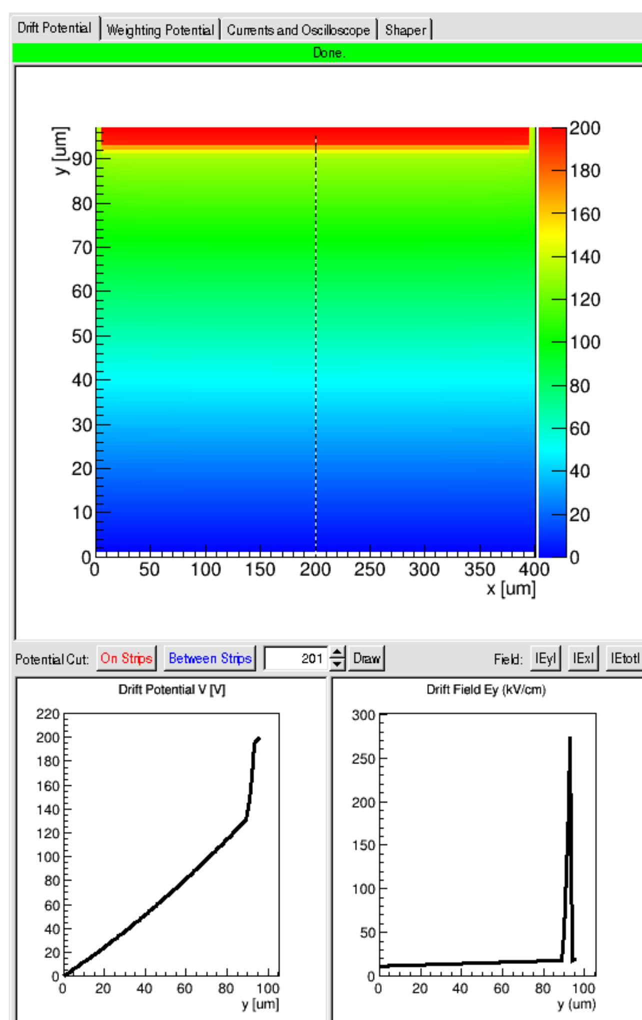

Figure 5.14: Drift potential tab features a canvas with a 2-dimensional view of the drift potential in the sensor. The lower part of the tab contains the graphs with the 1-dimensional view of the drift potential and of the drift field along the cut line.

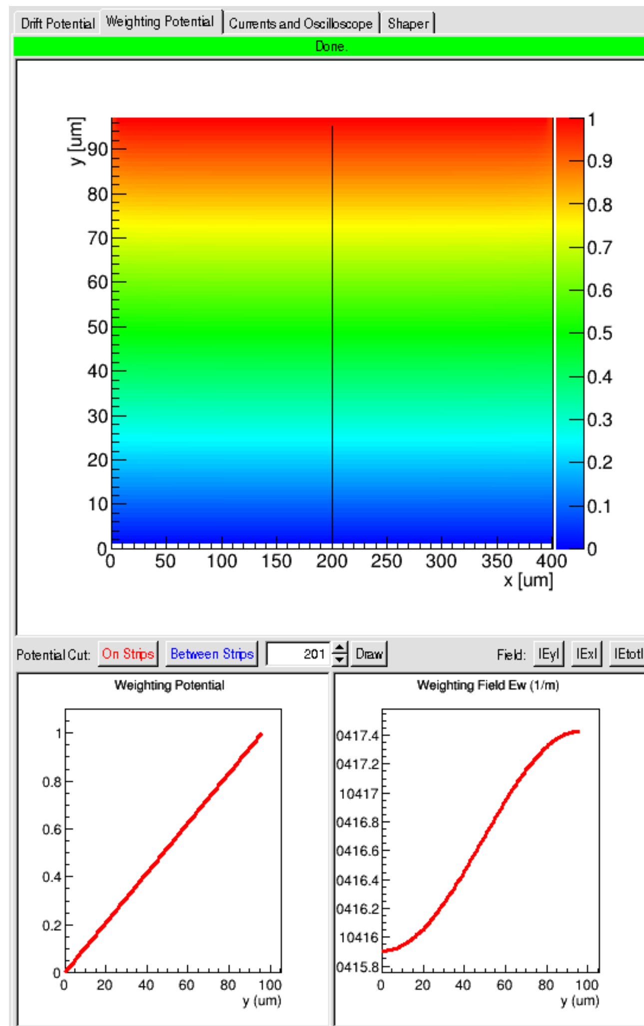

Figure 5.15: Weighting potential tab: the canvas in the upper part of the tab shows the weighting potential inside the sensor in 2 dimensions. The lower part features two graphs for weighting potential and weighting field in 1 dimension along the cut line.

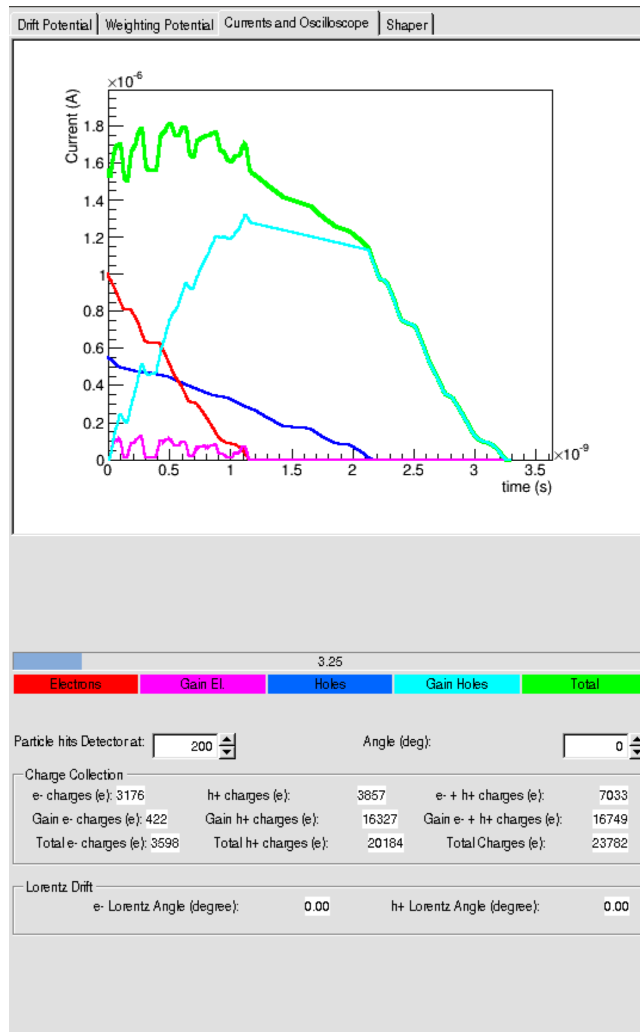

Figure 5.16: *Currents* tab contains the currents canvas, the time bar indicating the charge collecting time, two number entries to select the x hit coordinate of the particle and the angle formed by the particle trajectory with the vertical, the individual contributions to the total current and the Lorentz angle formed by electrons in presence of a magnetic field.

Chapter 6

Measurements and Results

To understand the behavior of the gain layer in Ultra-Fast detectors, a laboratory setup has been built at the Physics Department in Turin to test the devices. Laser measurements have been done on a CNM UFSD and compared with simulation.

6.1 Laser test

Laser penetration depth in silicon depends on the photon wavelength, and then on its energy (Fig. 6.1). The intensity of the radiation varies with the depth x and the *absorption coefficient* μ (or its reciprocal $\lambda = 1/\mu$, called *absorption length*), according to the *Lambert-Beer law*

$$I(x) = I_0 e^{-\mu x}, \tag{6.1}$$

where I_0 is the initial intensity. Fig. 6.2 shows the absorption coefficient dependence on the photon wavelength for different materials.
To cross the whole sensor bulk (as MIPs do), the photon wavelength has to be chosen in order to get a penetration depth a few times larger than the sensor thickness: for example, a wavelength of more than 1000 nm has a penetration depth of the order of the millimeter, higher than the average sensor thickness ($\sim$ 100 - 300 µm).
The laser device considered for the test setup is a picosecond laser providing both infrared and blue visible photons with wavelengths of 1060 nm and 405 nm, respectively. The two different wavelengths are provided by two laser heads, each connected to an optic fiber. In addition, since the charge deposition time for a MIP is of the order of the picosecond, it is useful to employ a laser with a pulse repetition rate comparable to this value.
The 1060 nm wavelength corresponds to an energy of about 1.2 eV, which is about the energy of the silicon band gap and hence the laser beam has an effect comparable to a MIP, producing just one electron-hole pair per photon, distributed along the whole sensor thickness.
Instead, the signal generated by a laser beam with 405 nm wavelength is comparable to the one produced by an alpha particle, since it does not penetrate the whole sensor but it stops within the first 10 µm. The range of alpha particles in silicon depends on their energy, but for a moderate-energy particle (under 5

MeV) the range is about a few tens of microns. It is reasonable to estimate a range of about 10 µm, therefore alpha particles are useful to inspect the gain layer of Ultra-Fast sensors, which is placed within the first 5 µm under the readout electrode. (Fig. 6.3).

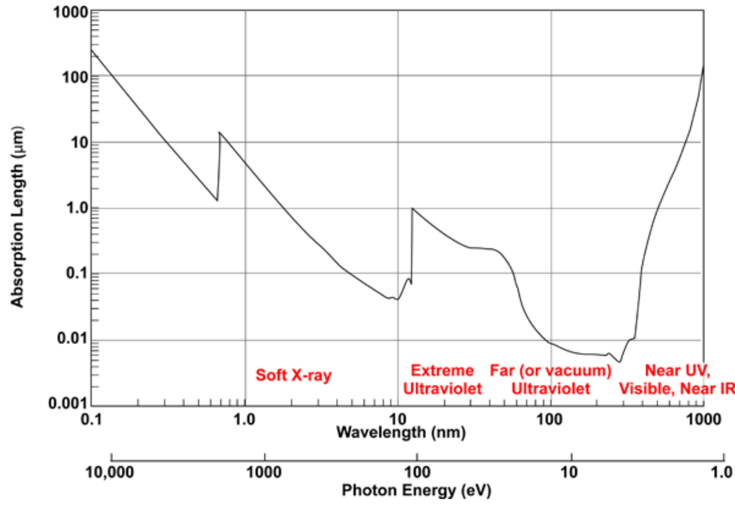

Figure 6.1: Absorption length in silicon as a function of the wavelength and the energy of the incident radiation.

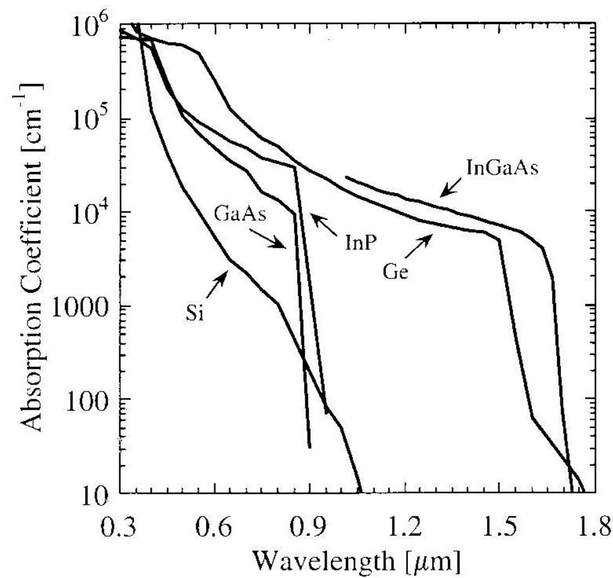

Figure 6.2: Absorption coefficient as a function of the wavelength for different materials.

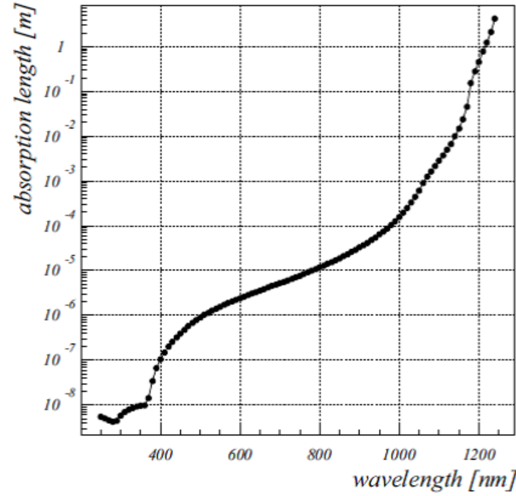

Figure 6.3: Closeup of Fig. 6.1 for wavelengths between 400 and 1200 nm.

6.2 The LGAD under test

The detector used for our measurements is a Low Gain Avalanche Detector (LGAD) produced by CNM [46].
A top view of the 5 mm × 5 mm sensor (from run 6474) is shown in Fig. 6.4. The inner part consists of a passivated optical window, surrounded by a metalized overlap of 120 µm width and a collector ring, while the outer part contains p-spray and a channel stopper. The transverse section of the inner part of the

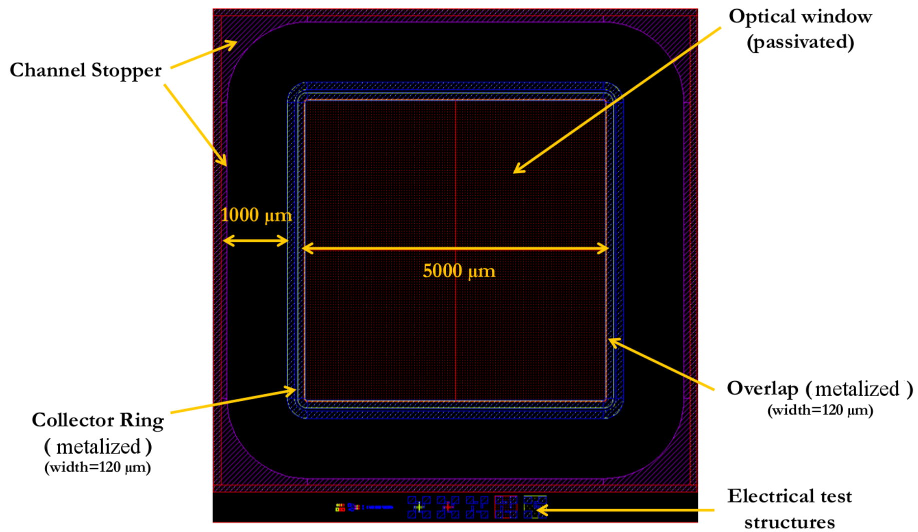

Figure 6.4: Top view of the 5 mm × 5 mm LGAD by CNM.

sensor is depicted in Fig. 6.5. From bottom to top:

- a 1 µm thick metal layer which is partially removed in the latest produced sensors (gray line),
- a 1 µm thick p^{++} layer for contact (blue line, doping concentration is shown in Fig. 6.8c),
- a low-doped p bulk of 300 µm thickness (yellow),
- the p-type multiplication layer (gain layer) of 5 µm thickness, doped with boron (light blue),
- the highly doped n^{++} electrode ($\sim 10^{18}$ cm^{-3}). This layer is conductive and deserves for readout: its thickness is 1 µm while "cavities" are 7 µm (red),
- a 700 nm thick SiO_2 layer for AC coupling (brown),
- the metalization (gray), which is 1.5 µm thick and is grounded,
- a SiO_2 - Si_3N_4 double oxide passivation of 400 nm thickness (green).

Fig. 6.6a shows the doping concentration along the cut line 1: the red line represents the phosphorus concentration, which determines the n^{++} highly doped readout electrode, while the blue line is the boron concentration (p doping) and the dashed line is the intrinsic concentration. The small peak at low depth in the boron concentration is a residual of the initial shot for boron implantation; the p^+ zone representing the gain stands where the boron concentration equals the phosphorus one.
Fig. 6.6b shows the doping concentration along the cut line 2: phosphorus concentration is very high at the top ($\sim 2 \cdot 10^{19}$) and decreases with depth until it merges with the bulk.

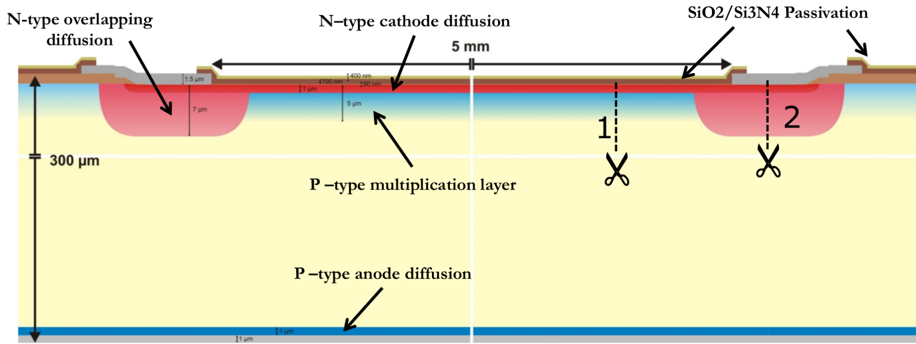

Figure 6.5: Transverse section of the CNM LGAD, inner zone.

The outer part of the LGAD has a vertical section as in Fig. 6.7, composed as:

- p-spray to isolate and avoid free electrons within the bulk (light blue). Boron concentration here is $\sim 10^{14}$ (Fig. 6.8a),

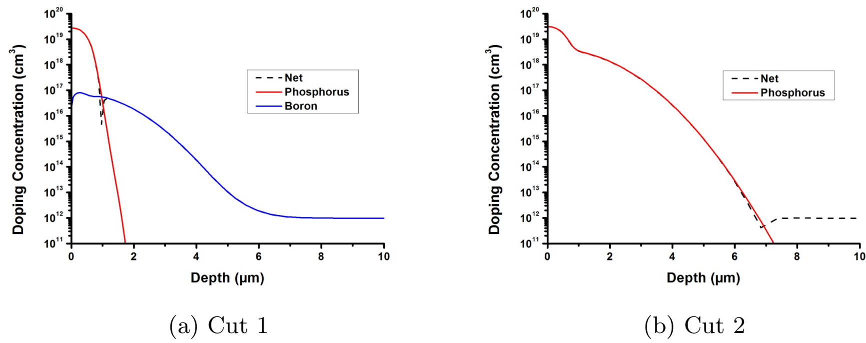

(a) Cut 1

(b) Cut 2

Figure 6.6: Doping concentration vs depth along cut line a) 1, b) 2.

- p-type channel stopper deserving as insulator at the edge of the sensor, highly doped (Fig. 6.8b),
- field oxide, 1.3 µm thick (light brown).

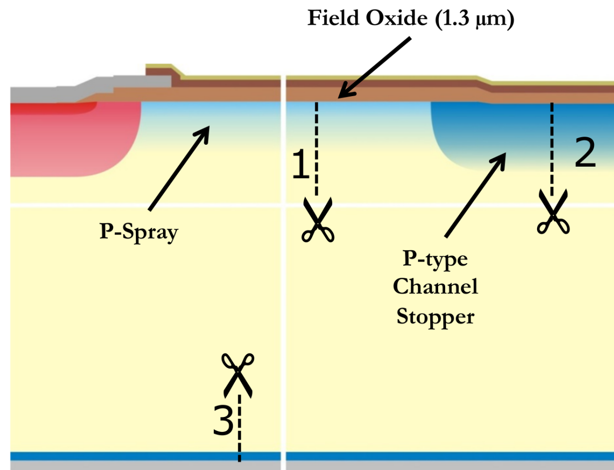

Figure 6.7: Transverse section of the CNM LGAD, outer zone.

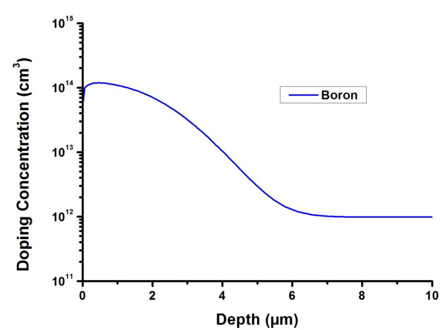

(a) Cut 1

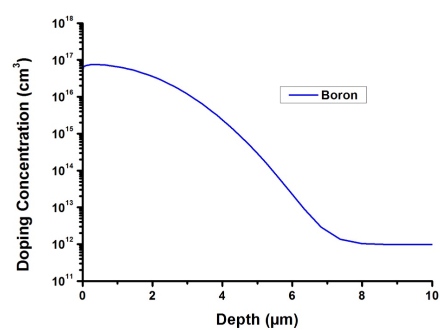

(b) Cut 2

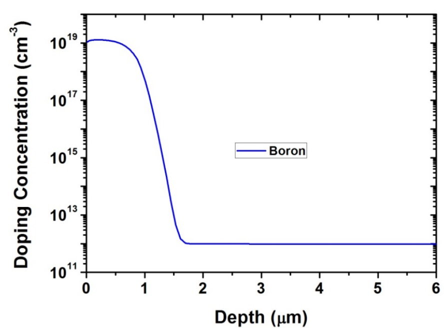

(c) Cut 3

Figure 6.8: Doping concentration vs depth along cut line a) 1, b) 2, c) 3.

6.3 Laboratory measurements

6.3.1 Laboratory setup

The laboratory setup (Fig. 6.9) consists of:

1. Picosecond laser (PiLas) by Advanced Laser Diode Systems with controller EIG2000DX, equipped with two heads of different wavelength:
   - 1060 nm, simulating a MIP
   - 405 nm, simulating an alpha particle
2. Oscilloscope (LeCroy WaveRunner 625Zi, sampling frequency 2.5 GHz)
3. Power supply (Keithley 2410)
4. Bias Tee (Mini-Circuits ZFBT-42RG+)
5. Sensor: CNM High resistivity FZ diode, 5mm × 5 mm, 300 µm thickness, contained into a metal box

As shown in Fig. 6.10, the optic fiber is positioned directly over the sensor, in correspondence of a hole at the top of the metal box containing the sensor, which allows the laser beam to enter. Laser pulses are sent with the controller through the fiber for both wavelengths: 1060 nm ("MIP-like" signal) and 405 nm ("alpha-like signal"). The sensor output signal is sent directly to the oscilloscope and then measured. The procedure is repeated for different bias voltages, from 200 V to 600 V in steps of 100 V. The oscilloscope output for the MIP case is shown in Fig. 6.11a, while alpha particle from the top and from the bottom are shown in Fig. 6.11b and Fig. 6.11c, respectively.

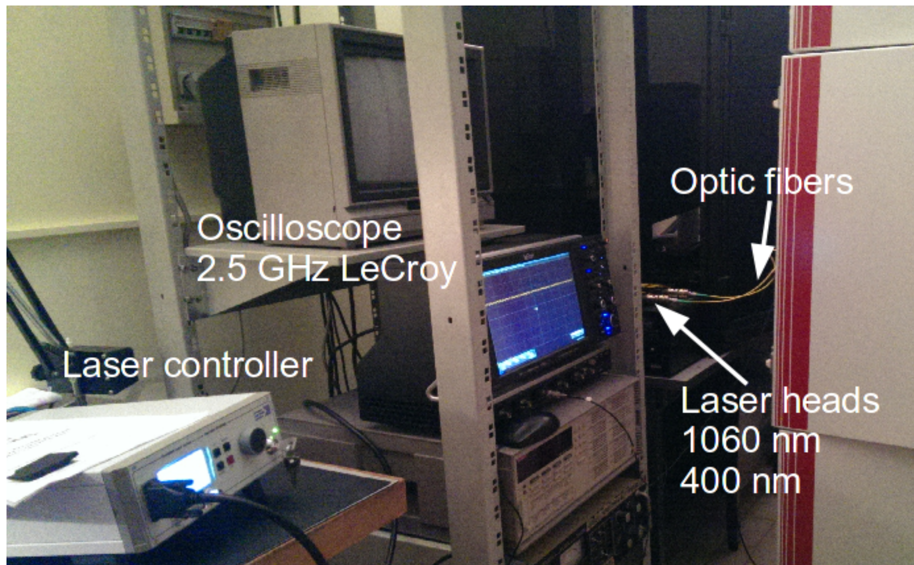

Figure 6.9: Laboratory setup.

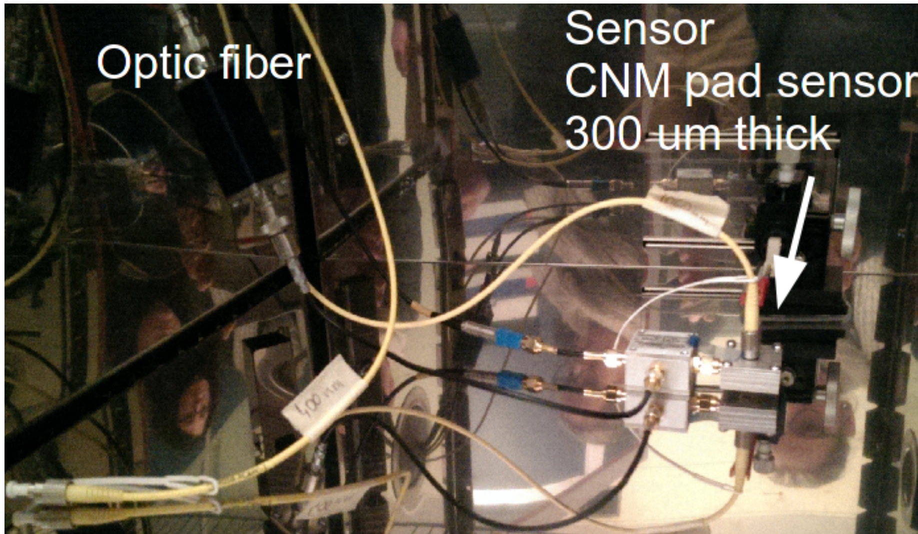

Figure 6.10: Optic fiber, bias tee and sensor.

6.3.2 Laser measurements and simulation

Our goal is to test the ability of the *Weightfield 2.0* program to predict the effect of charge multiplication and then to simulate a real sensor with gain. For this purpose, the oscilloscope outputs for the different bias voltages are compared with the results of a simulation performed for the same sensor geometry and bias voltage.

Simulation parameters

To simulate a pad geometry, one can set in the *Dimensions* panel of the program a strip width close to the pitch value, for example *pitch* = 400 µm and *width* = 390 µm. In this case, the drift field will be uniform, as shown in Figs. 5.5 and 5.8. It is not necessary to set the whole width of the sensor (5 mm in our case) when evaluating the signal shape, since it is influenced by the sensor thickness only. Moreover, since charge multiplication increases further the time needed for the simulation, reducing the width parameter allows to keep this time relatively low.
The geometrical parameters are then:

- *Detector Width* = 400 µm,
- *Detector Height* = 300 µm,
- *Strip Pitch* = 400 µm,
- *Strip Width* = 390 µm,
- *Gain Scale* = 2.

To compare the measurements done with the 1060 nm wavelength (MIP-like) with a *Weightfield 2.0* simulation, the case *MIP with uniform charge deposition*

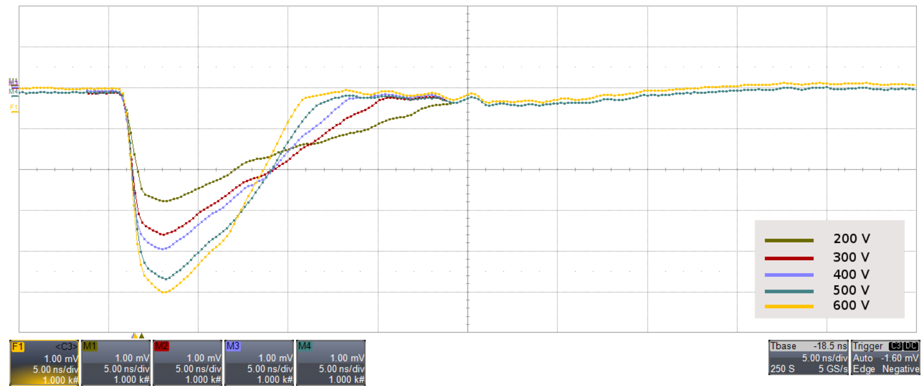

(a) MIP

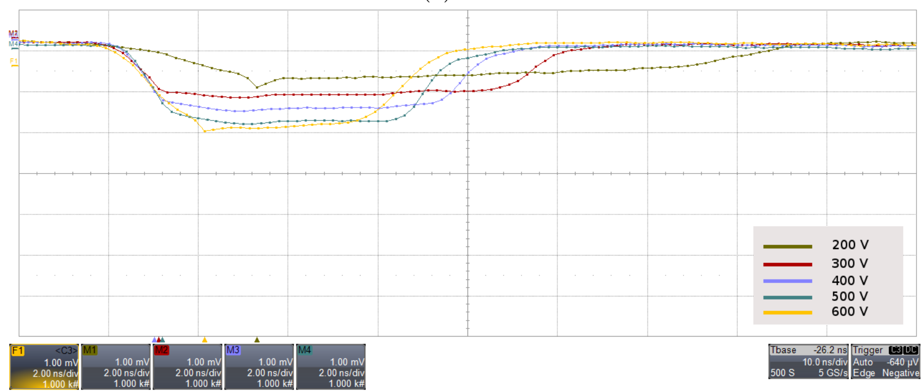

(b) alpha from top

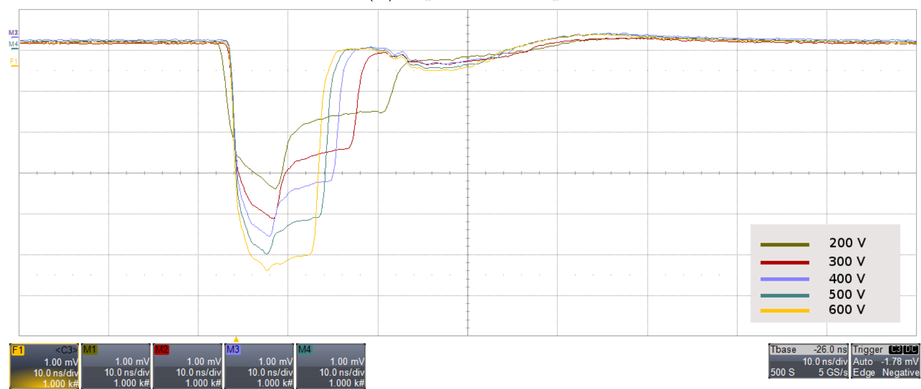

(c) alpha from bottom

Figure 6.11: Oscilloscope output as a function of bias voltage for a) MIP, b) alpha from top, c) alpha from bottom.

is used. Laser photons have low energy: each photon can only produce one e-h pair (Sec. 6.1) and no delta rays (which need higher energy). Moreover, the laser charge deposition can be considered uniform, being the exponential attenuation of Eq. 6.1 a non-noticeable effect.

When simulating alpha particles, the range parameter is set to 10 μm, because of

additional energy losses through air when traveling from the lens to the sensor, as discussed in Sec. 5.1.3.
In Fig. 6.11 the oscilloscope outputs are shown for the different cases (MIP, alpha from top and alpha from bottom) and at different bias voltages (from 200 to 500 V).

Comparison between measurements and simulation

To understand how a particular signal shape is formed, the case "alpha from the bottom" (Fig. 6.12) is analyzed in detail. At V_{bias} = 200 V, the initial bump

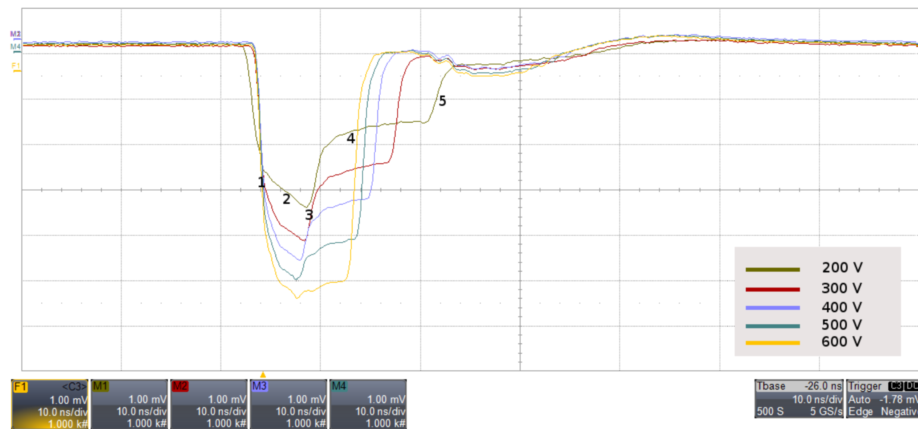

(a)

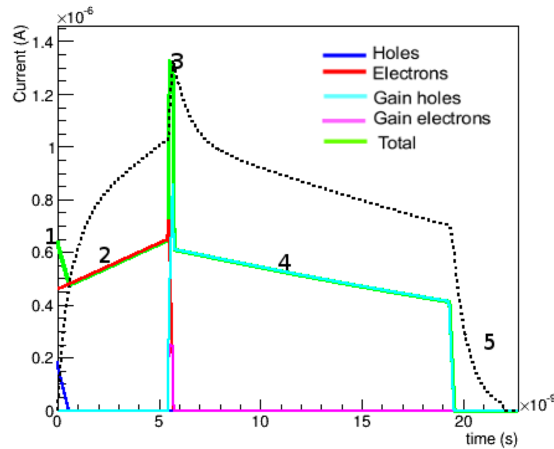

(b)

Figure 6.12: Oscilloscope output as a function of bias voltage for the case "alpha from the bottom" (a) compared to simulation with V_{bias} = 200 V (b).

in (1) is given by the "initial" holes being collected just after being produced. The rise (2) is due to electrons drifting toward the n^{++} electrode at the top of the sensor, where the electric field is higher: since at V_{bias} = 200 V their drift velocity has still not reached the saturation value, they accelerate as they move

in a higher field. The spike (3) is due to the "gain" electrons produced in the multiplication layer in the upper part of the sensor and immediately collected, while the slope (4) is given by "gain" holes which drift downwards to the backside of the sensor, decelerating because the electric field lowers, and are gradually collected (5).
As the bias voltage increase, the signal becomes shorter: the electric field strengthens, the charge carriers move with higher velocity and then the collection time gradually decreases. The gain electrons rise and the gain holes descent become less pronounced because the drift velocities are more and more close to saturation value. At $V_{bias} = 600$ V, the signal is flattened with respect to lower bias voltages, being drift velocities nearly constant, and the collection time noticeably reduced.

Results

The comparison between experimental data and simulation for the different kinds of particles and bias voltages is shown in Fig. 6.13, while the single components contributing to the total current are shown in Fig. 6.14. From the last figure, we can notice that part of the signal is given by charge multiplication: this is well visible from the longer "tails" in the MIP and alpha-from-bottom signals. Alpha-from-top signal instead, is dominated by the holes component: electrons are immediately collected, also those produced by charge multiplication are collected just after their production, while gain holes drift to the p electrode with the initial holes without substantially altering the collection time. Although the alpha-from-top signal does not contain substantial informations about the charge multiplication, it gives informations about the drift field and velocity: if the estimate for drift field (and then for drift velocity) were not correct or inaccurate, the signal length and the slope of the function electric field vs thickness would be different, leading to a disagreement between the predicted and measured drift velocity.
In the alpha-from-bottom signal, it is well distinguishable the electron component (in gray): at low bias voltages, one can see from the slope of the electron component that the drift velocity is not saturated, being the electric field too low. At higher voltages instead, drift velocity reaches the saturation value, because of the higher field, and then the electrons current shape is flattened.

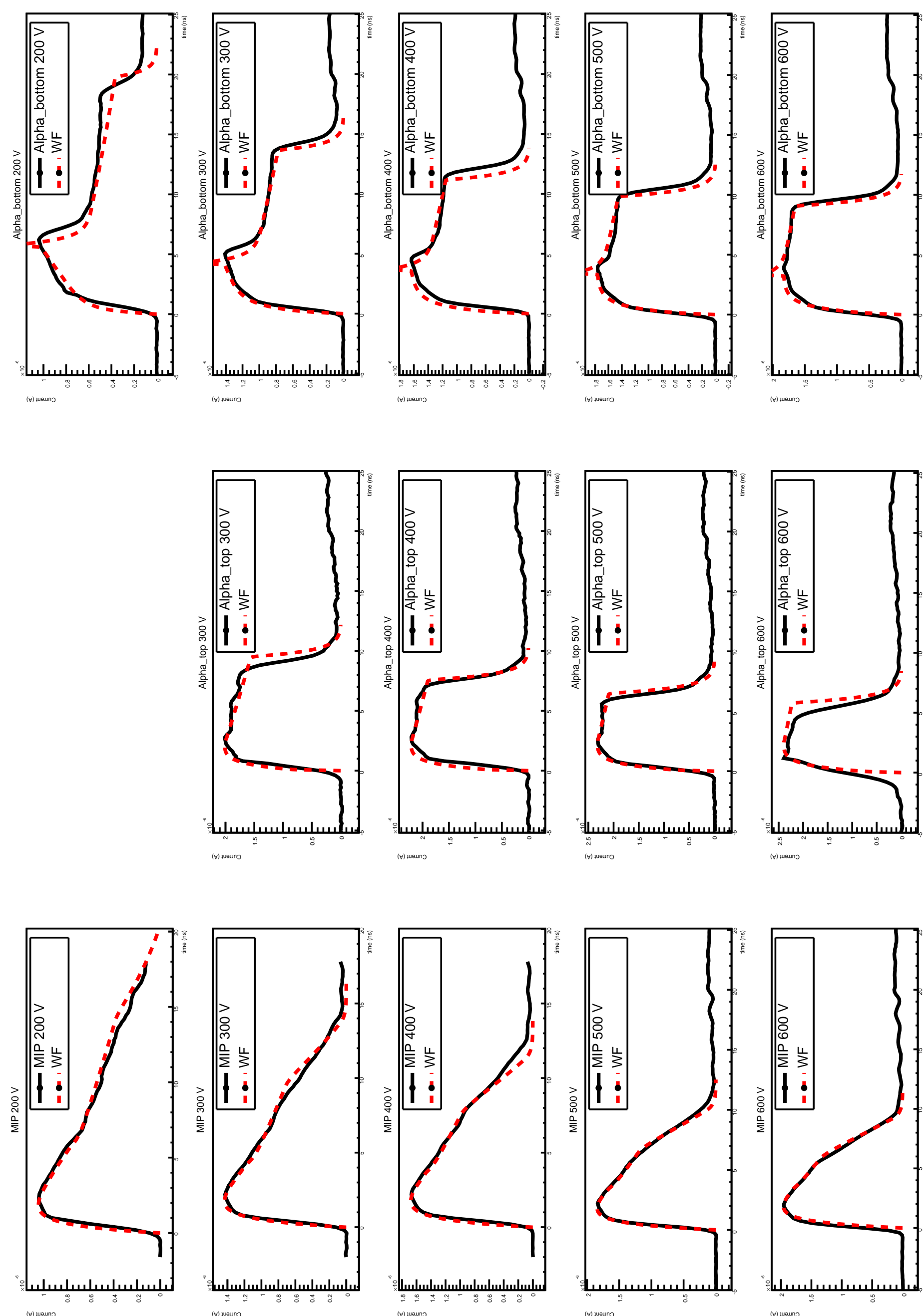

Figure 6.13: Comparison between experimental data (black solid line) and simulation (red dashed line) for different bias voltages and particle types.

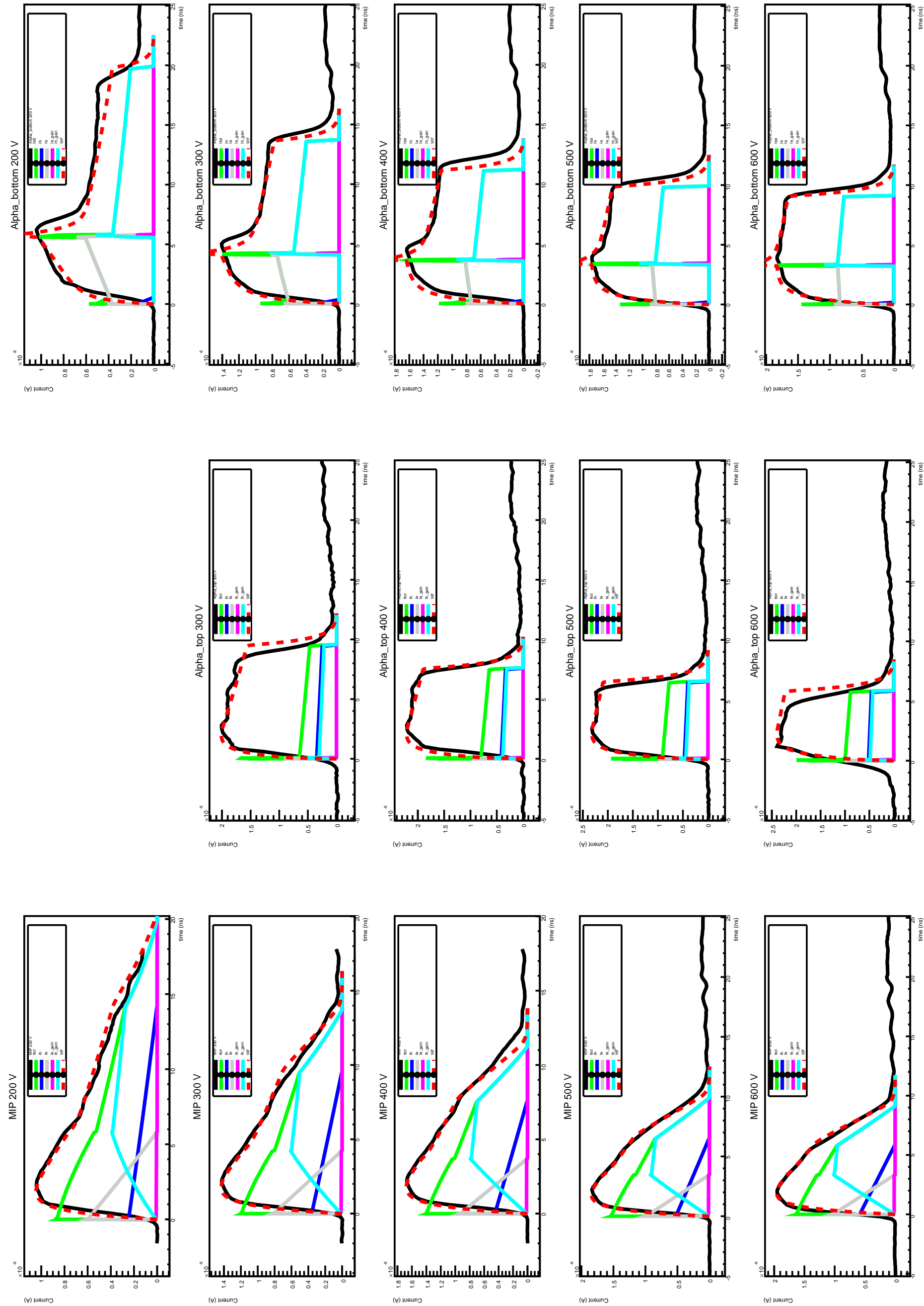

Figure 6.14: Different contributions to the total current superimposed to the previous graph.

Conclusions

In this thesis the principles at the base of signal formation in silicon sensors have been studied, to predict the signal shape in Ultra-Fast Silicon Detectors (UFSD), which are innovative detectors with a moderate internal gain ($\sim$3-10). For this purpose, charge multiplication in silicon, based on the impact ionization mechanism has been analyzed.
Charge multiplication allows to increase the signal amplitude, resulting in the possibility of a reduced sensor thickness, in order to get a very fast sensor, able to measure both space and time coordinates with good accuracy.
As the main project of this thesis, the code *Weightfield 2.0* has been developed, which simulates the production and the shape of the signal in UFSD, by implementing a gain layer which multiplies the charge carriers. This program can also produce both the current signals and the output voltages of an oscilloscope and a shaper, which can be directly compared with laboratory measurements.
In order to study the signal of UFSD prototypes, a laboratory setup has been built for testing these sensors with laser beams of different wavelengths, whose signals are similar to those of a minimum ionizing particle and an alpha particle. The comparison between data and simulation shows a good agreement.

Bibliography

[1] H. Bethe and W. Heitler, *On the stopping of fast particles and on the creation of positive electrons*, in Proc. Royal Soc. London, vol. A 146, pp. 83–112, 1934.

[2] K. Nakamura et al. (Particle Data Group), J. Phys. G 37, 075021 (2010) and 2011 partial update for the 2012 edition.

[3] F. Ravera, *Characterization and performance of 3D silicon pixel detectors for CMS*, Master's thesis, Università degli Studi di Torino, 2013.

[4] F. Rivero, *Characterization of FBK-irst 3D Double Side Double Type Column Silicon Sensors*, Master's thesis, Università degli Studi di Torino, 2009.

[5] C. Kittel, *Introduction to Solid State Physics*, 8th Edition, Wiley, 2004.

[6] F. Hartmann, "Silicon tracking detectors in high-energy physics", *Nucl. Instrum. Meth.*, vol. A 666, pp. 25-46, 2012.

[7] S. M. Sze and K. K. Ng, *Physics of Semiconductor Devices*, McGraw-Hill Company, 2002.

[8] A. Doolittle, "Chapter 2: Density of States and Fermi Energy Concepts", *Semiconductor Devices*, Georgia Institute of Technology, 2011.

[9] B. Van Zeghbroeck, *Principles of Semiconductor Devices*, Chapter 2, `http://ecee.colorado.edu/~bart/book/`, 2011.

[10] M. Krammer, *Silicon Detectors*, Presentation. Praktikum 2010/2011, Institute of High Energy Physics, Vienna, Austria.

[11] T. Bergauer, *Silicon detectors in high energy physics*, Presentation, Detector School 2011, Institute of High Energy Physics, Vienna, Austria.

[12] S. Mattiazzo, *I Rivelatori a Silicio*, `www.pd.infn.it/~carlin/riv/Slides/parte7.pdf`, 2012.

[13] R.K. Bock, A. Vasilescu, *The Particle Detector BriefBook*, Springer, 1998

[14] S. Ramo, *Currents Induced by Electron Motion*, Proceedings of the I.R.E., pp. 584-585, 1939.

[15] W. Shockley, *Currents to Conductors Induced by a Moving Point Charge*, Journal of Applied Physics 9, p. 635, 1938.

[16] H. Spieler, *Front-End Electronics and Signal Processing*, ICFA Instrumentation School/Workshop, University of Michoacan, Mexico, 2002.

[17] H. Spieler, *Front-End Electronics for Detectors*, Nuclear Science Symposium and Medical Imaging Conference, Honolulu, 2007.

[18] E. Monteil, *Front-End amplifiers in 65nm CMOS technology for the upgrade of the pixel detector of the CMS experiment*, Master's thesis, Università degli Studi di Torino, 2013.

[19] R. Jaeger, *Introduction to Microelectronic Fabrication*, Prentice Hall, 2002.

[20] M. Moll, *Tracking with Solid Stare Detectors*, Presentation, CERN Academic Training Programme, 2005.

[21] Chenming Hu, *Modern Semiconductor Devices for Integrated Circuits*, Prentice Hall, 2009.

[22] N. Weste, K. Eshraghian, *Principles of CMOS VLSI Design*, Addison-Wesley, 1988.

[23] J. M. Park, *Novel Power Devices for Smart Power Applications*, PhD Thesis, Technischen Universität Wien, Vienna, 2004.

[24] M. Keil, *Leakage current measurements in the ATLAS Pixel Detector*, Presentation, RD50 Workshop, Bari, June 2012.

[25] J. Schumacher, *Characterization Studies of Silicon Photomultipliers: Noise and Relative Photon Detection Efficiency*, Master's Thesis, Technischen Hochschule Aachen, 2011.

[26] B. Dolgoshein et al., *Status report on silicon photomultiplier development and its applications*, Article, Nucl. Instrum. Meth., vol. A 563, pp. 368–376, 2006.

[27] W. Maes, K. De Meyer, R. Van Overstraeten, "Impact ionization in silicon, a review and update", *Solid-State Electronics*, vol. 33, pp. 705–718, 1990.

[28] S. Meroli, *Two growth techniques for mono-crystalline silicon: Czochralski vs Float Zone*, `http://meroli.web.cern.ch/meroli/Lecture_silicon_floatzone_czochralski.html`, 2012.

[29] M. A. Karagounis, *Analog Integrated CMOS Circuits for the Readout and Powering of Highly Segmented Detectors in Particle Physics Applications*, PhD thesis, Fernuniversität Hagen, 2010.

[30] E. Alagoz et al., *Simulation and laboratory test results of 3D CMS pixel detectors for HL-LHC*, JINST 7, n. 08, p. P08023, 2012.

[31] H.F.W. Sadrozinski et al., *Ultra-fast silicon detectors*, Nucl. Instrum. Meth., vol. A 730, pp. 226–231, 2013.

[32] H.F.W. Sadrozinski et al., *4D Sensors: Unifying the Space and Time Domain with Ultra-Fast Silicon Detectors UFSD*, Presentation, SCIPP, Univ. of California Santa Cruz, 2013.

[33] A. Macchiolo, *Simulation of Irradiated Detectors and Charge Multiplication Effect in planar silicon sensors*, Vertex Workshop, Max-Planck-Institut für Physik, Munich, 2011.

[34] H. Bichsel, "Straggling in Thin Silicon Detectors", *Rev. Mod. Phys.* 60, 1988.

[35] M. Friedl, *The CMS Silicon Strip Tracker and its Electronic Readout*, Ph.D. Thesis, Vienna University of Technology, 2001.

[36] S. Parker, C. Kenney, J. Segal *3-D: A proposed new architecture for solid state radiation detectors*, Article, Nucl. Instrum. Meth., vol. A 395, pp. 328-343, 1997.

[37] B. Kolbinger, *Simulation of a Silicon-Strip Detector*, Report, HEPHY, Vienna, 2012.

[38] S. Meroli et al., *Energy loss measurement for charged particles in very thin silicon layers*, Article, JINST 6 P06013, 2011.

[39] V. Saveliev, "Photomultiplier - New Era of Photon Detection", *Advances in Optical and Photonic Devices*, Ki Young Kim (Ed.), ISBN: 978-953-7619-76-3, InTech, DOI: 10.5772/7150. Available from: `http://www.intechopen.com/books/advances-in-optical-and-photonic-devices/silicon-photomultiplier-new-era-of-photon-detection`

[40] H. Sadrozinski, A.Seiden, N. Cartiglia, *Ultra-Fast Silicon Detectors*, Presentation, 20th RD50 Workshop, Bari, 2012.

[41] N. Cartiglia et al., *Performance of Ultra-Fast Silicon Detectors*, Article, JINST 9 C02001, 2014.

[42] N. Cartiglia, *Timing capabilities of Ultra-Fast Silicon Detector*, Presentation, 9th "Trento" Workshop on Advanced Silicon Radiation Detectors, Genova, 2014.

[43] H. Spieler, *Semiconductor Detectors, Part 2*, SLUO Lectures on Detector Techniques, October 30, 1998.

[44] S. Garbolino, *Integrated Front-End Electronics for High Precision Timing Measurements with Radiation Detectors*, PhD Thesis, Università degli Studi di Torino, 2011.

[45] F. Cenna, *Simulation of Ultra-Fast Silicon Detectors*, Presentation, 9th "Trento" Workshop on Advanced Silicon Radiation Detectors, Genova, 2014.

[46] P. Fernández-Martínez, *Low Gain Avalanche Detectors (LGAD): Run 6474*, Private communication.

[47] G. Pellegrini, *Simulation of new P-type strip detectors*, Presentation, 17th RD50 Workshop, CERN, Geneva.

Acknowledgements

Vorrei ringraziare innanzi tutto Ada e Nicolò per il loro aiuto, sia per quanto riguarda il programma che per il testo e per la loro disponibilità.
Giulia, Antonella, Fabio ed Ennio per il loro supporto, Luca per avermi dato una mano con la parte di elettronica, Diego, Fede, Greg, Cisco e tutti gli altri fisici.
Grazie anche a tutti quelli che mi hanno incoraggiata al Trento Workshop (un ringraziamento speciale va a chi mi ha accompaganta sul treno!). Grazie anche a Veronica e tutti i non-fisici che mi hanno dato una mano in questo periodo.
Un grazie enorme a Fabio per avermi supportato (e sopportato) in tutto questo tempo e alla mia famiglia che ha sempre avuto fiducia in me.